Design and Synthesis of a Series of Redox Active Tetrazine and Triazine Based Transition Metal Complexes

by

Yixin Zhang

A thesis submitted in conformity with the requirements
for the degree of Master of Science in Chemistry

Department of Chemistry and Biomolecular Sciences
University of Ottawa

Design and Synthesis of a Series of Redox Active Tetrazine and Triazine Based Transition Metal Complexes

Yixin Zhang

Master of Science in Chemistry

Department of Chemistry and Biomolecular Sciences
University of Ottawa

2018

Abstract

The use of two different chelating redox active ligands, 2,6-bis(6-methyl-1,2,4,5-3-yl) pyridine (BTZP) and 2,6-bis-(5,6-dialkyl-1,2,4-triazin-3-yl)-pyridine (BTP) in heterometallic first row and second row transition metal chemistry has yielded two new families of redox active metal complexes. These complexes were found to exhibit interesting electrochemical and magnetic properties.

In this thesis, Chapter 1 lays the foundation for the research presented within. This section covers the fundamentals of the ligand design, ligand synthesis and related coordination chemistry literature review. Chapters 2 and 3 report the results of the current thesis. In Chapter 2, the synthesis and characterization of a family of discrete molecules and supramolecular arrangements, employing the ligand BTZP, is presented. All of the complexes presented in Chapter 2 are successfully synthesized and characterized with electrochemical and magnetic studies. According to the electrochemical data, it is found that the classic "terpy-like" complexes with $[Co(BTZP)_2]^{2+}$ formula fosters more stability in the redox process. In Chapter 3, a family of transition metal complexes with $[M(BTP)_2]^{2+}$ (M=Fe or Co) inorganic cores were obtained through the employment of the ligand BTP with various anions. In addition, dimeric molecules with $[CoX_4(BTP)_2]$ formula were also obtained by solvothermal synthesis. The complexes were also electrochemically characterized, with all the complexes capable of being reduced, while only $[Co^{II}(BTP)_2](ClO_4)_2$ showed reversible redox process. Similar with BTZP, the series of BTP based complexes are also characterized through magnetic measurement. Only cobalt-based BTP

complexes are paramagnetic, with $[Co^{II}(BTP)_2]^{2+}$ being spin crossover active when BF_4^- and ClO_4^- are present. However, the presence of NCS^- and halides lead to either antiferromagnetic interactions and ferromagnetic interactions dominating at different temperature regimes.

Acknowledgments

First and foremost, I would like to express my most sincere gratitude to my supervisor, Prof. Muralee Murugesu, for taking me on as a student and giving me this opportunity to further my skills as a synthetic chemist, offering me the chance to contribute to the molecular magnetism field. Thank you for pushing me to newer and greater heights. I have thoroughly enjoyed the numerous clever analogies you have shared with me over the past 2 years, with your patience, motivation and immense knowledge. I'm looking forward to keeping working with you!

I also would like to recognize the contributions of Dr. Bulat Gabidullin, our X-ray crystallographer. There are so many work depending on the X-ray results, and I am very grateful for having someone with your skills participate so actively in my research. I also would like to thank Ms. Rola Mansa for her assistance with TGA measurements.

Finally, I would like to thank all previous and current lab group members for their input on this work, including Dr. Amélie Pialat who taught me the basics of organic synthesis. Dr. Jamie Frost helped me a lot in the early stages of research, and thanks for his kindly teaching for the basic research principles. A special mention to Miss. Katie Harriman for helping me out measuring the samples in the SQUID magnetometry and teaching me a lot in the early stages of the research in terms of magnetism part as well as providing invaluable insight. Many thanks to Mr. Paul Richardson for his kindly help for explaining inorganic basic concepts and English correcting. I also would like to thank to Mr. Maykon Lemes, who has been a fantastic colleague and friend to work with throughout my graduate studies. I also would like to thank Mr Gabriel Brunet for his assistance with PXRD measurements, solving magnetic problems as well as grammar checking. Finally, I would like to recognize Mr. Thomas Lacelle, who gives me a numerous help during the past two years. It was a really unforgettable time for taking class with you. Thank you so much for helping me to pass all exams.

Last but not least, I would like to give thanks to all my friends who live in Ottawa, as well as living in all around the world now. Thank you so much about contributions that you given to me, and I really enjoy the moment with you. Special mention to my best friend back in China now Prof. Sha Feng, who has been an amazing organic synthetic chemist, and taught me a lot of tricks in the organic synthesis as well as numerous general chemistry contents. I also sincerely appreciate

Mr Bowen Wang for being a fantastic supporter in every single moment together. Thank you so much for teaching me how to be a researcher in the very early stage and how to solve problem by myself. With your support and help, I could be always positive and get over any challenges I have had during the study. Finally, I would like also to give my sincere gratitude to my parents, even though they cannot understand any single English word, but support me all the time and encourage me to try what I would like to do. I really thank them to give me this great opportunity to study chemistry in the University of Ottawa and accomplish my dream.

Table of Contents

Acknowledgments iv

Table of Contents vi

1 General introduction 1

1.1 Tetrazines and triazines 1

1.2 Ligand design 3

1.2.1 The choice of redox activity 3

1.2.2 Chelating ligand 4

1.3 Literature method for synthesis of BTZP and BTP 6

1.4 Previous literature review 8

1.4.1 Coordination chemistry of BTZP 8

1.4.2 Coordination chemistry of BTP 9

1.5 Project goal 11

2 Synthesis and characterizations in the molecular and supramolecular arrangements of transition metal complexes with a 2,6-bis(6-methyl-1,2,4,5-3-yl) pyridine ligand. 13

2.1 Introduction 14

2.2 Experimental 15

2.2.1 Materials and methods 15

2.2.2 Synthesis of 2,6-dicyanopyridine 15

2.2.3 Synthesis of the bis-tetrazine ligand (BTZP) 16

2.2.4 Synthesis of the $[Co^{II}(BTZP)_2](ClO_4)_2 \cdot 2MeCN$ (**1**) 17

2.2.5 Synthesis of the $[Ni^{II}(BTZP)(MeCN)_3](ClO_4)_2$ (**2**) 17

2.2.6 Synthesis of the $[Ni^{II}Cl_2(BTZP)(MeCN)] \cdot 2MeCN \cdot H_2O$ (**3a**) 17

2.2.7 Synthesis of the $[Ni^{II}Cl_2(BTZP)(MeCN)] \cdot MeCN$ (**3b**) 18

2.2.8 Synthesis of the $\{[Cd^{II}(NO_3)_2(BTZP)]\}_n$ (**4**) 18

2.2.9 Physical measurements 19

2.2.10 X-ray crystallography 19

2.2.11 Magnetic measurements....20

2.2.12 X-ray powder diffraction (XRPD) 20

2.3 Results and discussion 22

2.3.1 Synthesis of BTZP ligand 22

2.3.2 Synthesis and structure analysis for complex **1-4**....23

2.3.3 UV-vis spectroscopy 30

2.3.4 Electrochemical studies of complexes **1-4**....31

2.3.5 Magnetic studies 35

2.4 Conclusion and future work....38

3 Reversible redox, spin crossover, and superexchange coupling in 3-d transition metal complexes of bis-azinyl analogues of 2,2':6',2''-terpyridine....41

3.1 Introduction....42

3.2 Experimental section....44

3.2.1 General considerations....44

3.2.2 Synthesis of 2,6-dicyanopyridine....44

3.2.3 Synthesis of pyridine-2,6-bis(carboximidhydrazide)....44

3.2.4 Synthesis of 2,6-bis-(5,6-dialkyl-1,2,4-triazin-3-yl)-pyridine (BTP) 45

3.2.5 Synthesis of $[Fe^{II}(BTP)_2]$ $(BF_4)_2 \cdot 4MeCN \cdot Et_2O$ (**5a**). 45

3.2.6 Synthesis of $[Fe^{II}(BTP)_2]$ $(ClO_4)_2 \cdot 2MeOH$ (**5b**). 46

3.2.7 Synthesis of $[Co^{II}(BTP)_2]$ $(BF_4)_2 \cdot 3MeCN$ (**6a**). 46

3.2.8 Synthesis of $[Co^{II}(BTP)_2]$ $(ClO_4)_2 \cdot 4MeCN$ (**6b**). 46

3.2.9 Synthesis of $[Co^{II}(BTP)_2]$ $[Co^{II}(NCS)_4]$ (**6c**). 47

3.2.10 Synthesis of $[Co^{II}_2(BTP)_2Cl_4]$ (**7a**). 47

3.2.11 Synthesis of $[Co^{II}_2(BTP)_2Br_4] \cdot MeCN$ (**7b**).....47

3.2.12 Physical measurements.....48

3.2.13 Single crystal X-ray diffraction studies.....48

3.2.14 X-ray powder diffraction (XRPD).....49

3.3 Results and discussion.....51

3.3.1 Synthesis and structural analysis of BTP ligand.....51

3.3.2 Synthesis and structural analysis for complex **5-7**.....54

3.3.3 Thermogravimetric analysis.....62

3.3.4 Diffuse reflectance spectroscopy analysis.....64

3.3.5 Electrochemical studies of BTP and complexes **5-7**.....65

3.3.6 Magnetic properties.....68

3.3.7 Proposed super-exchange mechanism.....74

3.4 Conclusion and future work.....75

4 Conclusions and outlook.....77

References.....79

List of Schemes

Scheme 1.1. Reduction pathway of tetrazines. The first redox process is reversible and the second process is, most of the time, irreversible, because of the immediate protonation of two N anions...3

Scheme 1.2. Literature synthetic routes for the preparation of BTZP and BTP ligand. There is only one reported synthetic route for BTZP, while BTP can be obtained by the introducing [a] glyoxal trimer, [b] monomeric glyoxal, and [c] 2,3-dihydroxy-1,4-dioxane, with the reaction of pyridine-2,6-biscarbamidrazone... ……...…..……..7

Scheme 2.1. Synthesis of compounds **1**-**4**……..24

Scheme 3.1. Synthetic route for BTP ligand…….52

Scheme 3.2. Synthesis of complexes **5**-**7**. M = Fe^{II} or Co^{II} and X = Cl^- or Br^-……55

List of Figures

Figure 1.1. Three structural isomers of tetrazines……2

Figure 1.2. Three structural isomers of triazines…… 2

Figure 1.3. The classic terpy-like coordination mode with first row transition metals. Reported by Elgrishi and coworkers……4

Figure 1.4. The ligand design modification of terpy by introduction of nitrogen rich tetrazine rings at the 2 and 6 positions of the central pyridine ring, named 2,6-bis(6-methyl-1,2,4,5-3-yl) pyridine (BTZP)……...5

Figure 1.5. The ligand design modification of terpy by introduction of nitrogen rich triazine rings at the 2 and 6 positions of the central pyridine ring, named 2,6-bis-(5,6-dialkyl-1,2,4-triazin-3-yl)-pyridine (BTP). ……...6

Figure 1.6. The (BTZP)CuCl polymer chain, showing the repeating unit. Shaded unlabeled atoms are nitrogen. Note the orientation of the tetrazine nitrogen lone pairs away from copper.……9

Figure 1.7. Structure of $[Ln(NO_3)_3(BTP)_2]$ (Ln=Pr^{III} and Nd^{III}), reported by Boucher and coworkers. H atoms are omitted for clarity. Color code: yellow (Ln), blue (N), red (O) and black (C). Reproduced from Boucher and co-workers……..……10

Figure 1.8. Structure of $[Eu_2(BTP)_2(NO_3)_6] \cdot 2MeCN$, reported by Bhattacharyya and coworkers. H atoms are omitted for clarity. Color code: yellow (Eu), blue (N), red (O) and black (C). Reproduced from Bhattacharyya and coworkers……11

Figure 2.1. X-ray powder diffraction of $[Co^{II}(BTZP)_2](ClO_4)_2 \cdot 2MeCN$, **1**, (red) in the 5-50° 2θ region, as compared with the theoretical pattern generated from single crystal X-ray data (black)……....21

Figure 2.2. X-ray powder diffraction of $[Ni^{II}Cl_2(BTZP)(MeCN)] \cdot MeCN$, **3b**, (red) in the 5-50° 2θ region, as compared with the theoretical pattern generated from single crystal X-ray data (black)……....21

Figure 2.3. X-ray powder diffraction of $[\{[Cd^{II}(NO_3)_2(BTZP)]\}_n$, **4**, (red) in the 5-50° 2θ region, as compared with the theoretical pattern generated from single crystal X-ray data (black)……. 22

Figure 2.4. Partially labelled molecular structures of complexes $[Co^{II}(BTZP)_2]^{2+}$, **1**. Colour code: pink (Co), blue (N), and black (C). All of hydrogen atoms and solvent molecules are omitted for clarity...……..……....25

Figure 2.5. Partially labelled molecular structures of complexes $[Ni^{II}(BTZP)(MeCN)_3]^{2+}$, **2**. Color code: green (Ni), blue (N), and black (C). All of hydrogen atoms are omitted for clarity…….26
Figure 2.6. Representative example of complex $[Ni^{II}Cl_2(BTZP)(MeCN)]$, **3**. Colour code: olive green (Ni), light green (Cl), blue (N), and black (C). All of hydrogen atoms and solvent molecules are omitted for clarity. ……..……..28
Figure 2.7. Partially labelled molecular structures of complexes $\{[Cd^{II}(NO_3)_2\ (BTZP)]\}_n$, **4**. Colour code: dark pink (Cd), blue (N), red (O) and black (C). All of hydrogen atoms are omitted for clarity... ……..…..29
Figure 2.8. Self-assembling helical twist in the space fill supramolecular arrangement of the complex **4**. Colour code: dark pink (Cd), blue (N), red (O) and black (C). All of hydrogen atoms are omitted for clarity. ……..…..30
Figure 2.9. Normalized Kubelka-Munk spectra for BTZP and complexes **1-4**…….31
Figure 2.10. CV scan of $[Co^{II}\ (BTZP)_2](ClO_4)_2 \cdot 2MeCN$ (**1**) (blue line on the left) in MeCN solution (0.1 M $[Bu_4N][PF_6]$, 0.1 V/s) and multiple scans sweep rate from 0.05 V/s to 3.2 V/s (blue to green lines on the right). Black arrow indicates the direction of sweep……...33
Figure 2.11. CV scan of $[Ni^{II}\ (BTZP)(MeCN)_3](ClO_4)_2$ (**2**) red line on the left) in MeCN solution (0.1 M $[Bu_4N][PF_6]$, 0.1 V/s) and multiple scans sweep rate from 0.05 V/s to 3.2 V/s (black to red lines on the right). Black arrow indicates the direction of sweep……34
Figure 2.12. CV scan of $[Ni^{II}\ Cl_2(BTZP)(MeCN)]$ (**3**) (orange line on the left) in MeCN solution (0.1 M $[Bu_4N][PF_6]$, 0.1 V/s) and multiple scans sweep rate from 0.05 V/s to 3.2 V/s (black to orange on the right). Black arrow indicates the direction of sweep…….34
Figure 2.13. CV scan of $\{[Cd^{II}(NO_3)_2\ (BTZP)]\}_n$ (**4**) (pink line on the left) in MeCN solution (0.1 M $[Bu_4N][PF_6]$, 0.1 V/s) and multiple scans sweep rate from 0.05 V/s to 3.2 V/s (pink to black lines on the right). Black arrow indicates the direction of sweep……...35
Figure 2.14. Temperature dependence of the χT product at 1000 Oe for **1**, **2** and **3**, with χ being the molar magnetic susceptibility per molecule as defined by *M/H*. Experimental data is represented by hollow circles…….36
Figure 2.15. Field dependence of the magnetization (left) and the reduced magnetization (right) at 1.8, 3, 5 and 7 K for **1**. Experimental data is represented by solid circles…….……37
Figure 2.16. Field dependence of the magnetization (left) and the reduced magnetization (right) at 1.8, 3, 5 and 7 K for **2**. Experimental data is represented by solid circles…….38

Figure 2.17. Field dependence of the magnetization (left) and the reduced magnetization (right) at 1.8, 3, 5 and 7 K for **3**. Experimental data is represented by solid circles…….38
Figure 3.1. The ligand 2,6-bis-(5,6-dialkyl-1,2,4-triazin-3-yl)-pyridine (BTP) and potential coordination mode of BTP ligand, demonstrating the encapsulation of one metal center. In all complexes, the central pyridine ring and bis-triazine rings are coordinated to metal ions……43
Figure 3.2 X-ray powder diffraction of $[Co^{II}_2(^2\text{-}Cl)_2(BTP)_2Cl_2]$, **7a** (red) in the 5-50° 2θ region, as compared with the theoretical pattern generated from single crystal X-ray data (black).…….50
Figure 3.3 X-ray powder diffraction of $[Co^{II}_2(^2\text{-}Cl)_2(BTP)_2Br_2]$, **7b** (red) in the 5-50° 2θ region, as compared with the theoretical pattern generated from single crystal X-ray data (black)…..…..51
Figure 3.4. [a] Molecular structure of 2,6-bis-(5,6-dialkyl-1,2,4-triazin-3-yl)-pyridines (BTP). Colour code: blue (N) and black (C). All of hydrogen atoms are invisible for clarity. **[b]** Two BTP molecules within the same plane to form a dimeric-like structure which exhibits centro-symmetry. Colour code: blue (N), black (C) and grey (H). Red dash represents C-H···N hydrogen bonds and blue dash represents for the short contacts between C···N……..53
Figure 3.5. Partially labelled molecular structures of complexes $[Fe^{II}(BTP)_2]^{2+}$, **5a**. Colour code: olive green (Fe), blue (N), and black (C). All of hydrogen atoms and solvent molecules are omitted for clarity……56
Figure 3.6. Partially labelled molecular structures of complexes $[Co^{II}(BTP)_2]^{2+}$, **6a** (left) and **6b** (right). Colour code: pink (Co), blue (N), and black (C). All hydrogen atoms and solvent molecules are omitted for clarity…….57
Figure 3.7. Partially labelled molecular structures of complexes $[Co^{II}(BTP)_2][Co^{II}(NCS)_4]$, **6c**. Color code: pink (Co), yellow(S), blue (N), and grey (C). All of hydrogen atoms are omitted for clarity…….59
Figure 3.8. Ball and stick, and spacefill molecular structures constructed through *zig-zag* anion-π-system interactions in the structure of **5a**, **5b**, **6a**, **6b** and **6c**. Hydrogen atoms and disorders were omitted for clarity. Colour code: olive green (Fe), red (O), bright green (F), green (Cl), gold (B), pink (Co), yellow (S), blue (N) and black (C)……..……...60
Figure 3.9. Partially labelled molecular structures of complexes $[Co^{II}_2(\mu^2\text{-}Cl)_2(BTP)_2Cl_2]$ **7a**, which exhibits centro-symmetry. Colour code: pink (Co), blue (N), green (Cl) and black (C). All of hydrogen atoms are invisible for clarity……...……..61

Figure 3.10. Partially labelled molecular structure of complexes [$Co^{II}(\mu$-$Br)_2(BTP)_2Br_2$], **7b**. Colour code: pink (Co), brown (Br), blue (N), and black (C). All hydrogen atoms and solvent molecules are omitted for clarity……62
Figure 3.11. TGA analysis of **6a** performed in a dynamic nitrogen atmosphere……63
Figure 3.12. TGA analysis of **6b** performed in a dynamic nitrogen atmosphere……63
Figure 3.13. Normalized Kubelka-Munk spectra for BTP and complexes **5-7**……..65
Figure 3.14. CV scan of BTP ([**a**]; top orange line) and **6b** ([**b**]; bottom pink line) in MeCN solution (0.1 M [Bu_4N][PF_6], 100 mV/s). Black arrow indicates the direction of sweep……67
Figure 3.15. Temperature dependence of the χT product at 1000 Oe for **6a** (left), and **6b** (right), with χ being the molar magnetic susceptibility per molecule as defined by *M/H*……..69
Figure 3.16. Field dependence of the magnetization (left) and reduced magnetization (right) at 1.8, 3, 5 and 7 K for **6a**……70
Figure 3.17. Field dependence of the magnetization (left) and the reduced magnetization (right) at 1.8, 3, 5 and 7 K for **6b**……...70
Figure 3.18. Field dependence of the magnetization (left) and the reduced magnetization (right) at 1.8, 3, 5 and 7 K for **6c**. Experimental data is represented by hollow circles and best fits to the data as obtained through *PHI* software are depicted as solid lines……71
Figure 3.19. Temperature dependence of the χT product at 1000 Oe for **6c**, **7a** and **7b**, with χ being the molar magnetic susceptibility per molecule as defined by *M/H*. Experimental data is represented by hollow circles and best fits to the data depicted as solid lines……72
Figure 3.20. Field dependence of the magnetization (left) and the reduced magnetization (right) at 1.8, 3, 5 and 7 K for **7a**. Experimental data is represented by hollow circles and best fits to the data as obtained through *PHI* software are depicted as solid lines……74
Figure 3.21. Field dependence of the magnetization (left) and the reduced magnetization (right) at 1.8, 3, 5 and 7 K for **7b**. Experimental data is represented by hollow circles and best fits to the data as obtained through *PHI* software are depicted as solid lines……..74
Figure 3.22. Compilation of the magnetic behavior of several Co^{II} dimer with chloride bridge. Highlighted region indicates Co-X-Co (X =F, Cl, Br and I) bond angles that lead to ferromagnetic exchange interactions……74

List of Tables

Table 2.1. Summary of the crystal structure data and refinement for compounds **1-4**……19

Table 2.2. Selected bond distances (Å) for complex **1**……..25

Table 2.3. Selected bond distances (Å) for complex **2**. ……..26

Table 2.4. Selected bond distances (Å) for complex **3**. ……..28

Table 2.5. Selected bond distances (Å) for complex **4**. ……30

Table 2.6. CV data for the complexes in this work (MeCN/0.1 M Bu_4NBF_6, 298 K). Potentials are quoted at a scan rate 0.1 V/s *vs.* an internal Fc/Fc^+ standard…….32

Table 3.1. Summary of the crystal structure data and refinement for compounds **5-7** and BTP…49

Table 3.2. Selected bond distances (Å) for complexes **5a** and **5b**……..…56

Table 3.3. Selected bond distances (Å) for complexes **6a** and **6b**……..58

Table 3.4. Selected bond distances (Å) for complex **6c**…….60

Table 3.5. Selected bond distances (Å) for complex **7a** and **7b**…….62

Table 3.6. CV data for the complexes in this work (MeCN/0.1 M Bu_4NBF_6, 298 K). Potentials are quoted at a scan rate 0.1 V/s *vs.* an internal Fc/Fc^+ standard…….66

Table 3.7. Selected magnetic parameters for complex **6c**, **7a** and **7b**……....74

List of Abbreviations

1D	1-diementional
ac	Alternating current
BTP	2,6-bis-(5,6-dialkyl-1,2,4-triazin-3-yl)-pyridine
BTZP	2,6-bis(6-methyl-1,2,4,5-3-yl) pyridine
CCDC	Cambridge Crystallographic Data Center
dc	Direct current
DFT	Density Functional Theory
DMF	Dimethylformamide
DRS	Diffuse Reflectance Spectroscopy
EXAFS	Extended X-ray Absorption Fine Structure
FTIR	Fourier Transform Infrared Spectroscopy
HOMO	Highest Occupied Molecular Orbital
LUMO	Lowest Unoccupied Molecular Orbital
MeOH	Methanol
MeCN	Acetonitrile
MOF	Metal-Organic Framework
MRI	Magnetic Resonance Imaging
NMR	Nuclear Magnetic Resonance
PXRD	Powder X-ray Diffraction
SCXRD	Single-crystal X-ray Diffraction
SMM	Single Molecule Magnet
SQUID	Super-conducting Quantum Interference Device
TGA	Thermogravimetric Analysis
rf	Reflux
rt	Room temperature
UV	Ultraviolet
Å	Angstrom
cm	Centimeter
H	Magnetic field
Hz	Hertz
K	Kelvin
kcal	Kilocalorie
M	Molar concentration and Magnetization
min	Minute
mL	Millilitre
mM	Millimolar
mmol	Millimole
nm	Nanometer
Oe	Oersted
T	Temperature
V	Volume
χ	Molar magnetic susceptibility
χ'	In-phase magnetic susceptibility

χ''	Out-of-phase magnetic susceptibility
br	Broad
s	Strong (IR), singlet (NMR)
m	Medium (IR)
w	Weak
d	Doublet
t	Triplet

1 General introduction

1.1 Tetrazines and triazines

A heterocyclic compound is a cyclic molecule that has at least two different atoms as members of a ring.[1] It has various applications in organic chemistry,[2] inorganic chemistry,[3] analytical chemistry,[4] biology[5] and medicine.[6] The main reason is that heterocyclic compounds consist of a large group of organic molecules which exhibits biological activity resulting in a wide range of functionalities in nature.[7] Examples of heterocyclic compounds include many natural and synthetic dyes,[8-10] most biomass (cellulose and related materials),[11] a large majority of drugs[12-15] and some of the nucleic acids.[16, 17] Both tetrazine and triazine structures are heterocyclic rings, analogous to the six- membered benzene ring but with four or three carbon atoms replaced by nitrogen atoms.

Tetrazines were first discovered by Adolf Pinner in 1893 when he investigated the reactions between hydrazine and various nitriles.[18] To be specific, there are three known core-ring isomers of tetrazines that exist: namely 1,2,3,4-tetrazines, 1,2,3,5-tetrazines and 1,2,4,5-tetrazines (Figure 1.1). 1,2,3,4-tetrazines have all four nitrogen atoms bonded to each other on one side of the ring and 1,2,3,5-tetrazines have a single nitrogen bonded on the onside of the ring while the rest of nitrogen atoms are bonded on the other side of the ring. However, 1,2,4,5-tetrazine is the most symmetric isomer of the three, as it has two pairs of nitrogen atoms on the opposites sides of the ring. To date, the most common class of tetrazines are 1,2,4,5-tetrazines,[18, 19] as it has a highly electron-deficient π system of the tetrazine ring. Each tetrazine ring has four nitrogen atoms which lower the π^* orbitals, resulting in the tetrazines to be strong π-acceptors.[20] These unique properties of tetrazines offer great opportunity to have a wide variety of applications. Such applications include, but are not limited to, inverse-electron-demand Diels–Alder cycloadditions,[21] fluorescence,[22] energetic materials,[23-25] as well as radiochemical synthesis.[26]

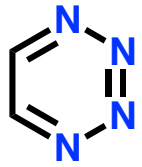

1,2,3,4-tetrazine

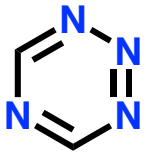

1,2,3,5-tetrazine

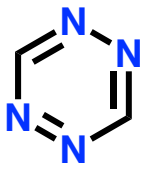

1,2,4,5-tetrazine

Figure 1.1. Three structural isomers of tetrazines.

On the other hand, like tetrazines, the three isomers of triazine are also distinguished from each other by the position of their nitrogen atoms, referred to 1,2,3-triazine, 1,2,4-triazine and 1,3,5-triazine (see Figure 1.2). To date, out of the above three triazine analogues, 1,2,3-triazine is the least explored one, as its N-N=N bonds are unstable. However, since 1,2,3-triazine has potent efficacy on biological metabolism with minimal side effects, its derivatives are more widely used in various pharmacological fields.[27-29] Since it has a similar structure to 1,2,3-triazine, 1,2,4-triazine derivatives have also found numerous biological activities, e.g. anticancer,[30] neuroleptic,[31] antiviral,[32, 33] anti-HIV,[34] therapeutic agents,[35] antifungal,[36-38] estrogen receptor modulators,[39, 40] antimalarial etc.[41] Apart from the pharmacological activities, the only structural difference between these two triazines is that 1,2,4-triazine has one nitrogen on the other side of the ring, increasing the stability of this ligand compared to 1,2,3-triazine. This ligand also provides us opportunities for studying spin delocalization,[42] intermolecular spin exchange interactions and electrochemical properties.[43] The last isomer, 1,3,5-triazine, sometimes can be called as *s*-triazine or symmetric triazine.[44] In the past two centuries, it and its derivatives have been intensively investigated due to their wide spread applications in optical bleaches,[45] plastic and rubber,[46, 47] dyes,[48] catalysis,[49] explosives[50] and pharmaceutical areas.[51]

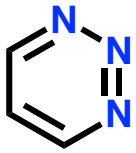

1,2,3-triazine

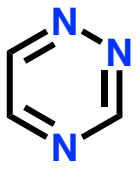

1,2,4-triazine

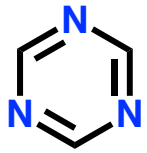

1,3,5-triazine

Figure 1.2. Three structural isomers of triazines.

1.2 Ligand design

1.2.1 The choice of redox activity

As mentioned above, the design and development of tetrazines and triazines has received a great deal of interest due to their numerous applications. In that regard, both tetrazines and triazines appear to be promising candidates for studying redox processes,[52] as their electron-deficient π systems have the potential to be reduced, affording an unpaired electron and therefore better opportunities for enhanced magnetic and electronic interactions between metal centres when used as a bridging ligand.[53] In order to promote strong exchange couplings between radicals and metal ions, ligand design would have to incorporate a moiety that it can readily undergo at least a single electron redox process, forming a radical species. Both tetrazines and triazines appear to be promising candidates, for their highly electron-deficient π system. The four or three nitrogen atoms lead to a low-lying π* LUMO (lowest unoccupied molecular orbital) which allows tetrazines and triazines to act as strong π-acceptors. These low-lying π* orbitals result in the facile one-electron reduction of tetrazines and triazines during the formation of radical anions. Additionally, the structural control through N-N bond stretching can aid in the stability of the radical state.[54] Tetrazines can exhibit both one-electron redox process or two-electron redox process (Scheme 1.1). However, in most cases, it shows a reversible one-electron reduction and, sometimes, a second irreversible reduction process.[55] In the case of the second irreversible reduction process, it is probably attributed to the immediate protonation of the doubly reduced tetrazine species to form 1,4-dihydrotetrazines.[55] Conversely, in the triazine case, the cyclic voltammetry data for triazines only exhibits a single reversible or irreversible redox process, due to the highly lability of doubly reduced triazine species.[56]

Scheme 1.1. Reduction pathway of tetrazines. The first redox process is reversible and the second process is, most of the time, irreversible, because of the immediate protonation of two N anions.[57]

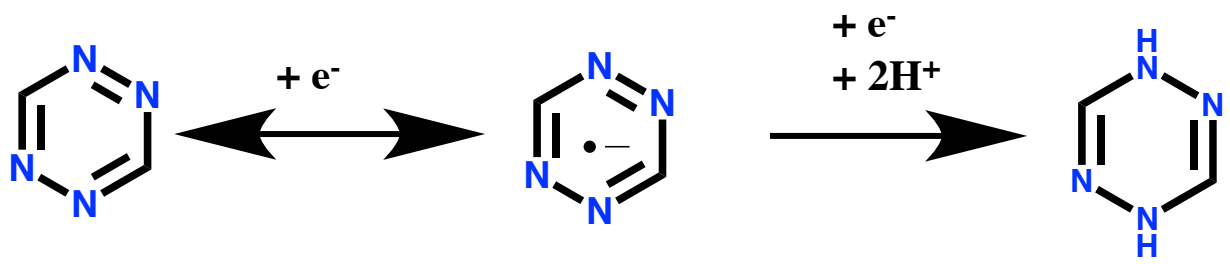

1.2.2 Chelating ligand

In coordination chemistry, chelation is a type of bonding motif between ligands and metal ions, involving the formation of two or more separate coordination bonds from the same ligand to the same central atom.[58-60] Compared to monodentate ligands, chelating ligands plays a significant role in the enhanced affinity for the metal ion. Chelation is useful in coordination chemistry, as their applications have been further studied in fertilizers,[61] manufacturing the homogeneous catalysts,[62-65] providing nutritional supplements,[66] as well as removing toxic metals from the body and contrast agents in MRI scanning.[67] Consequently, chelating ligand design and its resulting effect on coordination chemistry has received a great deal of interest. For example, one of the most widely studied chelating ligand systems is 2,2';6',2''-terpyridine (terpy) and its related derivatives, for it can provide coordination pocket and its coordinated metal ions always have a variety of geometries (Figure 1.3). [53, 68-70] These system have also been reported with various applications, such as spin-crossover,[71-74] sensors,[75] fluorescence,[76-78] light-emitting electrochemical cells,[79] and gas absorption.[80]

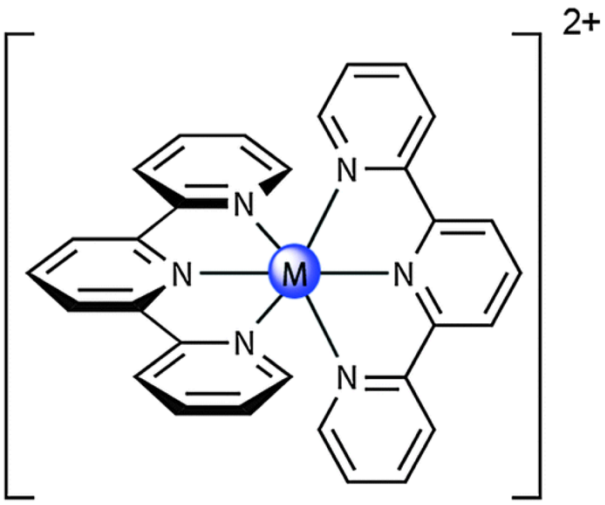

Figure 1.3. The classic terpy-like coordination mode with first row transition metals. Reported by Elgrishi and coworkers.[81]

However, the only observed electrochemical feature of terpy itself is an irreversible oxidation wave at 1.7 V (*vs*. Fc/Fc^{+}).[82] In that regard, research groups around the word have focused on developing terpy analogues as the demand for redox properties. The most common

way is to replace the peripheral positions on the pyridine ring with nitrogen rich function groups, as both the anionic and neutral states are potentially more stable. [53, 69, 83] Therefore, this may lead to ambiguity in the oxidation states of compounds containing these ligands. However, their applications have been held back by a few limitations, like the stability of the isolated metal complexes, solubility and reduction potentials.[84-88] Consequently, in the following projects, we decided to attach radical pendant groups in 2 and 6 positions, which is one of modifications of terpy which have been considered to obtain these desired properties, incorporating of nitrogen rich tetrazines and triazines of the central pyridine ring. The additional inclusion of heteroatoms (N) within the flanking heterocycles increases the π-accepting abilities of terpy, resulting in a stronger field ligand. This type of synthetic tunability is an attractive feature for controlling the spin-state of a chelated metal ion; a promising approach for the development of new molecular magnetic materials. Not only does this ligand design maintain the topology of terpy, but also increase the ligand field and redox acitivities. In this thesis, the ligands which have been chosen are in 2,6-bis(6-methyl-1,2,4,5-3-yl) pyridine (BTZP) and 2,6-bis-(5,6-dialkyl-1,2,4-triazin-3-yl)-pyridine (BTP) (Figure 1.4 and 1.5). Research into both ligand systems is relatively underdeveloped, compared to the numerous applications of terpy ligands in coordination chemistry field.[68-70, 89] This gives us enormous space to investigate and understand those two ligand systems.

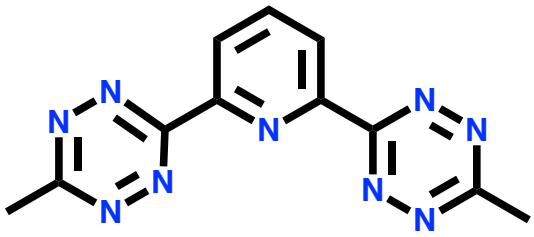

BTZP

Figure 1.4. The ligand design modification of terpy by introduction of nitrogen rich tetrazine rings at the 2 and 6 positions of the central pyridine ring, named 2,6-bis(6-methyl-1,2,4,5-3-yl) pyridine (BTZP).

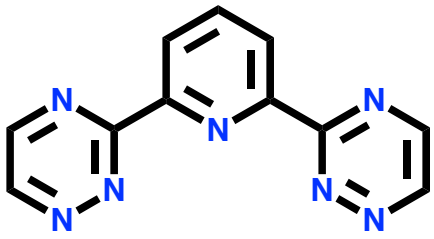

BTP

Figure 1.5. The ligand design modification of terpy by introduction of nitrogen rich triazine rings at the 2 and 6 positions of the central pyridine ring, named 2,6-bis-(5,6-dialkyl-1,2,4-triazin-3-yl)-pyridine (BTP).

1.3 Literature method for synthesis of BTZP and BTP

Because of the widespread interest in heterocycles, the synthesis of these compounds has always been among important research areas in synthetic chemistry. BTZP was recently reported by Caulton et.al in 2014 [84] (Scheme 1.2). The synthetic method of BTZP involves the addition of hydrazine to 2,6-pyridinedicarbonitrile, coupling with acetonitrile in the presence of sulfur. After this step, the published synthesis of BTZP involves the addition of CH_3COOH and $NaNO_2$ to generate NO_2 gas to act as an oxidant, closing the ring by a [4+2] cycloaddition reaction.[84] Residual polymerized side products were removed by column chromatography. The other side product, dimethyl tetrazine, is highly volatile, so it can be sublimed during the evaporation of solvent *in vacuo*. However, the reported yield is only 28%. [84]

Scheme 1.2. Literature synthetic routes for the preparation of BTZP and BTP ligand. There is only one reported synthetic route for BTZP,[84] while BTP can be obtained by the introducing [a] glyoxal trimer,[90, 91] [b] monomeric glyoxal,[92] and [c] 2,3-dihydroxy-1,4-dioxane,[93] with the reaction of pyridine-2,6-biscarbamidrazone.

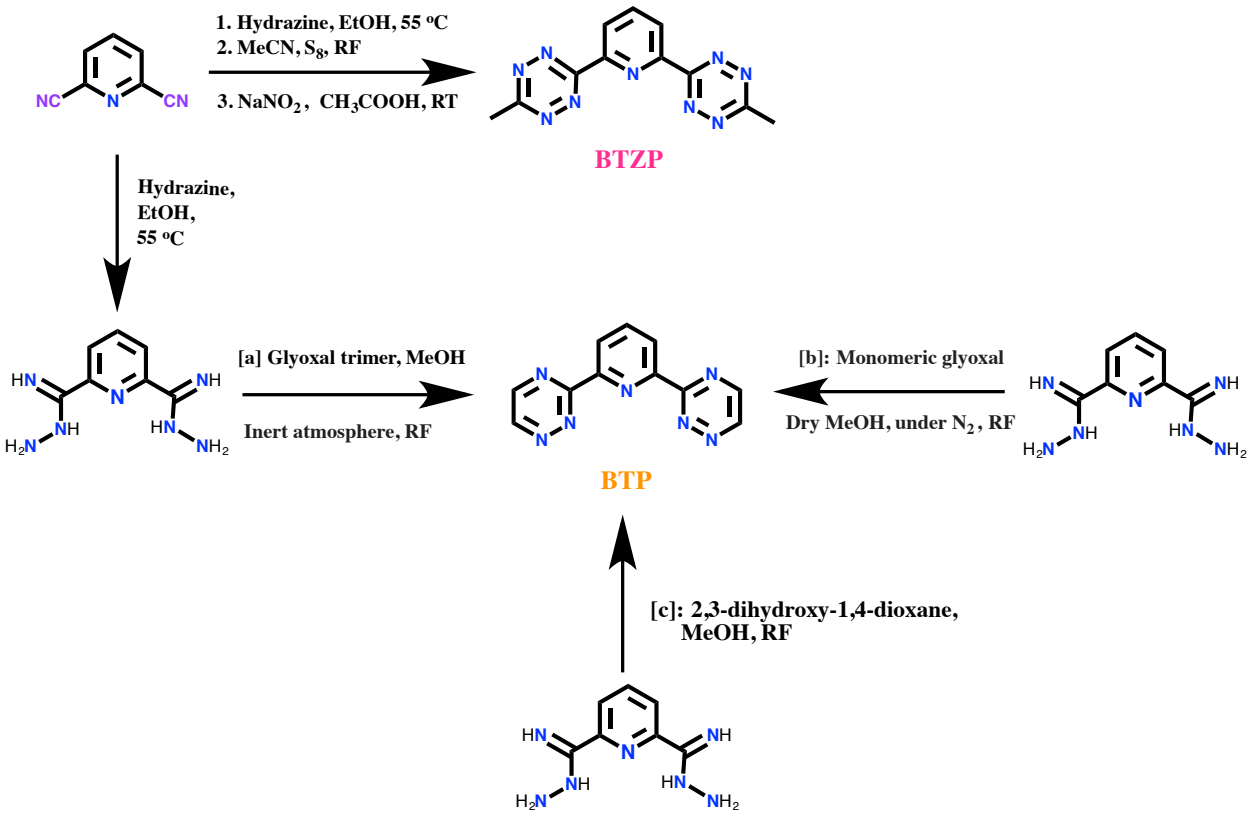

Unlike BTZP, BTP has a relatively longer history, and was first described by Sauer and co-workers in 1999. [92] There are three synthetic routes reported in the literature and all of them have the same precursor -- pyridine-2,6-biscarbamidrazone (Scheme 1.2). Additionally, it is interesting that 2,6-pyridinedicarbonitrile can also be used in the synthesis of BTP, as it is a common precursor for pyridine-2,6-biscarbamidrazone. The most popular synthetic route with the highest yield (75%[90] and ca. 80%[91]) involves the addition of glyoxal trimer in the dry methanol with the presence of pyridine-2,6-biscarbamidrazone. The reaction mixture was stirred at room temperature for 3 h under nitrogen to obtain the monomeric glyoxal and the reaction was followed by overnight refluxing. However, trimeric glyoxal is not commercially available and there are other researchers investigating whether they can use monomeric glyoxal to directly synthesize the BTP ligand. For example, Sauer and co-workers reported a BTP synthetic route by dissolving

monomeric glyoxal in dry methanol and rapidly adding in a stirred suspension of pyridine-2,6-biscarbamidrazone in MeOH.[92] The color of the stirred suspension turned yellow within 3 h at room temperature, and the reaction mixture was then heated to reflux for a further 2 h, with a yield of 67%. However, the anhydrous monomeric glyoxal is not commercially available and it has to be trapped at -78°C, which makes this synthesis quite challenging. Consequently, Ishizuka et. al reported a modified synthetic route, where instead of using glyoxal or its trimetric version, they introduced 2,3-dihydroxy-1,4-dioxane as a starting material. 2,3-dihydroxy-1,4-dioxane is relatively air stable and is commercially available, so the reaction conditions can be changed from inert to atmospheric. [93]

1.4 Previous literature review

1.4.1 Coordination chemistry of BTZP

As mentioned before, BTZP is still understudied, and all previous crystal structures were reported by Caulton and coworkers. [57, 84, 94, 95] It was first investigated with the goal of electron storage capacity in 2014.[84] However, only one solid-state structure of an iron (II) complex with a characteristic "terpy-like" structure, with the formula of $[Fe(BTZP)_2]^{2+}$ was investigated in this paper, through the use of $Fe(BF_4)_2 \cdot 6H_2O$ with BTZP in the ratio of 2:1. The cyclic voltammetry data of the complex showed four nearly perfect ligand-based redox processes when compared to the redox properties of the ligand itself. Almost at the same time, the Caulton group published another BTZP-based complex with vanadium (III) as a starting material, and it is interesting to note that this reaction yielded a vanadium (IV) metal ion, which was antiferromagnetically coupled to the tetrazinyl radical.[94]

Figure 1.6 presents another example of BTZP employed in first row transition metal coordination chemistry in order to explore the intramolecular redox chemistry. The reaction of CuCl with the same equivalents of BTZP in MeCN yields the complex (BTZP)CuCl, which is a chloride-bridged polymer in the solid state. DFT calculations show that the electronic structure indicates that one electron from the ground state Cu(I) has been transferred to a π^* orbital. EPR, chemical reactivity, and X-ray photoelectron spectroscopy results are also used to confirm the presence of a ligand-centered radical. [95]

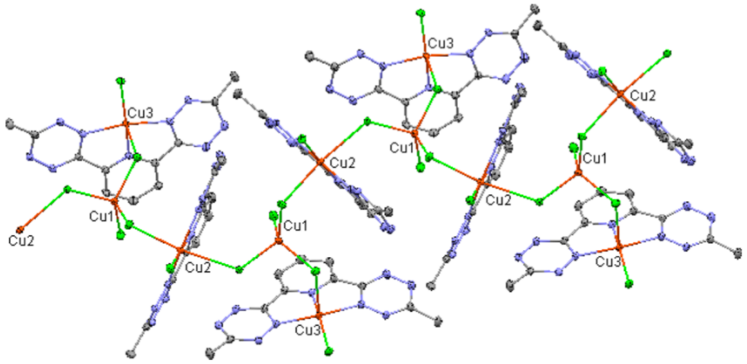

Figure 1.6. The (BTZP)CuCl polymer chain, showing the repeating unit. Shaded unlabeled atoms are nitrogen. Note the orientation of the tetrazine nitrogen lone pairs away from copper.[95]

1.4.2 Coordination chemistry of BTP

One of the main reasons that the coordination chemistry of BTP has remained less explored is the poor solubility of the ligand in most solvents.[96] BTP was first reported in 1999 as a candidate to broaden the synthetic scope for developed hetero [4+2] cycloaddition reactions between a series of tributyl(ethynyl)tin and 1,2,4-triazines. This method opened a new and very efficient route to synthesize a family of 1,2,4-triazines, leading to access to a variety of triazine based ligands which are interesting starting compounds for coordination chemistry.[92]

After that, BTP has been employed to great success in lanthanide coordination chemistry. Figure 1.7 shows the first solid-state structure synthesized which uses BTP in homometallic 12-coordinate complexes formed with praseodymium (III) and neodymium (III). The preparation of desired product is performed by adding BTP dissolved in MeCN dropwise with stirring to $Ln(NO_3)_3$ in MeCN. The solution was filtered after stirring for 15 minutes and crystals were formed by slow evaporation. However, there is no further characterization data reported in this paper. [90]

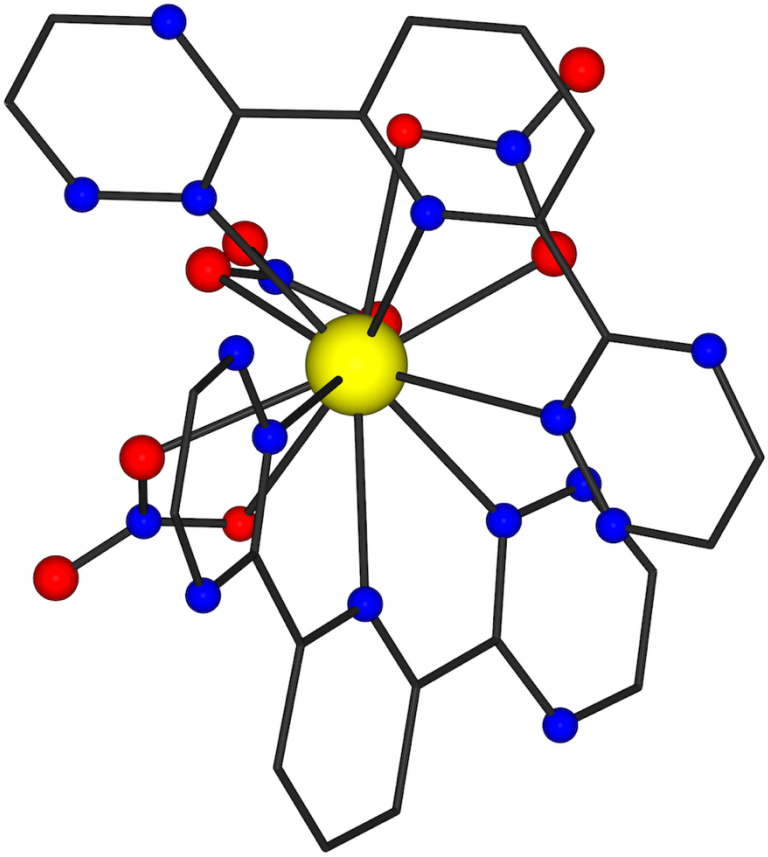

Figure 1.7. Structure of $[Ln(NO_3)_3(BTP)_2]$ (Ln = Pr^{III} and Nd^{III}), reported by Boucher and coworkers. H atoms are omitted for clarity. Color code: yellow (Ln), blue (N), red (O) and black (C). Reproduced from Boucher and co-workers.[90]

BTP has also been used in dimeric lanthanide coordination chemistry. In 2013, Bhattacharyya and coworkers presented a series of crystal structures with the use of both BTP and its derivatives in order to understand the effect of the nitrate ion on their complexation behavior.[96] The synthesis was performed in a similar manner from the above example. However, the final product that formed was $[Eu_2(BTP)_2(NO_3)_6] \cdot 2MeCN$ (Figure 1.8). Those complexes were found to show the formation of lower stoichiometric complexes in the presence of excess nitrate ion. DFT calculations also predict the structures observed experimentally. This work displayed a series of luminescence results such as time-resolved laser-induced fluorescence spectroscopy and UV−vis spectrophotometric titration, but no magnetic data. It would be interesting to see other lanthanides and BTP-based complexes in terms of both in luminescence and magnetism.

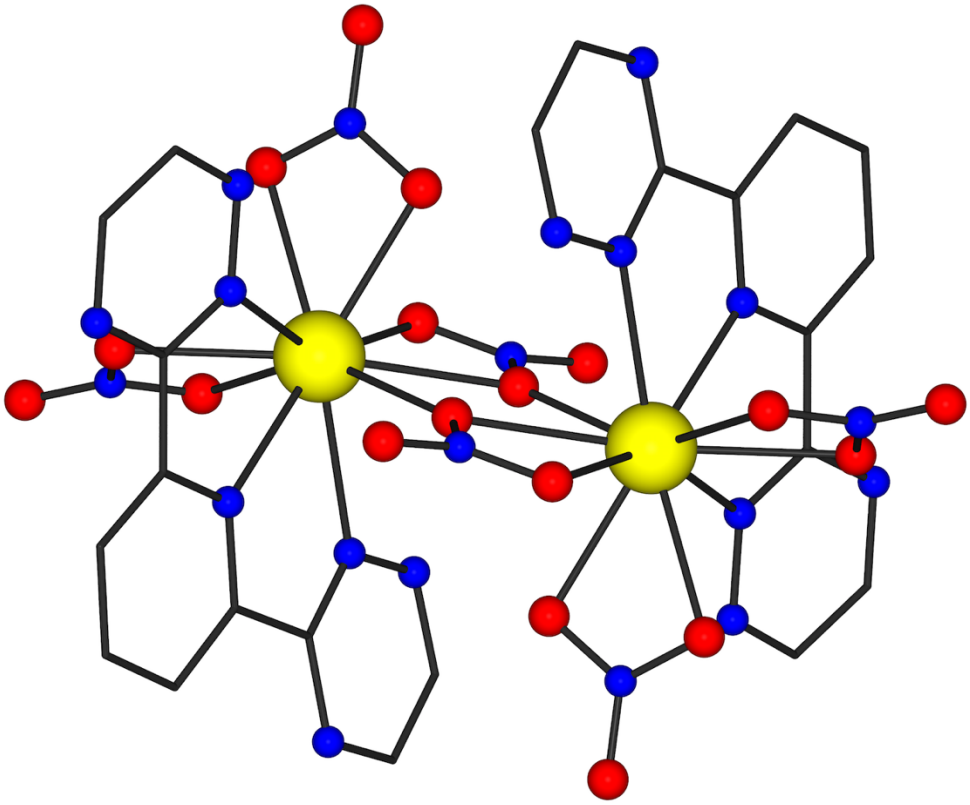

Figure 1.8. Structure of $[Eu_2(BTP)_2(NO_3)_6] \cdot 2MeCN$, reported by Bhattacharyya and coworkers. H atoms are omitted for clarity. Color code: yellow (Eu), blue (N), red (O) and black (C). Reproduced from Bhattacharyya and coworkers.[96]

1.5 Project goal

In order to obtain a strong magnetic exchange coupling between transition metal and radicals, the ligand design would have to incorporate a moiety that readily undergoes a one-electron redox process to form a radical species. BTZP and BTP appear to be the most promising candidates for this role since they not only undergo reversible one-electron reductions to form anion radicals, but they also exhibit remarkable stability coordinated with metal ions. Since BTZP was determined to be reduced during the coordination process with vanadium under atmosphere conditions, we wondered if we could observe the same phenomena in the other first row transition metals. In addition, BTP has a relatively similar structure with BTZP, so it might have the potential to act as a radical as well. Hence in this thesis project, we aim to study the BTZP and BTP ligand and investigate their coordination chemistry with a series of transition metals. To accomplish this

long-term goal, the project was divided into several short-term research objectives. These objectives are as follows: (a) synthesis and characterization (through NMR) of both BTZP and BTP ligands. (b) the synthesis and structural characterization (through single-crystal X-ray crystallography) of first row transition metals with both BTZP and BTP complexes. (c) the complete spectroscopic and electrochemical characterization of all synthesized compounds to determine which complex has potential to be reduced and which reducing agent should be employed; and (d) the performance of dc and potentially ac magnetic susceptibility studies to analyze the bulk magnetic properties of the compounds, as well as the spin states. Further goals are for the isolation of coordination complexes with both ligands possessing a radical state.

2 Synthesis and characterizations in the molecular and supramolecular arrangements of transition metal complexes with a 2,6-bis(6-methyl-1,2,4,5-3-yl) pyridine ligand.

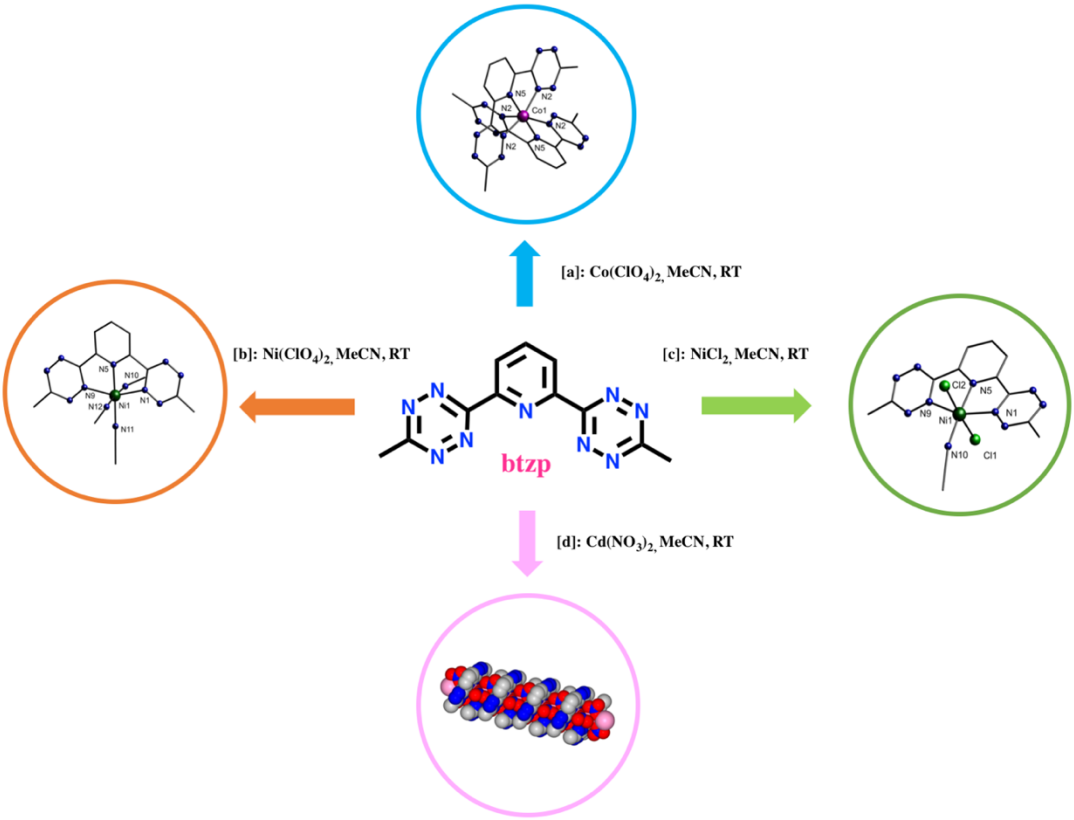

Abstract

A series of first and second row transition metal complexes, namely, $[Co^{II}(BTZP)_2](ClO_4)_2 \cdot 3MeCN$(**1**), $[[Ni^{II}(BTZP)(MeCN)_3](ClO_4)_2]$ (**2**), $[Ni^{II}Cl_2(BTZP)(MeCN)] \cdot 2MeCN \cdot H_2O$ (**3a**), $[Ni^{II}Cl_2(BTZP)(MeCN)] \cdot MeCN$ (**3b**), $\{[Cd^{II}(NO_3)_2(BTZP)]\}_n$ (**4**) was prepared from 2,6-bis(6-methyl-1,2,4,5-3-yl) pyridine (BTZP), an inherently redox active tridentate ligand, with various Co(II), Ni(II) and Cd(II) salts. Particularly, the crystal structure of **1** reveals a classic $[CoN_6]^{2+}$ inorganic core with coordination through a tridentate 'terpy-like' pocket. Moreover, there is Jahn-Teller compression that can be observed. Furthermore, complexes **2** and **3** showed a perfect octahedral geometry with only one BTZP ligand coordinated in a tridentate manner, with three more weak field ligands that are coordinated to the central metal in a monodentate manner. In the contrast, the polymer **4** results in a completely

different supramolecular arrangement and it has a μ-nitride bridge with repeating unit of [Cd^{II} (BTZP)$(NO_3)_2$]. Consequently, the spectroscopic behaviour of polymer **4** are significantly different with **1, 2** and **3**. The electrochemical results show that complex **1** exhibited four reversible or partially reversible ligand based redox process while complex **2** and **3** both exhibited two irreversible reduction process. In terms of magnetic properties, complex **1** remain low spin, complex **2** and **3** are both S=1, while complex **4** is diamagnetic.

2.1 Introduction

In recent years, the design and development of organic chelating ligands with nitrogen containing heterocycles have received a significant deal of interest for their suitability in a variety of applications, from functional materials to catalysis.[93, 97-100] In that regard, heterocycles containing tetrazine moieties are quite attractive, as it has highly electron-deficient π system in the tetrazine ring. The reason is that each tetrazine ring has four nitrogen atoms which lower the π^* orbitals, leading to the tetrazine moiety to act as strong π-acceptors. These unique properties of tetrazines offer great opportunity to have a wide variety of applications. Such applications include, but are not limited to, bioconjugation,[101] luminescence,[102] visible light photocatalysiscatalysis,[103-105] energetic materials,[106] as well as electron storage.[84] Tetrazine radicals also possess a high degree of stability,[55, 107] which can be represented as follows:

$$K_c = \frac{[M^{\bullet -}]}{[M^{2-}][M]} = 10^{\frac{\Delta E}{59\,(mV)}}$$

Where K_c is comproportionation constant and ΔE is the potential difference between the 0/•- and •-/2- redox couples. For tetrazines, these values can be greater than 10^{108} whereas with other azine-type ligands such as 2,2'-bipyrimidine the values of K_c are often several orders of magnitude lower.[109]

Recent attention has turned from the metal-centered redox process, as tetrazine ligand can transfer the additional electron density to the metal, allowing a tetrazine radical to be stabilized by the metal complex as a whole.[55] This design can have further functionalities, such as air stable radicals,[110] molecular switches,[111] single molecule magnets (SMMs),[112] electrocatalytic process,[113] and single-electron transfer (SET).[114] However, coordination complexes which include radical ligands normally have a very short lifetime. This has given rise to a big challenge for us to

understand the principles behind it, through a variety of characterization methods. Fortunately, in coordination chemistry, chelate effect can stabilize transition metal complexes. Chelation results in the formation of four- to six-membered rings which stabilizes the complex. In order to achieve such behavior, it is necessary to introduce a highly coordinating pocket into the tetrazyl-based radical framework. For example, to date, one of the most widely studied ligand systems is 2,2';6',2''-terpyridine (terpy).[53, 115] With respect to this, we have focused our attention on the synthesis and coordination chemistry of 2,6-bis(6-methyl-1,2,4,5-3-yl) pyridine (BTZP), which provides an ideal "terpy-like" tridentate coordination pocket, as well as the incorporation of nitrogen rich tetrazines at the 2 and 6 positions of the central pyridine ring.

Solid-state structures of BTZP complexes have been previously reported only with first row transition metals such as vanadium, iron and copper.[57, 84, 94, 95] Hence in this paper, for this first time we not only report the solid-state structures of a family of cobalt and nickel discrete molecules to fill in the row of 3-d transition metals, but also reveal a second row transition metal (cadmium) complex of BTZP and more importantly, we investigated the spin-states of all the complexes through magnetometry. In this series, the complex with cobalt has a $[Co^{II}(BTZP)_2]^{2+}$ formula with coordination through the tridentate 'terpy-like' pocket.[116] Additionally, two nickel complexes have a similar structure with $[[Ni^{II}(BTZP)(MeCN)_3]^{2+}$ or $[Ni^{II}Cl_2(BTZP)(MeCN)]$ with only one BTZP coordinated to the center metal and three monodentate weak-field ligands to achieve the octahedral geometry. Finally, the cadmium complex showed a supramolecular arrangement to form a 1-D polymer chain with repeating unit of $[Cd^{II}(BTZP)(NO_3)_2]$. We have structurally characterised all derivatives of BTZP and completed their cyclic voltammetry analysis as well as investigated the spin-states of the complexes through magnetometry.

2.2 Experimental

2.2.1 Materials and methods

All the chemicals used in the synthesis were from commercial sources and used as received, without further purifications.

2.2.2 Synthesis of 2,6-dicyanopyridine

2,6-dicyanopyridine was synthesized as previously reported.[84] 2,6-dibromopyridine (5 g, 21 mmol), copper(I) cyanide (3.0 g, 33 mmol) and sodium cyanide (2.2 g, 45 mmol) were mixed

in 20 mL of dry dimethylformamide (DMF). The solution was heated to 140 °C in an oil bath and refluxed under N_2(g) for 12 hours. Upon cooling to room temperature, 20 mL of concentrated sodium cyanide solution in water was then used to dissolve the excess copper (I) complex. A brown solid was precipitated upon addition of 100 mL of water. The resulting mixture was filtered by suction filtration with silica and washed with chloroform. The filtrate was collected and extracted with chloroform (3 x 100 mL). The combined organic extracts were collected and washed with brine (10 x 100 mL). The organic extracts were then evaporated to dryness, yielding a white crystalline solid which was collected and dried *in vacuo.* Yield: 2.35g, 87%. ^{1}H NMR (25 °C, 300 MHz, $CDCl_3$): δ 8.04(t, *J* = 8.0HZ, Ar-p, 1H), 7.90(d, *J* = 8.0HZ, Ar-m, 2H).

2.2.3 Synthesis of the bis-tetrazine ligand (BTZP)

The ligand synthesis is followed by the previous reported modified procedure and exhibits spectral data identical to a previous report.[84] To a solution of 2,6- pyridinedicarbonitrile (0.520 mg, 4.03 mmol) in ethanol (25 mL) to give a yellowish slurry. To this beige mixture, hydrazine monohydrate (10 mL, 205 mmol) was added while stirring and the solution was heated to 55 °C for 4 h until a white precipitate was observed. 25 mL of MeCN (473 mmol) and 0.40 g (12.47 mmol) sulphur were added rapidly and the colour changed immediately to green and then brown. The reaction was refluxed for 12 h and an orange solution was observed. The solution was allowed to cool to room temperature and the solvent was removed *in vacuo*. The resulting solid mixture was washed by CS_2 solution 3 x 15 mL to remove sulphur residues and dried *in vacuo*. 15 mL 1-methy-2-pyrrolidinone was added into the solid mixture, stirring for 15 minutes in the ice bath. Excessed NO_2 gas was generated by dissolving 50 g of copper powder in 50 mL of concentrated HNO_3. The gas was bubbled in the previous solid mixture for 30 min. Ice cold water was added to the solution which a large amount of pink powder participated out which can be filtered and washed with cold water, dried under vacuum to obtain crude product. This pink crude product was evenly placed on silica gel column (230-400 mesh) packed with CH_2Cl_2. The first fraction is collected with CH_2Cl_2 and discarded. The rest column was run varying from pure CH_2Cl_2 to CH_2Cl_2: MeCN 7:3. Isolated yield: 46.4%. 1H NMR (25 °C, 400 MHz, $CDCl_3$) δ 8.82 (d, *J* = 10 Hz, 2 H) 8.27 (t, *J* = 10 Hz, 1 H) 3.17 (s, 6H). ^{13}C NMR (25 °C, 100 MHz, $CDCl_3$) 163.1, 153.6, 150.8, 150.1, 139.3, 126.0 ppm. Selected IR (ATR, cm^{-1}): 3084.03(w), 1979.97(w), 1578.86(m), 1459.40(m), 1389.47(m), 1358.24(m), 1305.29(w), 1263.66(w), 1204.19(w), 1167.42(w),

1120.79(s), 1087.44(m), 1060.78(w), 1035.61(w), 992.42(w), 892.19(s), 849.48(m), 788.72(w), 745.75(m), 655.44(w), 614.81(s), 599.91(s), 588.02(s), 569.87(s), 560.23(m), 552.57(m), 537.28(w).

2.2.4 Synthesis of the $[Co^{II}(BTZP)_2](ClO_4)_2 \cdot 2MeCN$ (1)

To a pink solution of BTZP ligand (33.37 mg, 0.125 mmol) in acetonitrile (10 mL) was added $Co(ClO_4)_2 \cdot 6H_2O$ (45.74 mg, 0.125 mmol). After being stirred for 5 minutes the suspension turned to black. The filtered solution was placed into a diethyl ether bath for crystallization. Black cube-like crystals of **1** were collected by filtration after 2-3 days (yield = 30% based on $Co(ClO_4)_2$). Elemental Analysis; Calculated: C, 32.39; H, 2.45; N, 29.41. Found: C, 32.31; H, 2.43; N, 29.26. Selected IR (ATR, cm-1): 3079.34(w), 2322.92(w), 2168.80(w), 2049.85(w), 1980.02(w), 1682.51(w), 1608.82(w), 1581.13(m), 1552.20(w), 1510.15(w), 1494.11(s), 1472.32(s), 1453.31(m), 1439.32(w), 1394.94(s), 1359.13(m), 1322.43(m), 1279.33(m), 1172.78(w), 1087.93(s), 995.59(w), 960.15(w), 919.70(m), 835.21(m), 788.13(m), 748.01(m), 680.08(w), 623.37(s), 599.25(w), 573.47(s), 564.28(s), 554.68(m), 534.70(m), 526.52(m).

2.2.5 Synthesis of the $[Ni^{II}(BTZP)(MeCN)_3](ClO_4)_2$ (2)

To a pink solution of BTZP ligand (33.37 mg, 0.125 mmol) in acetonitrile (20 mL) was added $Ni(ClO_4)_2 \cdot 6H_2O$ (45.71 mg, 0.125 mmol). After being stirred for 10 minutes the suspension turned dark orange. The filtered solution was placed into a diethyl ether bath for crystallization. Orange needles-like crystals of **2** were collected by filtration after 2-3 days (yield = 42% based on $Ni(ClO_4)_2$). Elemental Analysis; Calculated: C, 21.63; H, 2.78; N, 17.8. Found: C, 21.91; H, 2.81; N, 17.54. Selected IR (ATR, cm^{-1}): 3421.10(w), 3106.24(w), 2321(w), 1979.82(w), 1606.73(w), 1492.64(m), 1443.57(w), 1396.14(s), 1363.87(w), 1326.88(w), 1284.79(w), 1172.19(w), 1075.11(s), 1029.95(m), 913.13(m), 865.09(w), 838.95(w), 802.90(m), 791.27(m), 746.06(w), 694.94(w), 621.88(s), 529.54(w).

2.2.6 Synthesis of the $[Ni^{II}Cl_2(BTZP)(MeCN)] \cdot 2MeCN \cdot H_2O$ (3a)

Complex **3a** was synthesized in an analogous manner to complex **2**, where BTZP (0.125 mmol, 33.37 mg) and $NiCl_2 \cdot 6H_2O$ (0.125 mmol, 29.71 mg) were combined in 10 mL of MeCN. Orange powder precipitated out after few seconds and filtered put by suction filtration. The *block*-like crystals for polymorph **3a** was collected by recrystallization by using minimum CH_2Cl_2 with

ether diffusion (yield = 60% based on $NiCl_2$). Elemental Analysis; Calculated: C, 34.52; H, 3.03; N, 30.97. Found: C, 34.84; H, 3.17; N, 31.23. Selected IR (ATR, cm^{-1}): 3453.60 (w), 3061.63(w), 2976.41(w), 2315.80(w), 2288.50(w), 2249.15(w), 2161.68(w), 2050.19(w), 1980.00(w), 1596.95(w), 1441.00(m), 1390.16(s), 1370.97(s), 1356.66(s), 1319.30(s), 1279.16(m), 1153.09(m), 1116.73(s), 1089.78(s), 1071.34(m), 1031.56(s), 951.99(w), 907.44(s), 851.00(s), 797.93(s), 751.73(m), 693.07(w), 652.61(m), 600.45(s), 578.61(s), 568.64(m), 552.57(m), 542.24(m).

2.2.7 Synthesis of the $[Ni^{II}Cl_2(BTZP)(MeCN)]\cdot MeCN$ (3b)

BTZP (0.125 mmol, 33.37 mg), $NiCl_2\cdot 6H_2O$ (0.125 mmol, 29.71 mg) and MeCN (10 ml) were added to a 20 mL sealed glass scintillation vial. The resulting mixture was sonicated for 10 min and heated gradually to 90 °C over 4 h, followed by heating at 90 °C for 24 h. The system was gradually cooled to room temperature over a period of 12 h, resulting in orange *needle-like* crystals. These crystals were collected by suction filtration and air dried (yield = 80% based on $NiCl_2$). Elemental Analysis; Calculated: C, 30.99; H, 2.80; N, 27.80. Found: C, 30.94; H, 2.82; N, 27.68. Selected IR (ATR, cm^{-1}):3450.69(m), 3065.28(w), 2922.29(w), 2317.75(w), 2290.07(m), 2248.39(w), 2050.18(w), 1599.82(m), 1446.35(m), 1396.47(s), 1364.08(m), 1325.76(m), 1282.96(w), 1169.41(m), 1142.70(w), 1119.77(w), 1030.94(m), 912.64(m), 795.20(m), 834.66(w), 795.20(m), 751.53(w), 694.23(w), 602.63(w), 602.63(w), 557.65(m), 541.44(m), 526.95(w).

2.2.8 Synthesis of the $\{[Cd^{II}(NO_3)_2(BTZP)]\}_n$ (4)

Complex **4** was synthesized in an analogous manner to complex **2**, where BTZP ligand (33.37 mg, 0.125 mmol) and $Cd(NO_3)_2\cdot 6H_2O$ (40.06 mg, 0.125 mmol) were combined in MeCN (10 mL). Pink needles-like crystals of **4** (yield = 30%) were collected by filtration after several days. Elemental Analysis; Calculated: C, 26.38; H, 1.94; N, 29.68. Found: C, 26.03; H, 1.81; N, 29.43. Selected IR (ATR, cm^{-1}): 1592.59 (w), 1468.55(s), 1394.40 (m), 1359.04(m), 1321.19(s), 1164.26(w), 1136.09(s), 1116.91(m), 1088.49(m), 1026.75(s), 915.74(m), 864.12(w), 836.48(s), 800.77(m), 791.08(m), 744.65(m), 704.79(m), 691.32(w), 539.17(w).

2.2.9 Physical measurements

The solid state infrared spectra were recorded on a Thermo Scientific Nicolet 6700 FTIR spectrometer equipped with an ATR in the 4000-525 cm^{-1} range. ^{1}H and ^{13}C NMR spectra were obtained on a Bruker Avance 400 MHz spectrometer equipped with an automatic sample holder and a 5 mm auto tuning broadband probe with Z gradient at room temperature. Elemental analyzes were measured at the G.G. Hatch Stable Isotope Laboratory at the University of Ottawa using an Isotope Cube elemental analyser.

2.2.10 X-ray crystallography

Suitable crystals were mounted on a glass fiber. A Bruker APEX-II CCD device was used to collect unit cell and intensity data using graphite Mo Kα radiation (λ = 0.71073). The data reduction included a correction for Lorentz and polarization effects, with an applied multiscan absorption correction (SADABS). The crystal structure was solved and refined using the SHELXTL program suite. Direct methods yielded all non-hydrogen atoms, which were refined with anisotropic thermal parameters. All hydrogen atom positions were calculated geometrically and were riding on their respective atoms.

Table 2.1. Summary of the crystal structure data and refinement for compounds **1-4**.

	1	**2**	**3a**	**3b**	**4**
Formula	$C_{26}H_{24}Cl_2CoN_{20}O_8$	$C_{17}H_{18}Cl_2NiN_{12}O_8$	$C_{17}H_{20}Cl_2NiN_{12}O$	$C_{15}H_{15}Cl_2N_{11}Ni$	$C_{11}H_9CdN_{11}O_6$
Mr	874.48	648.02	538.06	478.97	503.69
Space group	$P4_2/nnm$	$P2_1/c$	$Pbca$	$P2_1/c$	$C2/c$
a/ Å	10.6584(7)	13.0842(4)	7.9749(2)	10.6321(6)	21.6185(15)
b/ Å	10.6584(7)	10.0734(3)	20.5772(5)	25.3188(13)	10.4533(7)
c/ Å	16.6186(13)	20.4775(6)	29.9279(8)	7.6738(4)	7.7115(5)
α°	90	90	90	90	90
β°	90	99.452(2)	90	96.152(1)	104.921(1)
γ°	90	90	90	90	90
V/ Å^3	1887.9(3)	1573.95(10)	4911.2(2)	2053.83(19)	1683.9(2)
Z	4	4	8	4	4
T/K	201	201	201	201	200
Radiation	Mo-Kα	Mo-Kα	Mo-Kα	Mo-Kα	Mo-Kα
Dx/ g cm^{-3}	1.538	1.617	1.572	1.549	1.987
Mμ/ mm^{-1}	0.671	0.996	0.582	1.232	1.359
R[a]$_1$ (reflections)	0.0344	0.0572	0.0617	0.0406	0.0270
ω R[a]$_2$ (reflections)	0.0991	0.2125	0.1414	0.0995	0.0606

[a] $R = R1 = \sum | |F_o| - |F_c| | / \sum |F_o|$; $wR2 = \{[w(F_o - F_c^2)^2] / [w(F_o^2)^2]\}^{1/2}$; $w = 1/[\sigma_2(F_o^2) + (ap)^2 + bp]$, where $p = [\max(F_o^2, 0) + 2F_c^2]/3$; and $Rw = [w(|F_o| - |F_c|)^2 / w|F_o|^2]^{1/2}$, where $w = 1 / \sigma^2(|F_o|)$.

2.2.11 Magnetic measurements

Variable temperature magnetic susceptibility and magnetization measurements were performed on a crushed polycrystalline sample of 1 using a Quantum Design MPMS-XL7 SQUID magnetometer equipped with a 7 T dc magnet, in the temperature range 1.8 - 300 K for dc applied fields up to 7 T. An *M vs*. *H* measurement was performed at 100 K to confirm the absence of ferromagnetic impurities. Diamagnetic corrections were applied to the sample holder and to the observed paramagnetic susceptibility of complex **1**-**4** using Pascal constants.

2.2.12 X-ray powder diffraction (XRPD)

The XRPD pattern for selected complexes were performed using a RIGAKU Ultima IV diffractometer, equipped with a Cu-Kα radiation source (λ = 1.541836 Å), scintillation counter and a graphite monochromator. Scanning of the 2θ range was performed from 5-50°. Initial molecular models were constructed in the Mercury 3.9 program. Compared with calculated patterns from single crystal X-ray data, the XRPD patterns were consistent in 2θ values with slight discrepancies in some intensities of peaks attributed to preferred orientation and some broad amorphous character present. Complex **2** and **3a** are amorphous, because of the lability of the structure. However, the structure of the sample was confirmed by comparison between the collected pattern and the simulated pattern from the single crystal XRD data of complex **1**, **3b** and **4**. (Figure 2.1- 2.3).

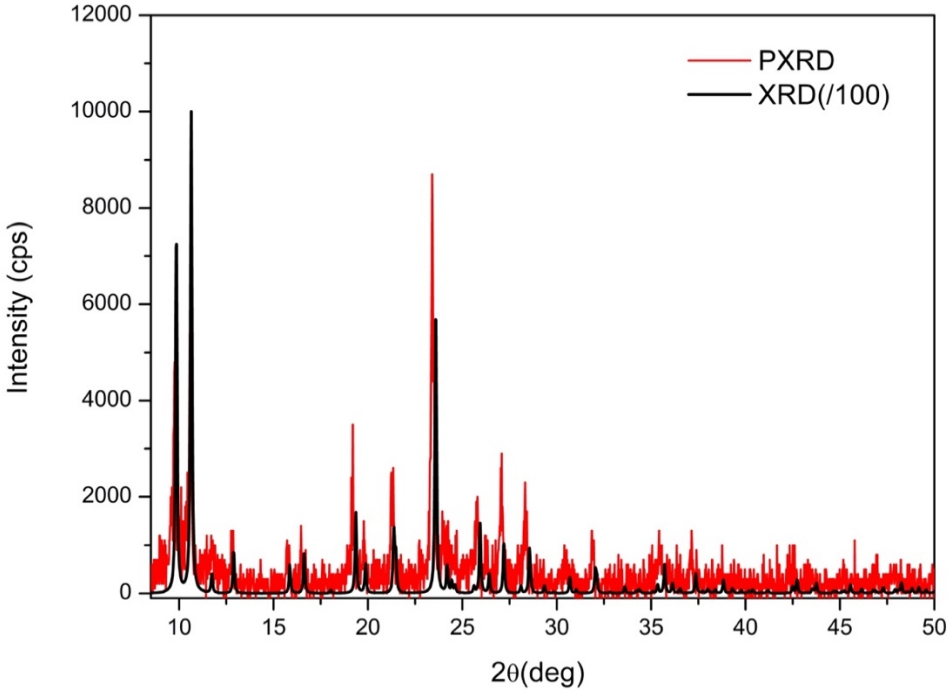

Figure 2.1. X-ray powder diffraction of $[Co^{II}(BTZP)_2](ClO_4)_2 \cdot 2MeCN$, **1**, (red) in the 5-50° 2θ region, as compared with the theoretical pattern generated from single crystal X-ray data (black).

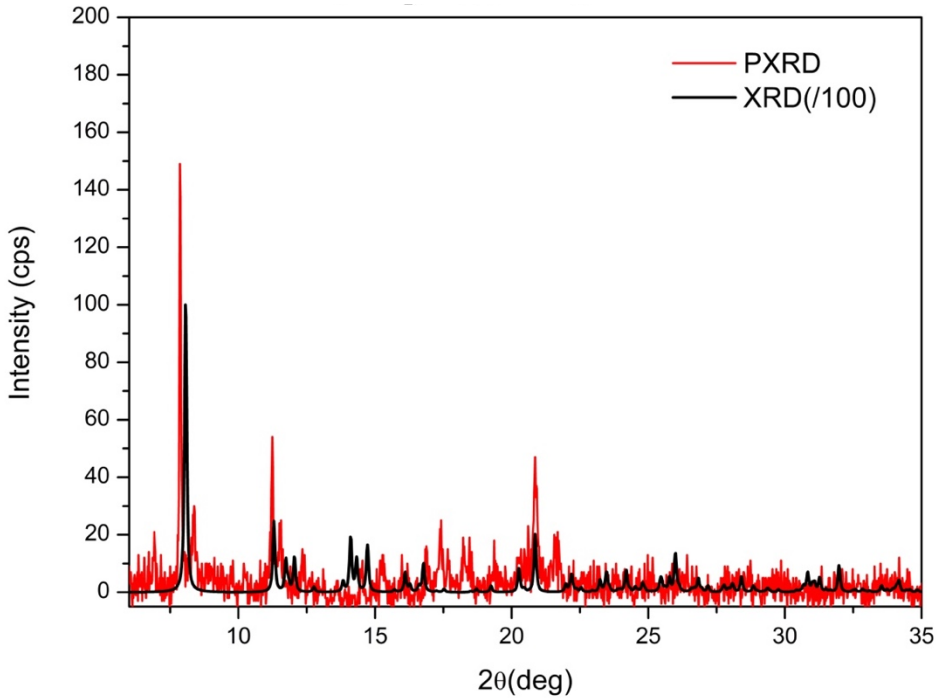

Figure 2.2. X-ray powder diffraction of $[Ni^{II}Cl_2(BTZP)(MeCN)] \cdot MeCN$, **3b**, (red) in the 5-50° 2θ region, as compared with the theoretical pattern generated from single crystal X-ray data (black).

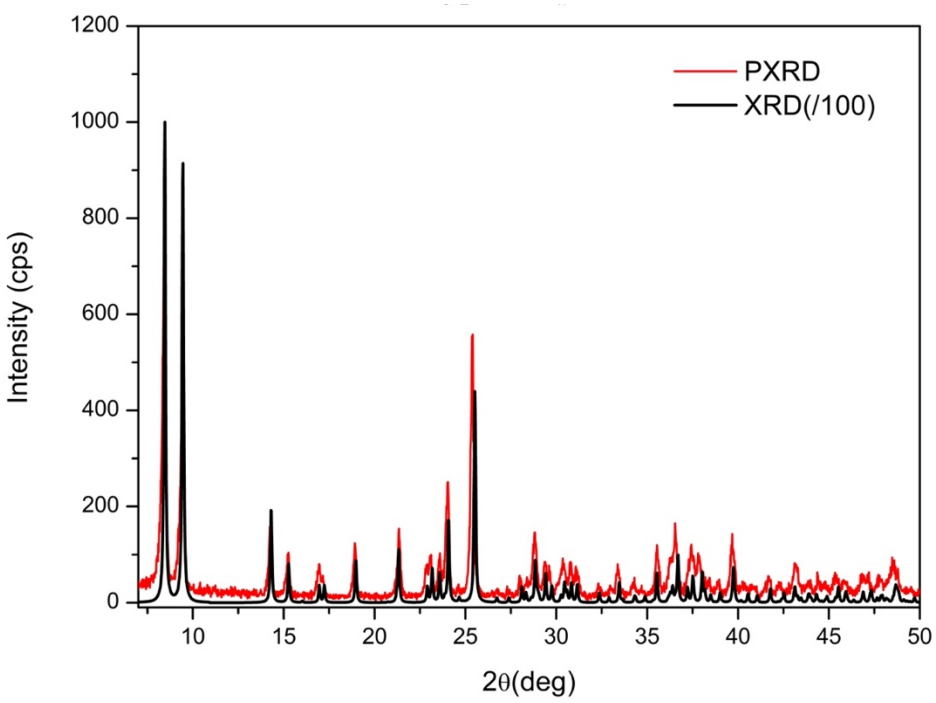

Figure 2.3. X-ray powder diffraction of $[\{[Cd^{II}(NO_3)_2(BTZP)]\}_n$, **4**, (red) in the 5-50° 2θ region, as compared with the theoretical pattern generated from single crystal X-ray data (black).

2.3 Results and discussion

2.3.1 Synthesis of BTZP ligand

2,6-bis(6-methyl-1,2,4,5-3-yl) pyridine (BTZP) was synthetized as previous reported. [84] The first step for the generation of this bis-tetrazine ligand involves the replacement reaction of bromide groups with cyanide groups on pyridine in DMF. There is a minor modification of the reaction conditions from the reported literature method, which changes the reaction temperature from 153°C to 140°C. The reason for this is that 2,6-dicyanopyridine has potential to decompose at high temperatures and under this modified condition, we could improve the yield to 87%. The remaining steps included the addition of hydrazine to 2,6-dicyanopyridine in EtOH, which forms pyridine-2,6-bis(carboximidhydrazide). The pyridine-2,6-bis(carboximidhydrazide) can further couple with MeCN when S_8 is present as a catalyst. After this step, the published synthesis of BTZP involves the addition of CH_3COOH and $NaNO_2$. However, we can only obtain very low yields because of the lability of BTZP ligand in the acid environment and moreover, it is time consuming to neutralize the reaction mixture by using Na_2CO_3 when synthesizing the ligand on a large scale. Consequently, we decided to investigate whether NO_2 gas could be used to directly synthesize

BTZP. With the generation of a large excess of NO_2 gas by reacting Cu and HNO_3,[117] we were able to close both tetrazine rings in the BTZP ligand. This molecule has a bright pink color, due to an n→π* transition, and indicates a small HUMO-LUMO gap in the molecule.[84] The ligand was used without any further purification for the complexation studies.

2.3.2 Synthesis and structure analysis for complex 1-4

As shown in Scheme 2.1, the synthesis of the complexes **1-4** were all performed in a similar manner, including the combination of various transition metal salts and BTZP ligand reacting in MeCN. These produced both mononuclear homoleptic complexes with ClO_4^- anions, heteroleptic mononuclear complexes with either extra coordinated three acetonitrile group or two chlorines & one acetonitrile group, as well as a supramolecular arrangement with 7-coordinated Cd^{II} center.

Scheme 2.1. Synthesis of compounds **1-4**.

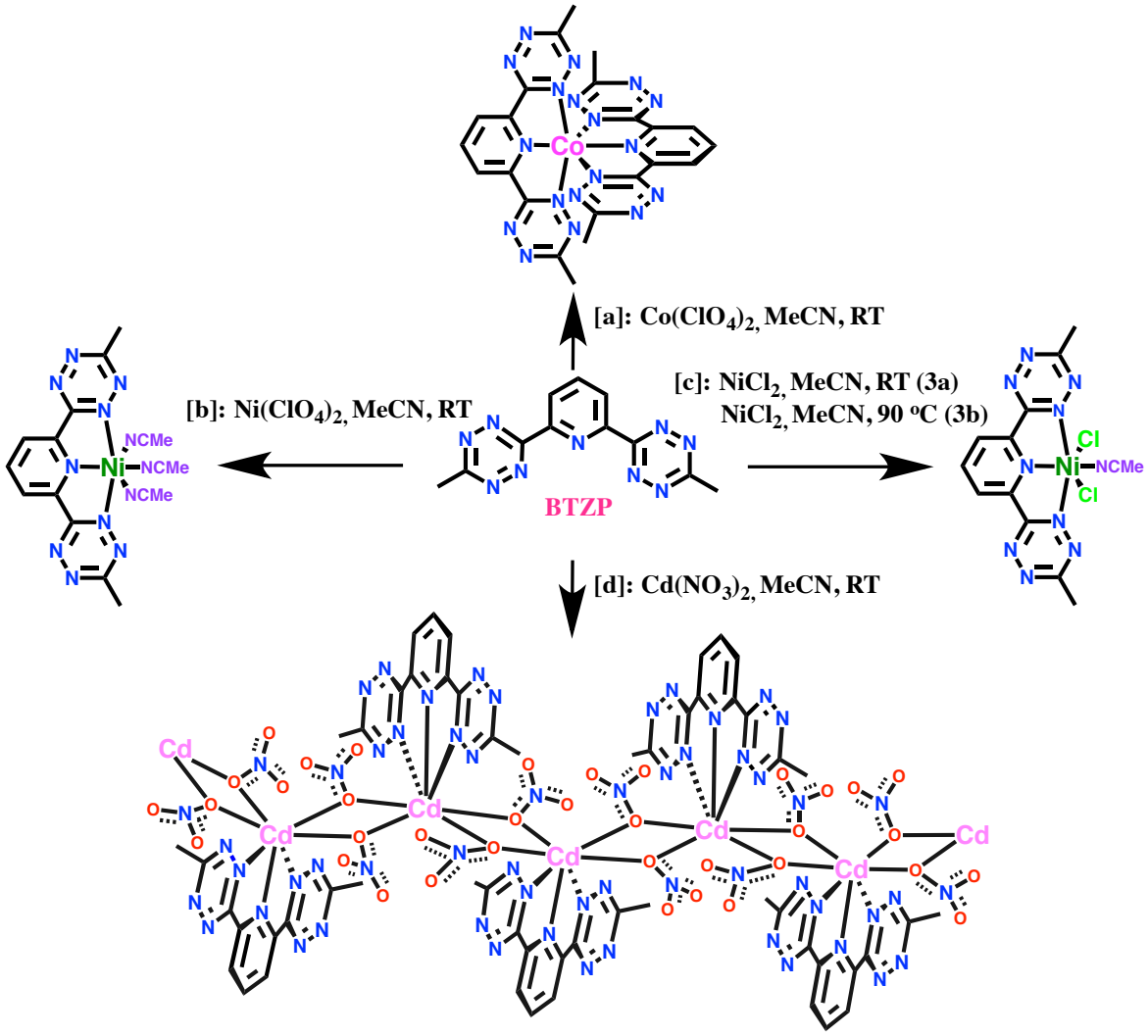

Complex $[Co^{II}(BTZP)_2](ClO_4)_2 \cdot 2MeCN$ (**1**) involved the combination of $Co(ClO_4)_2$ (1 equiv.) and BTZP (2 equiv.), stirring in MeCN for 5 minutes until all of starting materials dissolved. The reaction mixture was filtered by gravity and sealed in a vial with Et_2O for vapour diffusion, affording black block crystals after 2-3 days suitable for single crystal X-ray structures. Complex **1** crystallizes in the tetragonal $P4_2/nnm$ space group and the molecular structure is shown in Figure 2.4. The homoleptic complex is characterized by a 6-coordinate Co^{II} center, where the primary coordination sphere is completed with six N-atoms from two BTZP ligands. Both BTZP ligands have bite angles of 80.02° which results in the formation of a nearly perfect octahedral geometry (CShM = 2.14).[118] Interestingly, close inspection to the bond distance between Co-N, the shortest Co-N bonds are obtained for the central N-atom of the pyridine ring with the distance of 1.894(3) Å (Table 2.2). Moreover, the remaining Co-N bonds are shown as 2.022(2) Å. A similar Jahn-Teller compression phenomena is observed by other "terpy-like" compounds in the literature.[74, 100, 119-124] Intermolecular Co···Co distances were observed in **1**, with the smallest separation being 12.218(1) Å. Following bond valence sum (BVS) calculations these Co-N distances are most consistent with a Co^{II} oxidation state for the metal center, correlating with the charge balance of the species. Within the lattice, ClO_4^- ions form weak anion-π interactions with the 1,2,4,5-tetrazine components of the bound BTZP ligands. Such interactions keep consistent with the series of Fe^{II} /Co^{II} with BTP compound with similar structures. (*vide infra*). The ClO_4^- ions interact with 1,2,4,5-tetrazine ring composed of C2, N1, N2, C3, N4 and N3, such that a Cl-centroid distance of 3.38 Å is achieved. This distance is well within the van der Waals separation of 3.45 Å for C-Cl,[125] which suggests that a dominant electrostatic interaction exists between these moieties. The ClO_4^- ions in the complex **1** form tightly packed anion-π interactions, which leads to an extension of molecules in a *zig-zag* fashion along the c-axis and the inter-layer distance is 8.0 Å. Nerveless, the density of the materials is 1.538 $g.cm^{-3}$.

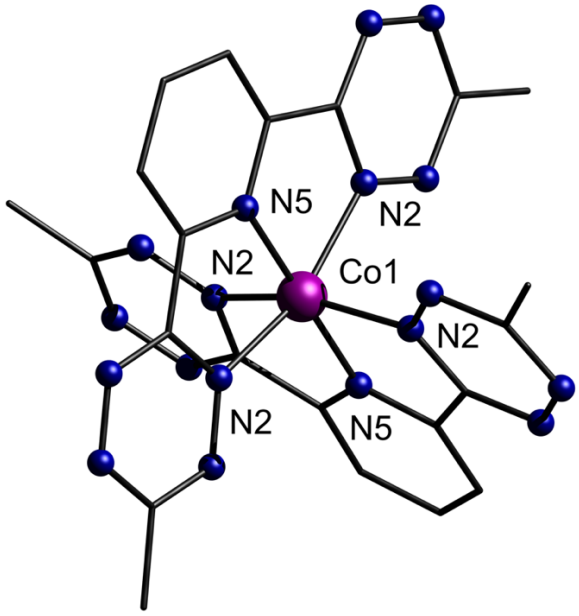

Figure 2.4. Partially labelled molecular structures of complexes $[Co^{II}(BTZP)_2]^{2+}$, **1**. Colour code: pink (Co), blue (N), and black (C). All of hydrogen atoms and solvent molecules are omitted for clarity.

Table 2.2. Selected bond distances (Å) for complex **1**.

Co1-N2	2.022(2)
Co1-N2#1	2.022(2)
Co1-N2#2	2.022(2)
Co1-N2#3	2.022(2)
Co1-N5	1.894(3)
Co1-N5#2	1.894(3)

Inspired by the structural insight of BTZP with Co^{II}, the coordination chemistry between Ni and BTZP was also explored by Ni^{II} precursors. Interestingly, the synthesis of the nickel derivative with the same ClO_4^- anions, which has a molecular formula of $[Ni^{II}(BTZP)(MeCN)_3](ClO_4)_2$ followed a similar route as the preparation of complex **1**. Namely, a MeCN solution of $Ni(ClO_4)_2$ was added into an MeCN solution of BTZP, stirring until all starting materials were dissolved. The reaction mixture was filtered and placed in a Et_2O bath for vapour diffusion at room temperature. Orange needle-shaped crystals suitable for single crystal X-ray analysis were obtained after several days. SCXRD analysis reveals that complex **2** crystallize in the monoclinic $P2_1/c$ space group. The overall crystal structure of **2** is totally different with complex

1, where the second BTZP ligand has been replaced by three acetonitrile groups, adopting in a 6-coordinate octahedral coordination mode. (CShM = 1.441) (Figure 2.5).[118] Close inspection of the Ni-N bond distances (Table 2.3), reveals the average Ni-N distance of 2.064 Å. Specifically, there exists a close distance between N4 of the 1,2,4,5-tetrazine ring and O4 of ClO_4^-. This anion-π interaction is an excellent indication of the elongated Ni-N1 bond and further supported by the Ni-N1 which is the largest Ni-N distance in the complex **2**. Intermolecular Ni···Ni distances were measured in **2**, with the smallest separation being 8.4578(6) Å. Nevertheless, these ClO_4^- ions are responsible for propagating a *zig-zag-like* packing arrangements of the complexes in the solid. This subsequently results the density of complex **2** at 1.617 $g.cm^{-3}$.

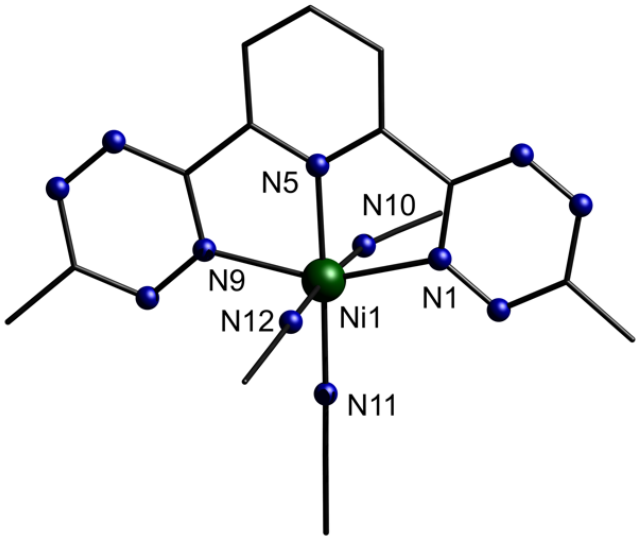

Figure 2.5. Partially labelled molecular structures of complexes $[Ni^{II}(BTZP)(MeCN)_3]^{2+}$, **2**. Color code: green (Ni), blue (N), and black (C). All of hydrogen atoms are omitted for clarity.

Table 2.3. Selected bond distances (Å) for complex **2**.

Ni1-N1	2.109(2)
Ni1-N5	2.0077(18)
Ni1-N9	2.144(2)
Ni1-N10	2.017(2)
Ni1-Nl1	2.3953(7)
Ni1-Nl2	2.3879(7)

As such, intrigued by the rich structural insights of BTZP with the Ni(II) and Co(II) with perchlorate precursors, halide derivatives were used to determine if the metal starting material had

an effect on the resulting structure. The synthesis was performed in a manner identical to complex **2**. Addition of $[Ni(H_2O)_6]Cl_2$ in MeCN to a solution of BTZP in MeCN, resulting in deep-orange, block shaped crystals of **3a**. Complex $[Ni^{II}Cl_2(BTZP)(MeCN)]\cdot 2MeCN \cdot H_2O$ (**3a**) crystalized in the orthorhombic space group *Pbca*, involving one coordinated BTZP ligand, one acetonitrile group and two chloride atoms with an octahedral coordination mode. For comparison, a solvothermal synthetic method was conducted in order to achieve a different polymorph of complex **3a**, resulting in complex **3b**. Namely, $NiCl_2$ (1 equiv.) and BTZP (1 equiv.) were combined in a sealed scintillation vial, heated by 90 ^oC for 24 hours and followed by 12 hours cooling, leads to the polymorph $[Ni^{II}Cl_2(BTZP)(MeCN)]\cdot MeCN$ (**3b**). Compound **3b** crystallizes in the monoclinic space group $P2_1/c$. The overall composition of compound **3** was determined as $[Ni^{II}Cl_2(BTZP)(MeCN)]$ (see Figure 2.6). The distance of complex **3a** and **3b** between Ni-N are almost the same, with the average of 2.07 Å, however, the longest distance in the coordination environment is Ni1-Cl1, at 2.3953(7) Å, suggesting that metal-ligand back donation may be dominant (Table 2.4).

While the packing arrangement of complexes **3a** and **3b** appear to be similar, the H_2O molecules in the complex **3a**, which participate in hydrogen bonds with chloride ligands from an adjacent non-parallel layer, result in a slightly denser packing arrangement and the closest distance between two parallel layers is 7.6738(6) Å. However, in the following **3b** case, there are π-π interactions that can be seen in the 1,2,4,5-tetrazine components of the bound BTZP ligands between each layer. This results in the formation of ribbon-like layers, with the closest distance between C atoms in the molecules above and below each other being 3.377(3) Å. Nevertheless, similar intermolecular Ni···Ni distances were observed in **3a** and **3b**, with the smallest separation being 7.5646(3) and 7.7415(3) Å, respectively. Since the metal complex portion of the structure of **3** behaves the same, UV-vis, electrochemistry and SQUID data are identical (*vide infra*).

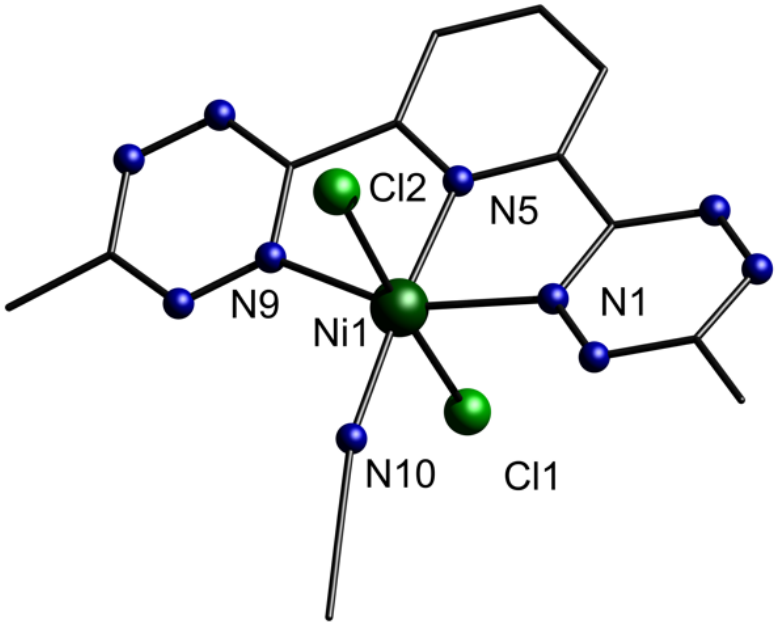

Figure 2.6. Representative example of complex $[Ni^{II}Cl_2(BTZP)(MeCN)]$, **3**. Colour code: olive green (Ni), light green (Cl), blue (N), and black (C). All of hydrogen atoms and solvent molecules are omitted for clarity.

Table 2.4. Selected bond distances (Å) for complex **3**.

3a		**3b**	
Ni1-N4	2.112(3)	Ni1-N1	2.109(2)
Ni1-N5	2.006(3)	Ni1-N5	2.0077(18)
Ni1-N9	2.099(3)	Ni1-N9	2.144(2)
Ni1-N10	2.022(3)	Ni1-N10	2.017(2)
Ni1-Cl1	2.3906(12)	Ni1-Cl1	2.3953(7)
Ni1-Cl2	2.4027(12)	Ni1-Cl2	2.3879(7)

Surprisingly, even though synthesis of the cadmium (II) nitrate derivative $\{[Cd^{II}(NO_3)_2(BTZP)]\}_n$ (**4**) was performed in a similar manner of the previous complexes, the product yields a 1-D coordination polymer (Figure 2.7 and 2.8). The reaction of Cd(II) nitride and BTZP results in a bright pink solution, which was filtered and put in a Et_2O bath for vapour diffusion. Suitable pink cubic crystals for single crystal diffraction formed after a week. Structure solution of **4** reveal a 1-D chain, and the molecule crystallizes in the monoclinic space group *C*2/*c*. This helical 1-D chain has the repeating unit which comprises a single BTZP ligand coordinated to one Cd(II) ion in its tridentate coordination mode, and the repeating unit is extended into the 1-D motif through the coordination of two NO_3^- anions. The three $N_{BTZP} - Cd^{II}$ distances are very close to each other,

with the shortest distance with N atom in the center pyridine (2.425(3) Å) and the two 1,2,4,5-tetrazine is the same again (2.472(3) Å). Each 7-coordinated Cd(II) ion is charge balanced by the presence of the two NO_3^- anions. Each nitrate ion is μ-bridging monodentate. SHAPE analysis reveals that Cd1 possesses an elongated triangular pyramid (C_{3v}) geometry (CShM = 9.612).[118] This leads to a repeat in the structure, linking individual $\{[Cd^{II}(NO_3)_2\,(BTZP)]^{2+}\}$ units together through two μ-O atoms, with Cd1-O1-Cd1=115.67^o to yield the 1-D chain structure of **4**. The central Cd_2O_2 core, appears to be nearly rhombic, with two Cd-O1 distance being 2.3450(17) and 2.4148(16) Å (Table 2.5). The shortest intermolecular Cd···Cd distance is 4.030(1) Å. It is also observed that there are strong π-π interactions can be seen in the 1,2,4,5-tetrazine components of the bound BTZP ligands between each metal center, resulting in linking the ribbon-like 1-D chain. The closet inter-chain contacts via C-H···N hydrogen bonds is 2.734 Å and there is also an extensive network of inter-chain C-$N_{tetrazine}$ short contacts (3.242 Å) between BTZP ligands. Nerveless, this packing arrangement results the density of complex **4** is 1.220 g.cm^{-3}.

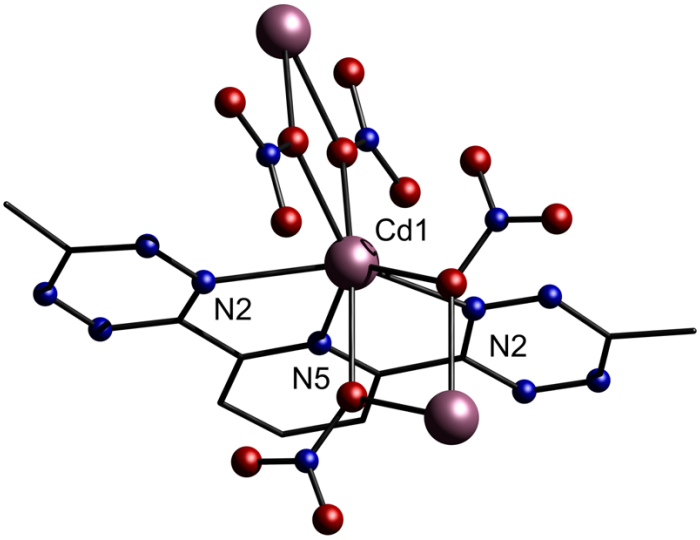

Figure 2.7. Partially labelled molecular structures of complexes $\{[Cd^{II}(NO_3)_2\,(BTZP)]\}_n$, **4**. Colour code: dark pink (Cd), blue (N), red (O) and black (C). All of hydrogen atoms are omitted for clarity.

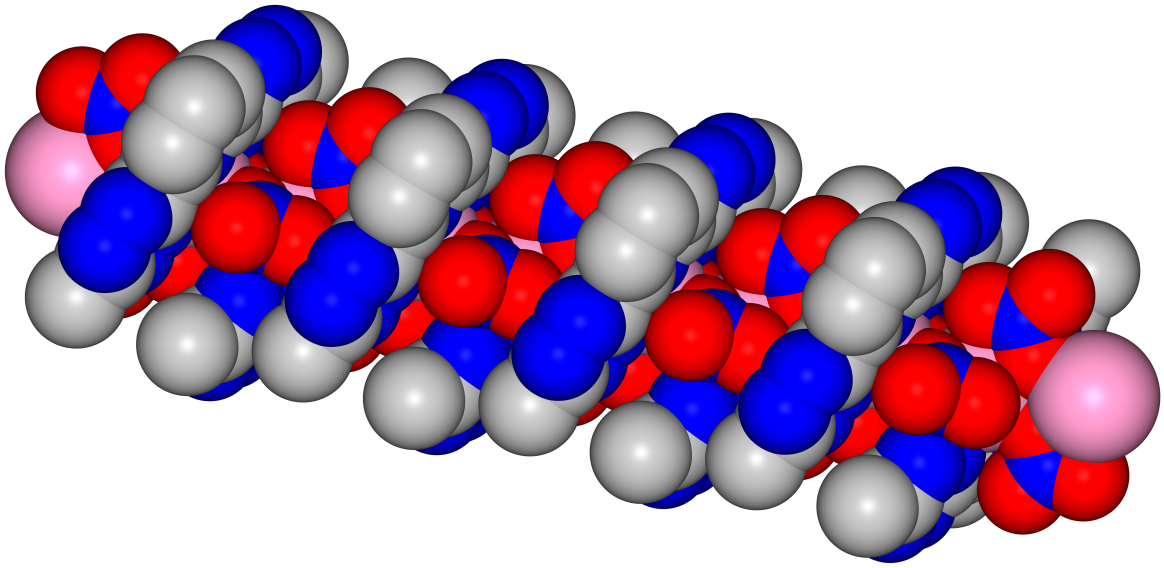

Figure 2.8. Self-assembling helical twist in the space fill supramolecular arrangement of the complex **4**. Colour code: dark pink (Cd), blue (N), red (O) and black (C). All of hydrogen atoms are omitted for clarity.

Table 2.5. Selected bond distances (Å) for complex **4**.

Cd1-N2	2.472(2)
Cd1-N2#1	2.472(2)
Cd1-N5	2.425(3)
Cd1-O2	2.3450(17)
Cd1-O2#1	2.3450(17)
Cd1-O2#2	2.4148(16)
Cd1-O2#3	2.4148(16)

2.3.3 UV-vis spectroscopy

In order to investigate the solid-state electronic structure of the ligand and its complexes, the pure solid materials were analyzed by diffuse reflectance spectroscopy at room temperature (Figure. 2.9). The free ligand presented visible absorptions at 555 and 247 nm, which correlates with the previously reported solution UV-vis absorption measurements completed in MeCN by Caulton and coworkers.[84] These peaks may be attributed to n$\rightarrow \pi^*$ and $\pi \rightarrow \pi^*$ transitions.[92] After the coordination process, the visible absorption at 247 nm that was present in the free ligand spectra was still visible, but the absorption at 555 nm disappeared. The diffuse reflectance spectrum of all of complexes also contains a shoulder at 927 nm, exclusively in the NIR region. The diffuse

reflectance spectra of the octahedral discrete complexes **1-3** are almost identical, showing the expected metal-ligand charge transfer (MLCT) absorptions in the range of 620-800 nm. [76, 126, 127] Notably, the complex **4** has another absorption at 590 nm and this can be probably attributed to the differences in the energy gap of HOMO-LUMO energy levels for octahedral and elongated triangular pyramid complexes.[128]

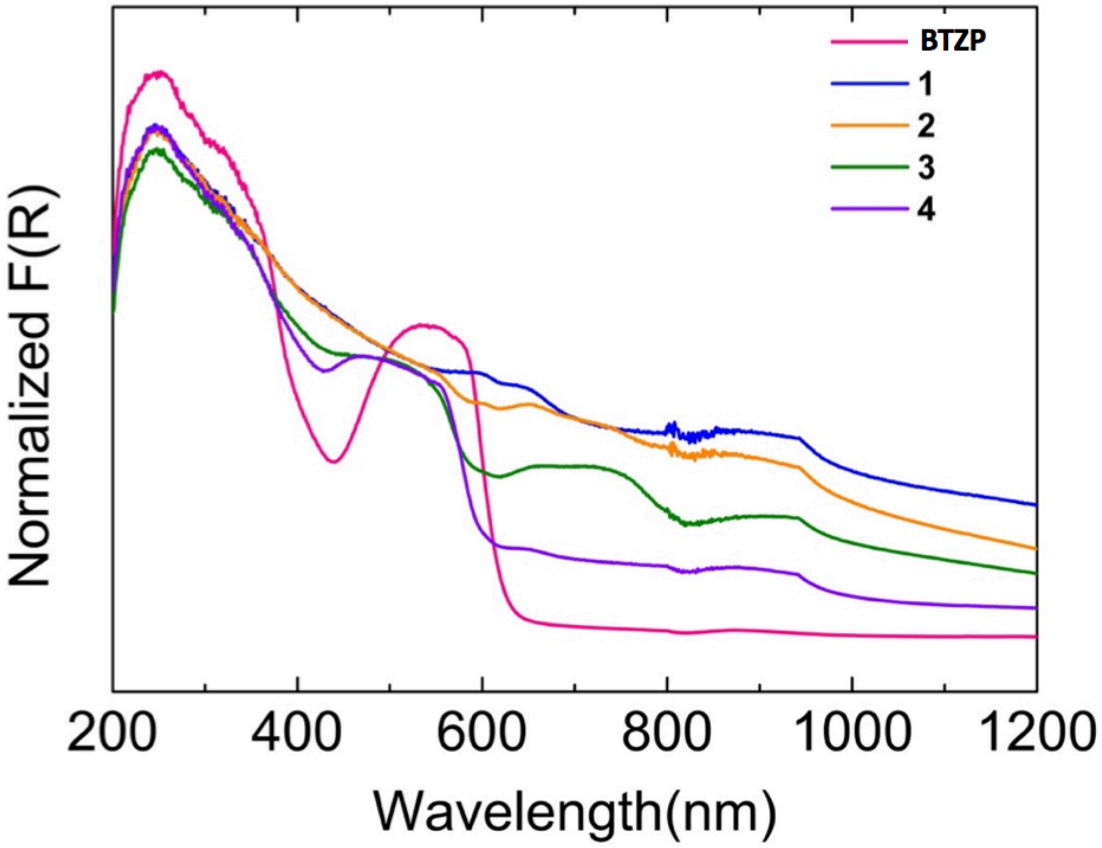

Figure 2.9. Normalized Kubelka-Munk spectra for BTZP and complexes **1-4**.

2.3.4 Electrochemical studies of complexes 1-4

In order to investigate the electrochemical properties of the BTZP complexes (**1-4**), cyclic voltammetry (CV) experiments were conducted in MeCN with 0.1 M Bu_4NBF_6 as supporting electrolyte and Fc/Fc^+ as an internal reference (*vide infra*). Caulton et.al group showed the CV data for the free BTZP ligand exhibiting a single reversible sharply-defined redox process with E_c = -850 mV *vs*. Ag/AgCl in MeCN, such that peak-to-peak potential separation (ΔE) was found to be 108 mV, with comparable i_{pc} and i_{pa}.[84] Nevertheless, for complexes **1-4** the complexity of the CV spectra was unexpected given the simplicity of the free ligand spectra. Most of the metal-centered

redox processes were reversible or partially reversible, falling in the range of -0.511 V < $E_{1/2}$ < 0.570 V *vs* Fc/Fc^+. In addition to these redox events, all of the complexes showed four or two redox active processes related to the ligand, which were either partially reversible or irreversible, ranging from -0.202 V to 1.961 V (Table 2.6).

Table 2.6. CV data for the complexes in this work (MeCN/0.1 M Bu_4NBF_6, 298 K). Potentials are quoted at a scan rate 0.1 V/s *vs.* an internal Fc/Fc^+ standard.

	M^{III}/M^{II} $E_{1/2}$, V	M^{II}/M^{I} $E_{1/2}$, V	Ligand-based reductions $E_{1/2}$, V
1	0.570	-0.129 [b]	-0.202, -0.787[a], -1.142[b], -1.361
2	-	-0.146	-0.611[b], -1.534[b]
3	-	0.521[c]	-0.772, -1.662[b]
4	-	0.161[c]	-0.577[a], -1.961[b]

[a] Partly chemically reversible, $E_{1/2}$ value quoted. [b] Irreversible process, E_c value quoted. [c] Irreversible process, E_a value quoted.

More specifically, the cyclic voltammetry results of **1** shows reversible redox properties (Figure 2.10). The first reduction of **1** in $[Co(BTZP)_2]^{2+}$ has the Co^{III}/Co^{II} redox couple at 0.570 V and the peak to peak potential separation (ΔE) was found to be 0.088 V demonstrating the expected pseudo-reversibility for the metal-based process of the complex. Additionally, there is a Co^{II}/Co^{I} reduction process at -0.129 V, which is common in the previous literature reports. [129] The lack of reversibility in the Co^{II}/Co^{I} reduction process is attributed to the instability of the Co^{I} cation in solution.[72] Interestingly, when it comes to ligand-based redox couples, there are four reducing process observed in **1**, which is comparable to the previous report. [84] Nevertheless, the ligand-based peaks for **1** revealed potentials of -0.202, -0.787, -1.142 and -1.361 V. Specifically, the peak at -1.142 V is an irreversible process due to the lability of the compound during the BTZP radical state. The rest of ΔE was found at 0.127 V, 0.038 V and 0.091 V demonstrating the reversible or partially reversible process. All the peaks appeared roughly equal and consistent with previous reports of $[CoN_6]^{2+}$ compounds.[130, 131] Increasing scan rates from 0.05 V/s to 3.2 V/s reveal the identical result.

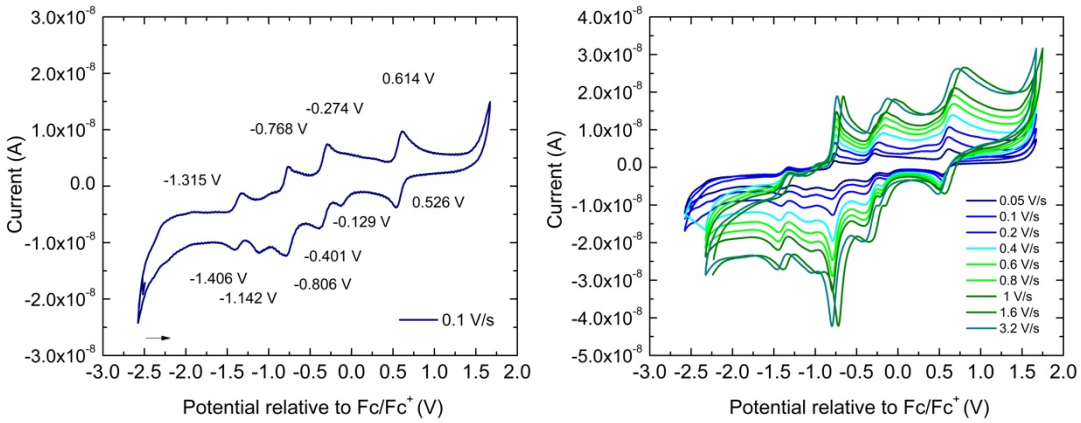

Figure 2.10. CV scan of $[Co^{II}(BTZP)_2](ClO_4)_2 \cdot 2MeCN$ (**1**) (blue line on the left) in MeCN solution (0.1 M $[Bu_4N][PF_6]$, 0.1 V/s) and multiple scans sweep rate from 0.05 V/s to 3.2 V/s (blue to green lines on the right). Black arrow indicates the direction of sweep.

Conversely, in the coming complex **2** case, Figure 2.11 shows that the Ni^{II}/ Ni^{I} couple characteristic of the octahedral $[Ni(BTZP)_2]^{2+}$ component shifted -0.146 V compared to **1** (*vide supra*). Peak to peak potential separation (ΔE) was found to be 0.106 V, demonstrating reversibility. The Ni^{II}/Ni^{I} redox chemistry of **2** is very similar to previously reported terpy analogue complexes.[123, 132, 133] However, there are only two ligand-based reduction process consist with **1**, which appear at -0.611, -1.534 V for complex **2**. The main reason is that there is only one BTZP ligand present in complex **2** and a single BTZP ligand potentially have up to 4 electrons capacity.[57] Unfortunately, due to the lability of **2** in MeCN, some of the oxidation peaks might not be observed during the experiment. It should be noticed that increasing scan rate from 0.05 V/s to 3.2 V/s can lead to the appearance of extra Ni^{III}/ Ni^{II} redox couple. Additionally, the previous peak of Ni^{II}/ Ni^{I} couple at -0.146 V disappeared. This may suggest that the BTZP radical state has potential to further decompose the coordination complex, increasing the lability of **2** in the solution. Furthermore, there is an oxidation peak at 1.099 V can be observed in the ligand based reduction process. However, the cyclic voltammetry results of **3** (Figure 2.12) show a single reduction process with E_a = -0.521 V and it is significantly more positive than complex **2**. Similarly, there are two ligand based reduction process with the potentials of -0.772 V and -1.662 V, respectively. It is notable that the peak at -0.772 V is partially reversible, with the peak to peak potential at 0.081V. These findings may suggest that compare to MeCN as a coordinated solvent, the Cl ligand allows for increased stability of **3** over **2**, which was found to be labile in solution in a previous

study.[134] Conversely, another oxidation peak of Ni^{II}/ Ni^{I} couple is observed at -0.511 V, which is attributed to Cl^-. Again, there is no significant difference for changing the sweep from 0.05 V/s to 3.2 Vs.

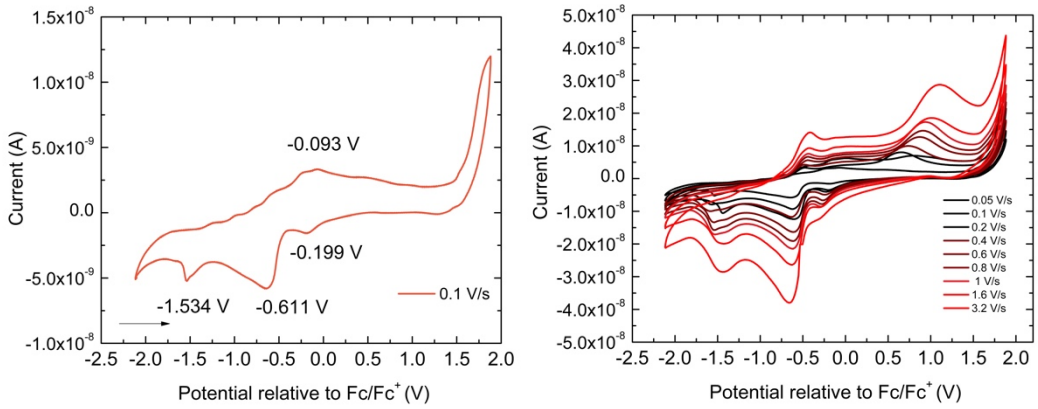

Figure 2.11. CV scan of $[Ni^{II}(BTZP)(MeCN)_3](ClO_4)_2$ (**2**) red line on the left) in MeCN solution (0.1 M $[Bu_4N][PF_6]$, 0.1 V/s) and multiple scans sweep rate from 0.05 V/s to 3.2 V/s (black to red lines on the right). Black arrow indicates the direction of sweep.

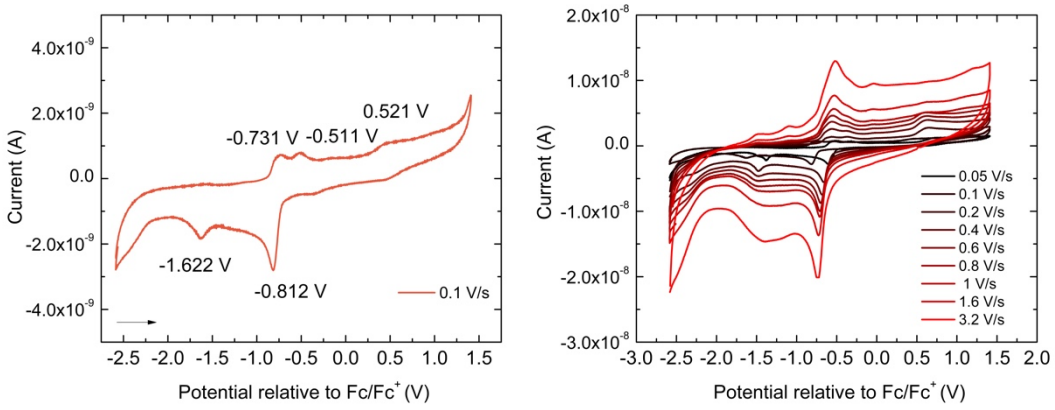

Figure 2.12. CV scan of $[Ni^{II}Cl_2(BTZP)(MeCN)]$ (**3**) (orange line on the left) in MeCN solution (0.1 M $[Bu_4N][PF_6]$, 0.1 V/s) and multiple scans sweep rate from 0.05 V/s to 3.2 V/s (black to orange on the right). Black arrow indicates the direction of sweep.

As for the Cd(II) 1-D chain, the Cd^{II}/Cd^{I} couple can be seen at 0.161 V, which is only slightly more negative than complex **2** (Figure 2.13). It is seen that there is a ligand-based partially reversible redox process showing at -0.577 V with peak to peak separation at 0.151 V. In addition,

another ligand-based reduction process appeared at -1.961 V, which is consistent with complexes **1-3** and previous reports. *(vide supra)*.[135] Surprisingly, the increased scan rate resulted in the extra Cd^{II}/Cd^{I} redox couple of compound **4** to be 0.397 V, and this is only slightly more negative than complex **3**. In addition, the ligand-based oxidation process disappeared at -0.501 V, which is consistent with complex **2** and **3**. This may be attributed to the decomposition of the polymer chain, because of the lability of BTZP radical state.

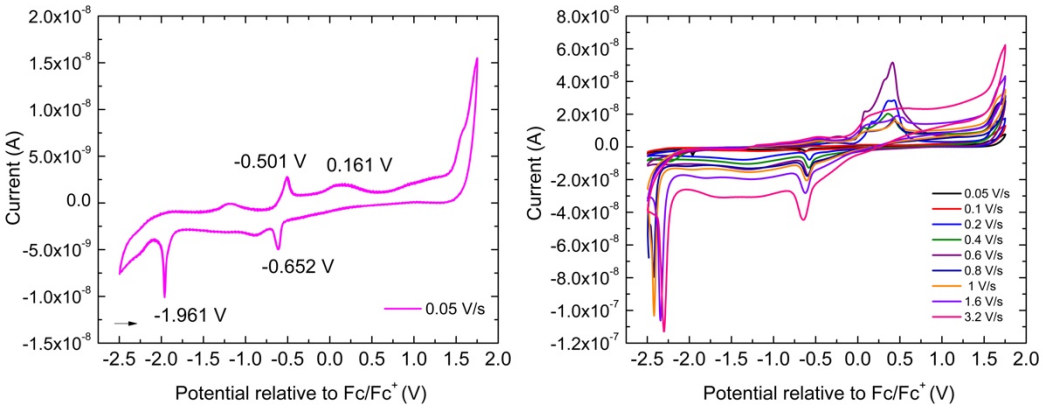

Figure 2.13. CV scan of $\{[Cd^{II}(NO_3)_2(BTZP)]\}_n$ (**4**) (pink line on the left) in MeCN solution (0.1 M $[Bu_4N][PF_6]$, 0.1 V/s) and multiple scans sweep rate from 0.05 V/s to 3.2 V/s (pink to black lines on the right). Black arrow indicates the direction of sweep.

2.3.5 Magnetic studies

In order to probe the magnetic properties of compounds **1-3**, dc magnetic susceptibility measurements were completed under a static field of 1000 Oe in the temperature range 1.8-300 K (*vide infra*). Under these conditions, an absence of signal was observed for compound **4**, confirming its diamagnetic electronic configuration. This is because of the metal center of complex **4** is diamagnetic. Conversely, compounds **1-3** exhibited paramagnetic behaviour, revealing χT values at 300 K of 0.55, 1.01, and 1.05 cm^3 K mol^{-1}, respectively (Figure 2.14).

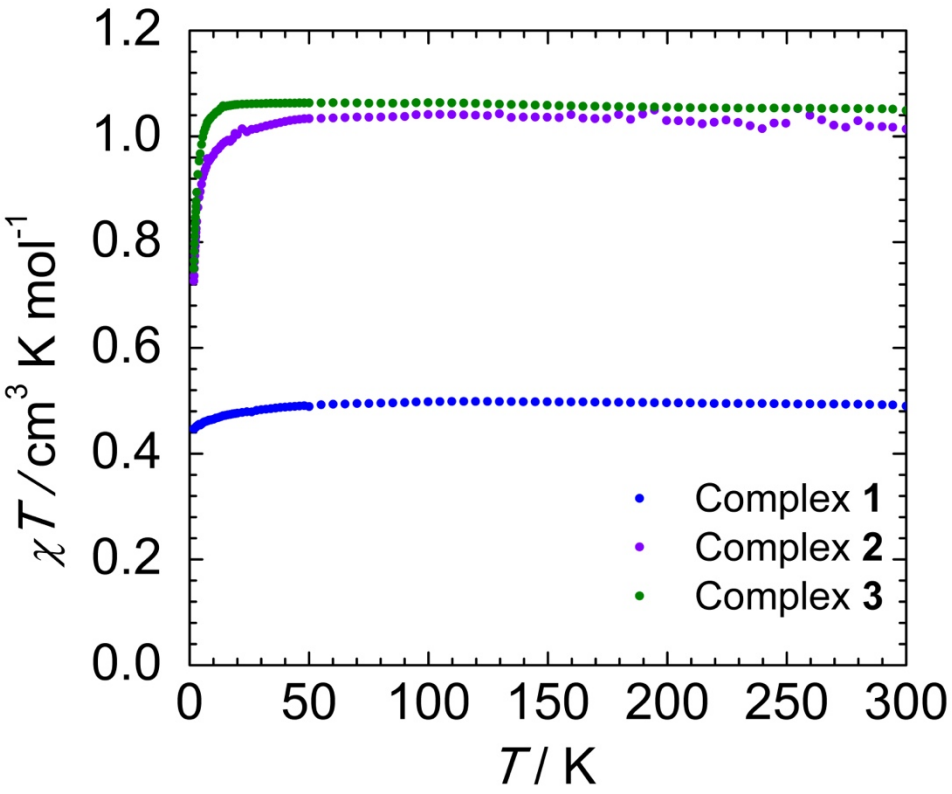

Figure 2.14. Temperature dependence of the χT product at 1000 Oe for **1**, **2** and **3**, with χ being the molar magnetic susceptibility per molecule as defined by M/H. Experimental data is represented by hollow circles.

To be specific, the room temperature χT value of 0.55 cm^3 K mol^{-1} for **1** is slightly larger than the expected low spin-only value of 0.375 cm^3 K mol^{-1} for cobalt discrete molecules (Figure. 2.14). It has been commonly seen in complexes of $[CoN_6]^{2+}$ magnetic core, with coordination through the tridentate 'terpy-like' pocket, have a strong ligand field. [71-73, 78, 136-138] Thus, given this information it is postulated that a low-spin configuration is imposed on the octahedral Co1 in complex **1**, resulting in spin states of $S = 1/2$ for Co1. At significantly low temperatures (< 5 K), there is a slight decrease to reach 0.45 cm^3 K mol^{-1} at 1.8 K for **1**. This downturn may be a direct consequence of the inherent orbital angular momenta of Co^{II} low spin ions, or the presence of weak intermolecular antiferromagnetic interactions. Moreover, at 1.9 K the magnetization saturates for **1** at 1.02 μ_B (Figure 2.15). which is in excellent agreement with the expected value for this spin system (1 μ_B), assuming g = 2. Additionally, the isotemperature reduced magnetization curves are

all super-imposed suggesting the absence of angular momentum, this is not surprising given that the low spin state is dominant in these systems at low temperature (Figure 2.15).

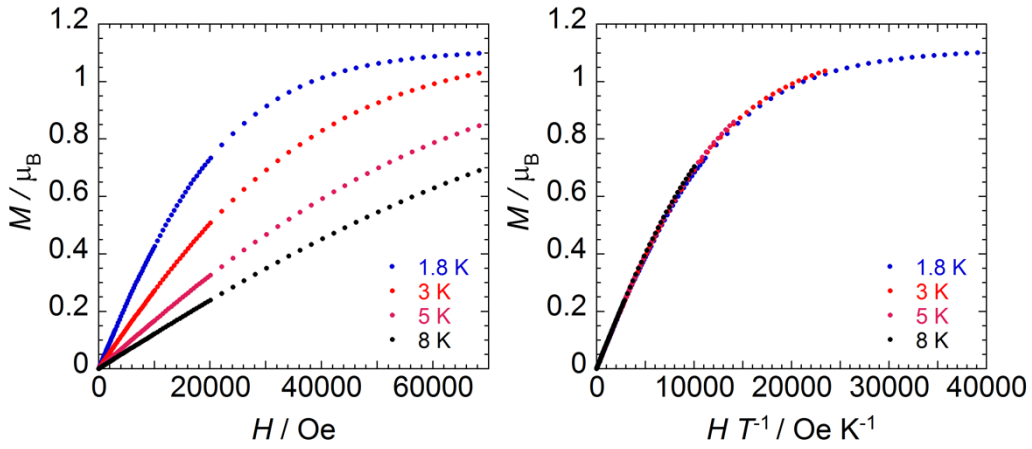

Figure 2.15. Field dependence of the magnetization (left) and the reduced magnetization (right) at 1.8, 3, 5 and 7 K for **1**. Experimental data is represented by solid circles.

χT curves of complexes **2** and **3** display similar temperature dependent behaviors over the temperature range of 1.8-300 K, and this is not surprising given the similarities in their molecular structures. At room temperature, χT values of 1.01 cm^3 K mol^{-1} for **2** and 1.05 cm^3 K mol^{-1} for **3** are obtained. The χT profile of **2** and **3** remains relatively linear upon decreasing temperature, until 12 K, where there is a more precipitous drop, reaching a minimum value of 0.73 cm^3 K mol^{-1} and 0.75 at 1.8 K, respectively. This could due to the magnetic anisotropy, thermal depopulation of low lying excited states or weak antiferromagnetic intermolecular interactions.[139-141] These χT products also include a small temperature independent paramagentism (TIP) contribution of 0.0002 cm^{-1} for **2** and there is no TIP for **3**. In addition, at 1.9 K the magnetization saturates at 2.00 μ_B for **2** and 1.86 μ_B for **3** (Figure 2.16 and 2.17), which is in excellent agreement with the expected value for these spin system (2 μ_B), considering the spin-only formula. Furthermore, the non-superposition of the reduced magnetization isotemperature curves may be the result of unquenched angular momentum (Figure 2.16 and 2.17). Alternating current (ac) magnetic susceptibility studies performed on the complexes did not reveal any frequency-dependent, out-of-phase signals, which indicates that the complexes do not act as single-molecule magnets.

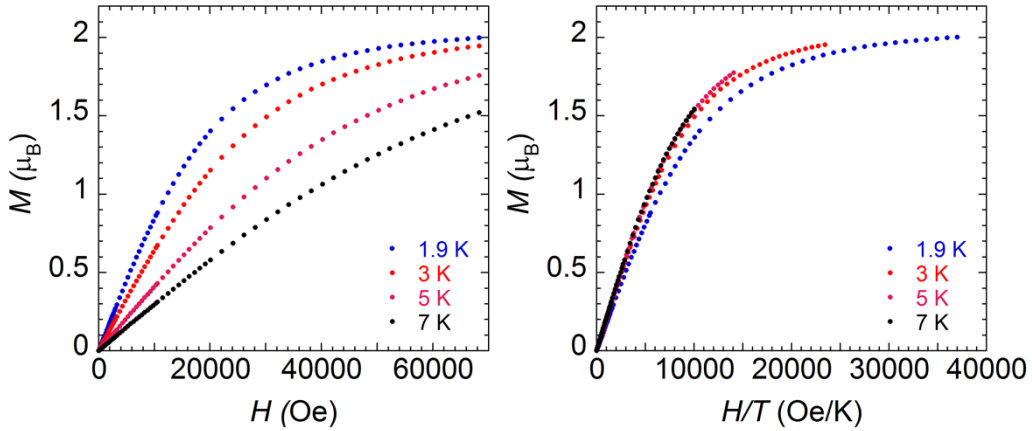

Figure 2.16. Field dependence of the magnetization (left) and the reduced magnetization (right) at 1.8, 3, 5 and 7 K for **2**. Experimental data is represented by solid circles.

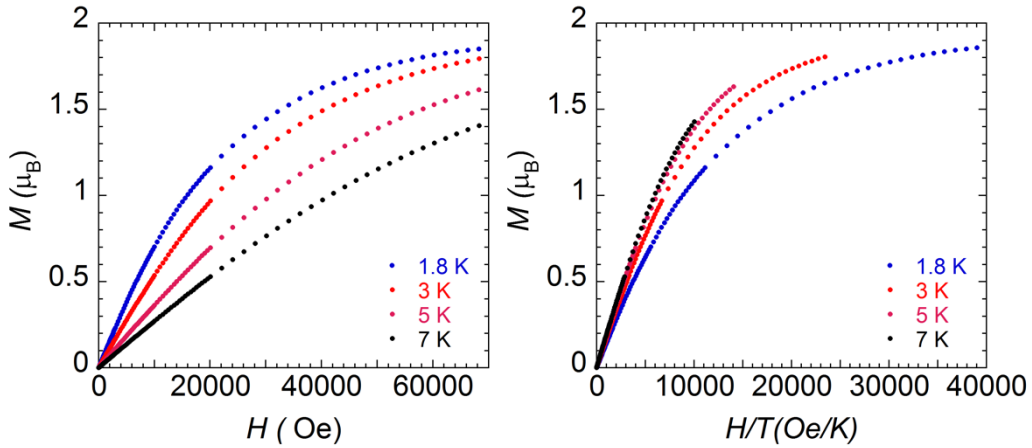

Figure 2.17. Field dependence of the magnetization (left) and the reduced magnetization (right) at 1.8, 3, 5 and 7 K for **3**. Experimental data is represented by solid circles.

2.4 Conclusion and future work

In summary, a series of new complexes **1-3** namely $[Co^{II}(BTZP)_2](ClO_4)_2 \cdot 3MeCN$(**1**), $[[Ni^{II}(BTZP)(MeCN)_3](ClO_4)_2]$ (**2**), $[Ni^{II}Cl_2(BTZP)(MeCN)] \cdot 2MeCN \cdot H_2O$ (**3a**), $[Ni^{II}Cl_2(BTZP)(MeCN)] \cdot MeCN$ (**3b**), $\{[Cd^{II}(BTZP)(NO_3)_2]\}_n$ (**4**) have been successfully prepared, isolated *via* complexation of BTZP with $Co^{II}(ClO_4)_2$, $Ni^{II}(ClO_4)_2$, $NiCl_2$ and $Cd(NO_3)_2$, and characterised structurally, together with detailed probing of their solution phase electrochemical and solid-state magnetic behaviour. Even though complexes **1-3** are all discrete molecules, their crystal structures are quite different. Particularly, complex **1** crystallized in a

classic $[CoN_6]^{2+}$ formula with coordination through the tridentate 'terpy-like' pocket and there is a Jahn-Taller compression effect observed in the SCXRD data. Complex **2** and **3** have some relatively similar perfect octahedral geometries with one tridentate coordinated BTZP ligand and three weak monodentate coordinated weak field ligand. However, complex **4** is composed of a 7-coordinated polynuclear cadmium complex which is bridged by two nitride groups and repeated by $[Cd^{II}(BTZP)(NO_3)_2]$ units. Overall, there is two BTZP ligand coordinated in **1** and only one BTZP ligand coordinated in **2-4**.

Since complexes **1-3** are discrete molecules, the diffused reflectance spectra are almost identical, which shows the expected MLCT ranging from 600 nm to 700 nm. However, the complex **4** has another absorption at 590 nm which also presented in the free ligand and furthermore, all of complexes contains a shoulder at 927 nm, exclusively in the NIR region. Even though complexes **1-3** are all discrete molecules, the extra coordinated BTZP ligands might lead to the fact that electrochemical studies for **1** is quite unique, comparing to the rest of the compound. It can be observed that **1** has two metal-centered redox reactions with 0.570 V and -0.169 V *vs* Fc/Fc^+ and four ligand-based redox couples, falling in the range of -0.202 V< $E_{1/2}$< -1.361 V. As for complex **2-4**, most of the metal-centered redox processes were reversible or partially reversible, which falls in the range of -0.146 V < $E_{1/2}$ < 0.521 V *vs* Fc/Fc^+. Apart from these redox events, all of the complexes showed two ligand-centered reduction processes which were either partially reversible or irreversible, in a range from -0.577 V to -1.961 V. Consequently, based on the cyclic volumetric data observed above, complex **1** is the ideal candidate to explore the radical state of BTZP, because its classic "terpy-like" structure can stabilize the BTZP radical state. In terms of the magnetic properties, complex **1** exhibit paramagnetic behaviour with S=1/2, yielding 0.55 cm^3 K mol^{-1} for **1**. Complex **2** and **3** has similar χT profile of 1.01 cm^3 K mol^{-1} for **2** and 1.05 cm^3 K mol^{-1} for **3** due to the same electron configuration, leading to S=1. Complex **4** is diamagnetic due to the all electrons in the metal center are paired up.

On the basis of studies described above, we have successfully prepared a series of first and second row transition metal with the complexation of BTZP and investigated their optical, electrochemical and magnetic properties. According to the electrochemical data, the next step will be focused on synthesizing the classic $[CoN_6]^{2+}$ formula with coordination through the tridentate 'terpy-like' pocket, for only complex **1** showed reversible redox active properties. Investigations

to further explore and understand the redox chemistry by isolating the radical state of BTZP, and new magnetic materials in terms of the coordination chemistry with different metal ions or other terpy analogues are currently underway.

3 Reversible redox, spin crossover, and superexchange coupling in 3-d transition metal complexes of bis-azinyl analogues of 2,2':6',2"-terpyridine

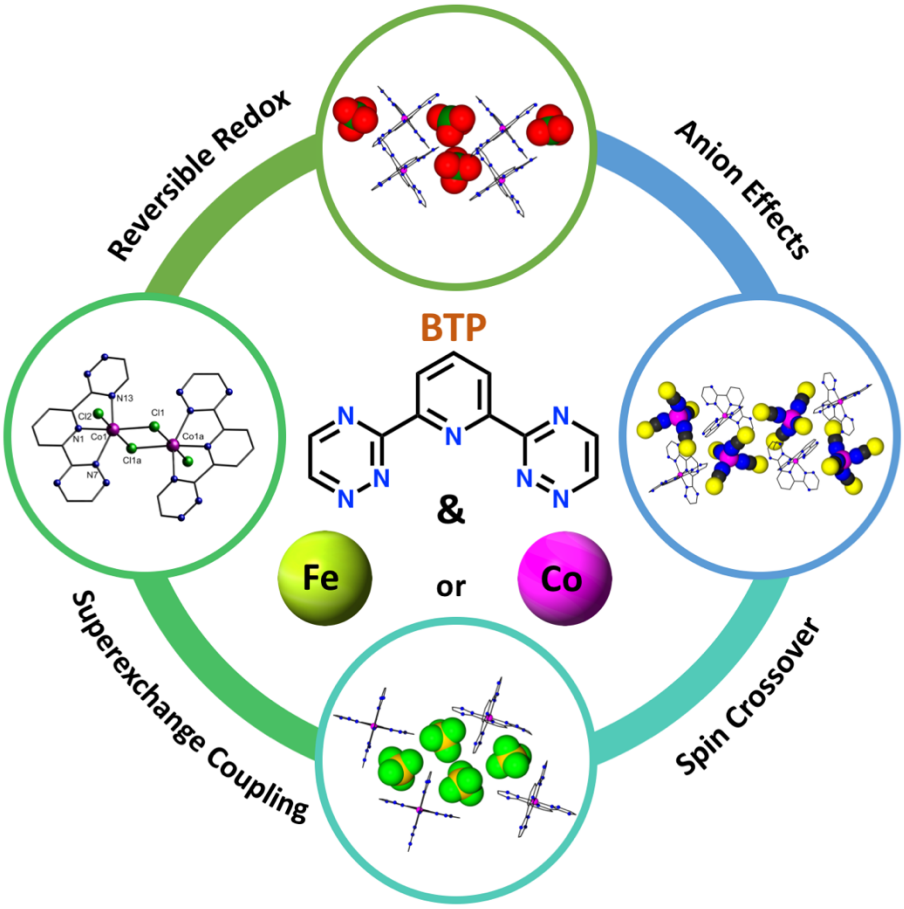

Abstract

A new series of first row of transition metal complexes was synthesized, and the geometry and preliminary magnetic measurements of the complexes were explored. The specific ligand used 2,6-bis-(5,6-dialkyl-1,2,4-triazin-3-yl)-pyridine (BTP) was synthesized. The terpyridine-inspired tridentate ligand, 2,6-bis-(5,6-dialkyl-1,2,4-triazin-3-yl)-pyridine (BTP), was synthesized and utilized to isolate five $[M^{II}(BTP)_2]^{2+}$ (M = Fe and Co) transition metal complexes of various anions (BF_4^-, ClO_4^-, and NCS^-). Notably, when metal-halide precursors are employed, 1:1 M:L products $[Co_2^{II}(\mu\text{-}X)_2(BTP)_2X_2]$ (X = Cl or Br) are obtained, exhibiting μ-halide bridges. All complexes were structurally characterized through single crystal X-ray diffraction and their electrochemical and magnetic properties were investigated. Electrochemical studies reveal that the free BTP ligand

has a single irreversible reduction, however; coordination to a metal center results in stabilization of the reduced BTP ligand and the observation of up to four reductive processes associated with the ligand within the solvent window. The metal-centered redox processes were either reversible or partially reversible, and fall within the range of $0.13 < E_{1/2} < 0.90$ V *vs*. Fc/Fc^{+}. Although there was minimal effect on the redox properties of the metal centers, there is strong dependence on the spin state. SQUID magnetometry elucidated a low spin state for the Fe^{II} complexes at room temperature, revealing a diamagnetic electronic structure. Whereas, the cobalt monometallic complexes, $[Co^{II}(BTP)_2]^{2+}$, showed gradual spin crossover properties between 1.8–370 K, displaying a minor dependence on the spin crossover behavior based on the respective anion. Additionally, ferromagnetic exchange interactions of J = +2.57 and +2.98 cm^{-1} were obtained using the -2J formalism for the dinuclear Co^{II} complexes, $[Co_2^{II}(\mu\text{-}X)_2(BTP)_2X_2]$ for X = Cl and Br respectively.

3.1 Introduction

Chelating ligand design and its coordination chemistry has consistently been of significant research interest, which is due in part to the diversity of potential applications, from catalysis to functional materials.[93, 97-100] To date, one of the most widely studied ligand systems is 2,2';6',2''-terpyridine (terpy) and its related derivatives which contain tridentate chelating environments, thus allowing for coordination to a wide range of metal ions with varied geometries and coordination numbers from 2 to 12. Many of these systems have found application in fluorescence,[76-78] spin-crossover,[71-74] photo systems,[142] organic electronics,[143, 144] gas absorption,[80] light-emitting electrochemical cells,[79] sensors,[75] biomedical applications,[145-147] etc. Complexes of terpy itself can have important functionalities, while terpy derivatives bearing different substituents are also known in the literature. These variants of terpy and their complexes have been further studied in supramolecular chemistry such as metal-containing polymers,[123, 148] molecular and nanochemical devices,[149] dendrimers,[150] and supramolecular arrays.[123] One such modification of terpy to attain these desired properties has been the incorporation of nitrogen rich triazines at the 2 and 6 positions of the central pyridine ring, resulting in 2,6-bis(6-methyl-1,2,4,5-3-yl) pyridine (BTP), a terpy analog with a trident chelating environment (Figure 3.1). The additional inclusion of heteroatoms (N) within the flanking heterocycles increases the π-accepting abilities of terpy, resulting in a stronger field ligand. This type of synthetic tunability is an attractive feature for controlling the

spin-state of a chelated metal ion; a promising approach for the development of new molecular magnetic materials.

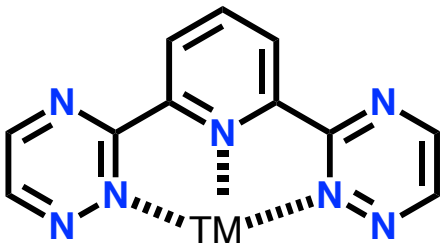

Figure 3.1. The ligand 2,6-bis-(5,6-dialkyl-1,2,4-triazin-3-yl)-pyridine (BTP) and potential coordination mode of BTP ligand, demonstrating the encapsulation of one metal center. In all complexes, the central pyridine ring and two triazine rings are coordinated to metal ions.

With respect to this, complexes of 3-d transition metals namely, Fe^{II} and Co^{II} are known to be ideal candidates for molecular magnetic materials, especially for the purpose of attaining spin crossover behaviour and observing the ligand field influence on the magnetic properties.[71-74] The structural motifs for spin crossover complexes are typically $[M(N)_6]^{2+}$, which are composed of terpy-like or bis-pyrole based ligands.[151] With respect to this, the synthesis and physical characteristics of two $[M(N)_6]^{2+}$ (M = Fe^{II} and Co^{II}) complexes, $[Fe(BTP)_2][BF_4]$ and $[Co(BTP)_2][BF_4]$, were previously investigated with the goal of producing spin crossover spieces.[91] However; the limited stability of such compounds prevented the full assessment of their magnetic properties, precluding the determination of their spin states. Fortunately, larger anions like ClO^{4-} or NCS^{-} have been shown to play an important role in stabilizing metal ions within complexes.[152-154] Consequently, the introduction of halides as counterions may soften the ligand field as they are characteristically weak-field ligands. Collectively, this allows for synthetic tunability of both the stability and spin-states of BTP complexes through counterion effects.

Solid-state structures of BTP complexes have only been previously reported with lanthanide ions or with heavy second/third row transition metals.[90, 96] Thus, for the first time we report the solid-state structures of a family of first row transition metal complexes of BTP. Of the series, five complexes have the general formula $[M^{II}(BTP)_2]^{2+}$ (M = Fe and Co) with coordination through the tridentate ‘‘terpy-like’’ pocket,[116] and two complexes of the $[Co^{II}(\mu\text{-}X)_2(BTP)_2X_2]$ (X = Cl or Br) form were obtained by solvothermal synthesis. We have structurally characterised both

the Fe and Co derivatives of BTP and complete their cyclic voltammetry analysis as well as investigate the spin-states of the complexes through magnetometry. Additionally, the dinuclear-species allow for a unique opportunity to study the superexchange coupling between two high-spin cobalt metal centers through halide bridges in the $[M^{II}(\mu\text{-}X)_2(BTP)_2X_2]$ coordination motif.

3.2 Experimental section

3.2.1 General considerations

All manipulations, unless otherwise stated, were performed under aerobic/ambient conditions. All materials were used as received from TCI, Strem Chemicals and Sigma Aldrich without further purification.

3.2.2 Synthesis of 2,6-dicyanopyridine

2,6-dicyanopyridine was synthesized as previously reported.[84] 2,6-dibromopyridine (5 g, 21 mmol), copper(I) cyanide (3.0 g, 33 mmol) and sodium cyanide (2.2 g, 45 mmol) were mixed in 20 mL of dry dimethylformamide (DMF). The solution was heated to 140 °C in an oil bath and refluxed under N_2(g) for 12 hours. Upon cooling to room temperature, 20 mL of concentrated sodium cyanide solution in water was then used to dissolve the excess copper (I) complex. A brown solid was precipitated upon addition of 100 mL of water. The resulting mixture was filtered by suction filtration with silica and washed with chloroform. The filtrate was collected and extracted with chloroform (3 x 100 mL). The combined organic extracts were collected and washed with brine (10 x 100 mL). The organic extracts were then evaporated to dryness, yielding a white crystalline solid which was collected and dried *in vacuo.* Yield: 2.35g, 87%. ^{1}H NMR (25 °C, 300 MHz, $CDCl_3$): δ 8.04(t, *J* = 8.0HZ, Ar-p, 1H), 7.90(d, *J* = 8.0HZ, Ar-m, 2H).

3.2.3 Synthesis of pyridine-2,6-bis(carboximidhydrazide)

The compound was synthesized as previously reported.[155] 2.35g (18.33 mmol) of 2,6-dicyanopyridine was dissolved in 160 mL of ethanol. To this beige solution, hydrazine monohydrate (12 mL, 366.60 mmol) was added and the resulting solution was stirred for 24 h. The resulting white precipitate was collected through vacuum filtration, washed with cold ethanol, and air dried resulting in a yield of 58% (2.05 g). ^{1}H NMR (25 °C, 300 MHz, DMSO-d6) δ 7.82 (d, J = 7.8 Hz, 2H), 7.68 – 7.59 (m, 1H), 6.04 (s, 4H), 4.96 (s, 4H).

3.2.4 Synthesis of 2,6-bis-(5,6-dialkyl-1,2,4-triazin-3-yl)-pyridine (BTP)

The compound was synthesized as previously reported.[93] Pyridine-2,6-bis(carboximidhydrazide) (2.05 g, 10.61 mmol) and 2,3-dihydroxy-1,4-dioxane (2.23 g, 10.61 mmol) were combined in 60 mL of methanol and stirred for 6 h at room temperature, followed by refluxing for 16 h. The resulting yellow solid was collected and washed with acetone. The filtrate was collected and following slow evaporation for one week, yellow crystals were isolated and combined with the previous product and dried *in vacuo*. The ligand was used without any further purification for the complexation studies. Yield: 1.5g, 60%. Elemental analysis; Calculated: C, 54.95; H, 2.93; N, 40.78. Found: C, 55.06; H, 2.99; N, 40.41. 1H NMR (25 °C, 300 MHZ, DMSO-d6) δ 8.30 (t, J = 7.94 Hz, 1 H) 8.63 (d, J = 7.84 Hz, 2 H) 9.05 (d, J = 2.35 Hz, 2 H) 9.52 (d, J = 2.35 Hz, 2 H). 13C NMR (25 °C, 300 MHz, DMSO-d6) 163.1, 153.6, 150.8, 150.1, 139.3, 126.0 ppm. Selected IR (ATR, cm-1): 3072 (w), 3020 (w), 1583 (w), 1521 (m), 1439 (w), 1411 (m), 1382 (m), 1361 (m), 1340 (m), 1294 (w), 1258 (m), 1180 (w), 1167 (w), 1159 (w), 1124 (m), 1101 (w), 1086 (m), 1053 (s), 989 (s), 977 (s), 878 (m), 833 (m), 783 (s), 761 (w), 733 (m), 687 (m), 647 (m), 633 (s).

3.2.5 Synthesis of $[Fe^{II}(BTP)_2]$ $(BF_4)_2 \cdot 4MeCN \cdot Et_2O$ (5a).

BTP (0.1 mmol, 23.7mg) and $Fe(BF_4)_2 \cdot 6H_2O$ (0.1 mmol, 33.8mg) were combined in 20 mL of MeCN. The resulting black solution was stirred at room temperature until all the starting material was dissolved. This solution was gravity filtered, and the filtrate was collected and evaporated slowly for ~2 days to concentrate the solution. Following a second filtration, the resulting mother liquor was placed in a bath of diethyl ether. After one week, black needle-shaped crystals were collected with 80% yield. Recrystallization in MeOH and re-precipitation in ether was performed before any further characterization. Elemental analysis; Calculated: C, 34.86; H, 2.66; N, 25.87; Found: C, 35.27; H, 2.46; N, 25.75. 1H NMR (25 ^{o}C, 300 MHz, acetone-d6) δ 9.36 (d, J = 7.43 Hz, 2H), 9.14 (m, 4H), 9.06 (m, 1H). Selected IR (ATR, cm^{-1}): 3616 (w), 3544 (w), 3068 (w), 2168 (w), 1980 (w), 1618 (w), 1566 (w), 1539 (m), 1492 (w), 1431 (w), 1406 (m), 1348 (m), 1309 (w), 1285 (m), 1226 (w), 1151 (w), 1109 (w), 1050 (br), 875 (m), 833 (m), 782 (m), 748 (w), 679 (w).

3.2.6 Synthesis of $[Fe^{II}(BTP)_2]$ $(ClO_4)_2 \cdot 2MeOH$ (5b).

Complex **5b** was synthesized in an analogous manner to complex **5a**, where BTP (0.1 mmol, 23.7 mg) and $Fe(ClO_4)_2 \cdot 6H_2O$ (0.1 mmol, 33.8 mg) were combined in 20 mL of MeCN and recrystallizing from the MeOH. Black block-shaped crystals suitable for single-crystal X-ray crystallography were isolated after ~5 days. Yield = 80%. Elemental analysis; Calculated: C, 33.91; H, 2.07; N, 25.17; Found: C, 34.27; H, 2.16; N, 25. ^{1}H NMR (25 °C, 400 MHz, acetone-d_6) δ 9.28 (d, J = 7.8 Hz, 2H), 9.07 (d, J = 2 Hz, 2H), 9.04 (d, J = 2.5 Hz, 2H), 9.02 (t, J = 8 Hz, 1H). Selected IR (ATR, cm^{-1}): 3599 (w), 3080 (w), 1972 (w), 1631 (w), 1567 (w), 1542 (m), 1491 (w), 1433 (w), 1402 (m), 1341 (m), 1309 (w), 1288 (w), 1154 (w), 1082 (s), 1044 (s), 871 (w), 831 (m), 783 (m), 748 (w), 679 (w), 619 (s), 562 (w).

3.2.7 Synthesis of $[Co^{II}(BTP)_2]$ $(BF_4)_2 \cdot 3MeCN$ (6a).

Complex **6a** was synthesized in an analogous manner to complex **5a** and **5b**, where BTP (0.1 mmol, 23.7 mg) and $Co(BF_4)_2 \cdot 6H_2O$ (0.1 mmol, 34.6mg) were combined in 20 mL of MeCN. Black block-shaped crystals suitable for single-crystal X-ray crystallography were isolated after ~2 days. Yield = 80%. Elemental analysis; Calculated: C, 34.18; H, 2.09; N, 24.72;25.37 Found: C, 34.27; H, 2.16; N, 25.44. Selected IR (ATR, cm^{-1}): 3630 (w), 3090 (w), 2249 (w), 1609 (w), 1544 (m), 1404 (m), 1353 (w), 1315 (w), 1285 (m), 1030 (s), 877 (w), 833 (w), 748 (w), 695 (w).

3.2.8 Synthesis of $[Co^{II}(BTP)_2]$ $(ClO_4)_2 \cdot 4MeCN$ (6b).

Complex **6b** was synthesized in an analogous manner to complex **5a** and **5b**, where BTP (0.1 mmol, 23.7 mg) and $Co(ClO_4)_2 \cdot 6H_2O$ (0.1 mmol, 34.6mg) were combined in 20 mL of MeCN. Black block-shaped crystals suitable for single-crystal X-ray crystallography were isolated after ~2 days. Yield = 80%. Elemental analysis; Calculated: C, 35.15; H, 2.50; N, 25.23; Found: C, 34.91; H, 2.25; N, 25.59. Selected IR (ATR, cm^{-1}): 3079 (w), 2323 (w), 2162 (w), 2050 (w), 1980 (w), 1682 (w), 1609 (w), 1581 (m), 1552 (w), 1510 (w), 1494 (s), 1472 (m), 1439 (w), 1394 (s), 1359 (m), 1322 (m), 1279 (s), 1172 (m), 1087 (s), 1034 (m), 995 (m), 960 (m), 920 (m), 835 (m), 788 (m), 748 (m), 680 (w), 623 (s), 599 (m), 573 (s), 564 (s), 555 (s), 535 (s), 534 (m), 526 (m).

3.2.9 Synthesis of $[Co^{II}(BTP)_2]$ $[Co^{II}(NCS)_4]$ (6c).

BTP (0.05 mmol, 11.35 mg), $Co(NCS)_2$ (0.1 mmol, 17.51 mg) and MeCN (10 ml) were added to a 20 mL sealed glass scintillation vial. The resulting mixture was sonicated for 10 min and heated gradually to 90 ^oC over 4 h, followed by heating at 90 ^oC for 24 h. The system was gradually cooled to room temperature over a period of 12 h, resulting in small black block-like crystals. These crystals were collected by suction filtration and air dried, with a 30% yield based on $Co(NCS)_2$. Elemental analysis; Calculated: C, 37.50; H, 2.66; N, 30.28; S, 15.40; Found: C, 36.98; H, 1.63; N, 30.03; S, 15.35. Selected IR (ATR, cm^{-1}): 3073 (w), 2993 (w), 2042 (s), 1601 (w), 1569 (w), 1537 (s), 1525 (m), 1455 (w), 1436 (w), 1404 (s), 1349 (s), 1314 (m), 1283 (m), 1204 (w), 1145 (w), 1110 (w), 1078 (w), 1060 (m), 1050 (m), 1037 (w), 1023 (w), 977 (w), 917 (w), 874 (m), 849 (w), 828 (m), 775 (s), 743 (w), 736 (w), 700 (m), 639 (w).

3.2.10 Synthesis of $[Co^{II}_2(BTP)_2Cl_4]$ (7a).

Complex **7a** was synthesized in an analogous manner to complex **6c**, where BTP (0.05 mmol, 11.35 mg), $CoCl_2$ (0.05 mmol, 6.49 mg) and MeCN (10 mL) were combined in a 20 mL sealed glass scintillation vial. Black block-like crystals suitable for X-ray diffraction were isolated, with a 35% yield based on $CoCl_2$. Elemental analysis; Calculated: C, 33.78; H, 1.80; N, 25.07; Found: C, 33.54; H, 1.68; N, 25.03. Selected IR (ATR, cm^{-1}): 3195 (br), 2172 (w), 1631 (s), 1538 (s), 1448 (w), 1397 (m), 1353 (m), 1294 (m), 1216 (w), 1160 (w), 1090 (w), 1057 (w), 1021 (m), 931 (w), 874 (w), 830 (m), 798 (w), 785 (w), 740 (w), 692 (w), 667 (w), 641 (w).

3.2.11 Synthesis of $[Co^{II}_2(BTP)_2Br_4] \cdot$ MeCN (7b).

Complex **7b** was synthesized in an analogous manner to complex **6c**, where BTP (0.05 mmol, 11.35 mg), $CoBr_2$ (0.05 mmol, 10.94 mg) and MeCN (10 mL) were combined in a 20 mL sealed glass scintillation vial. Black block-like crystals suitable for X-ray diffraction were isolated with a 25% yield based on $CoBr_2$. Elemental analysis; Calculated: C, 24.98; H, 1.52; N, 18.54; Found: C, 24.94; H, 1.57; N, 18.61. Selected IR (ATR, cm-1): 3321 (w), 2922 (s), 2844 (m), 2160 (w), 1977 (w), 1625 (m), 1456 (m), 1374 (w), 1235 (m), 1177 (w), 1112 (w), 1077 (m), 1039 (m), 959 (m), 907 (m), 831 (m), 780 (m), 736 (w).

3.2.12 Physical measurements

Infrared spectra were recorded with a Thermo Scientific Nicolet 6700 FTIR spectrometer equipped with an ATR in the 500–4000 cm^{-1} range. Diffuse reflectance spectra were measured with a Varian Cary-100 spectrophotometer using polytetrafluoroethylene (PTFE) as a reference. Kubelka-Munk spectra were normalized to allow for meaningful comparisons. Powder X-ray diffraction (PXRD) for bulk samples were carried out using a Rigaku Ultima IV X-ray powder diffractometer. The parallel beam mode was employed to collect the data (λ = 1.541836 Å). NMR analyses were conducted using a Bruker Avance 400 MHz spectrometer equipped with an automatic sample charger and a 5 mm auto-tuning broadband probe with Z gradient. Thermogravimetric analysis data were recorded using a Q5000 IR TGA instrument at a heating rate of 10 ^{o}C/min between room temperature and 1000 ^{o}C, under a constant flow of nitrogen.

3.2.13 Single crystal X-ray diffraction studies

Single crystals of BTP and complexes **5-7** suitable for X-ray diffraction measurements were mounted on thin glass fibersusing paraffin oil. Intensity data collection and unit cell measurement were collected on a MAR345 image plate using Mo Kα radiation (λ = 0.71073 Å) APEX II CCD detector focused by a Xenocs Fox3D mirror at 150 K. Raw data collection and processing was completed with APEX II software package from BRUKER AXS, including a correction for Lorentz and polarization effects. The multi-scan absorption correction (SADABS) was applied. SHELXTL program suite was used to solve and refine crystal structure. All non-hydrogen atoms were refined with anisotropic thermal parameters. Hydrogen atoms were placed on calculated positions in riding mode on their respective atoms. General crystallographic details can be found in Table 3.1. CCDC numbers are as follows: 1563301 (**5a**), 1563302 (**5b**), 1563303 (**6a**), 1563304 (**6b**), 1563305 (**6c**), 1563306 (**7a**), 1563307 (**7b**), 1563309 (BTP).

Table 3.1. Summary of the crystal structure data and refinement for compounds **5-7** and BTP

	5a	**5b**	**6a**	**6b**
Formula	$C_{28}H_{25}B_2F_8FeN_{16}O_{0.5}$	$C_{24}H_{22}Cl_2FeN_{14}O_{10}$	$C_{28}H_{23}B_2CoF_8N_{17}$	$C_{28}H_{23}Cl_2CoN_{17}O_8$
Mr	823.11	793.30	830.18	855.46
Space group	*Cm*	*P*-1	$P2_1/c$	$P2_1/n$
a/ Å	17.7047(12)	10.5726(4)	13.6698(3)	17.787(2)
b/ Å	20.8510 (12)	11.1322(4)	10.3773(2)	10.5289(15)
c/ Å	10.2938(9)	14.3870(5)	25.5544(6)	21.052(3)
α°	90	76.052(3)	90	90
β°	113.674(6)	73.289(2)	104.617(1)	113.439(3)
γ°	90	85.778(3)	90	90
V/ Å^3	3480.3(5)	1573.95(10)	3507.71(13)	3617.3(9)
Z	4	2	4	4
T/K	200	200	200	200
Radiation	Mo-Kα	Mo-Kα	Mo-Kα	Mo-Kα
Dx/ g cm^{-3}	1.571	1.674	1.572	1.571
Mμ/ mm^{-1}	0.527	0.729	0.582	0.696
R[a]$_1$ (reflections)	0.0723	0.0615	0.0709	0.0674
ωR[a]$_2$ (reflections)	0.1823	0.2125	0.2547	0.1670
	6c	**7a**	**7b**	**BTP**
Formula	$C_{22}H_{14}Co_2N_{18}S_4$	$C_{22}H_{14}Cl_4Co_2N_{14}$	$C_{24}H_{17}Br_4Co_2N_{15}$	$C_{11}H_7N_7$
Mr	824.65	734.13	953.02	237.24
Space group	$P2_1/n$	$P2_1/n$	*P*-1	*C*2/*c*
a/ Å	9.6319(2)	8.7504(12)	7.8230(2)	21.6146(17)
b/ Å	11.2915(3)	19.787(3)	9.9711(3)	3.7616(3)
c/ Å	30.0065(7)	7.6239(10)	10.6727(3)	24.864(2)
α°	90	90	68.442(1)	90
β°	90.2269(15)	97.462(2)	78.391(2)	98.754(6)
γ°	90	90	80.920(1)	90
V/ Å^3	3263.44(13)	1308.8(3)	755.22(4)	1996.6(3)
Z	4	2	1	8
T/K	200	200	200	200
Radiation	Mo-Kα	Mo-Kα	Mo-Kα	Mo-Kα
Dx/ g cm^{-3}	1.679	1.863	2.095	1.578
Mμ/ mm^{-1}	1.325	1.722	6.435	0.107
R[a]$_1$ (reflections)	0.0437	0.0353	0.0243	0.0551
ωR[a]$_2$ (reflections)	0.0959	0.0880	0.0499	0.1547

[a] $R = R1 = \sum | |F_o| - |F_c| | / \sum |F_o|$; $wR2 = \{[\sum w(F_o^2 - F_c^2)^2] / [\sum w(F_o^2)^2]\}^{1/2}$; $w = 1/[\sigma_2(F_o^2) + (ap)^2 + bp]$, where $p = [\max(F_o^2, 0) + 2F_c^2]/3$; and $Rw = [\sum w(|F_o| - |F_c|)^2 / \sum w|F_o|^2]^{1/2}$, where $w = 1 / \sigma^2(|F_o|)$.

3.2.14 X-ray powder diffraction (XRPD)

The XRPD pattern for selected complexes were performed using a RIGAKU Ultima IV diffractometer, equipped with a Cu-Kα radiation source (λ = 1.541836 Å), scintillation counter and a graphite monochromator. Scanning of the 2θ range was performed from 5-50°. Initial

molecular models were constructed in the Mercury 3.9 program. Compared with calculated patterns from single crystal X-ray data, XRPD pattern was consistent in 2θ values with slight discrepancies in some intensities of peaks attributed to preferred orientation and some broad amorphous character present. Complex **5** and **6** are amorphous. However, the structure of the sample was confirmed by comparison between the collected pattern and the simulated pattern from the single crystal XRD data of complex **7** (Figure 3.2 and 3.3).

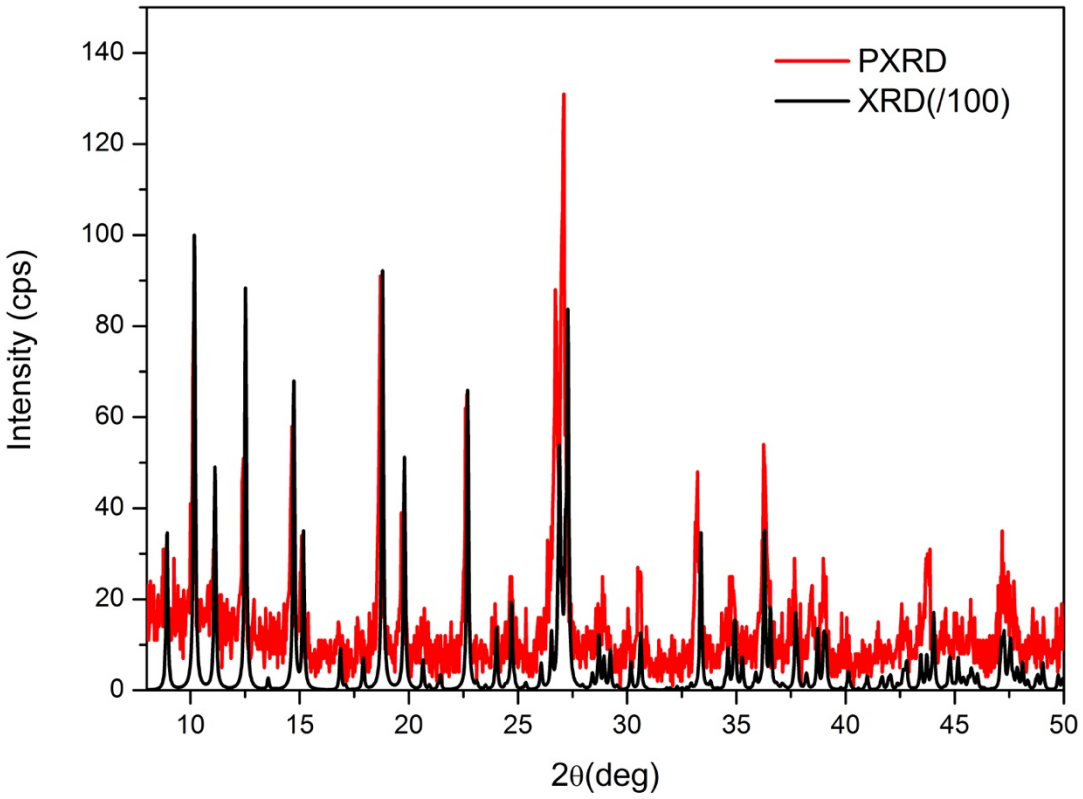

Figure 3.2 X-ray powder diffraction of $[Co^{II}_2(\mu\text{-}Cl)_2(BTP)_2Cl_2]$, **7a** (red) in the 5-50° 2θ region, as compared with the theoretical pattern generated from single crystal X-ray data (black).

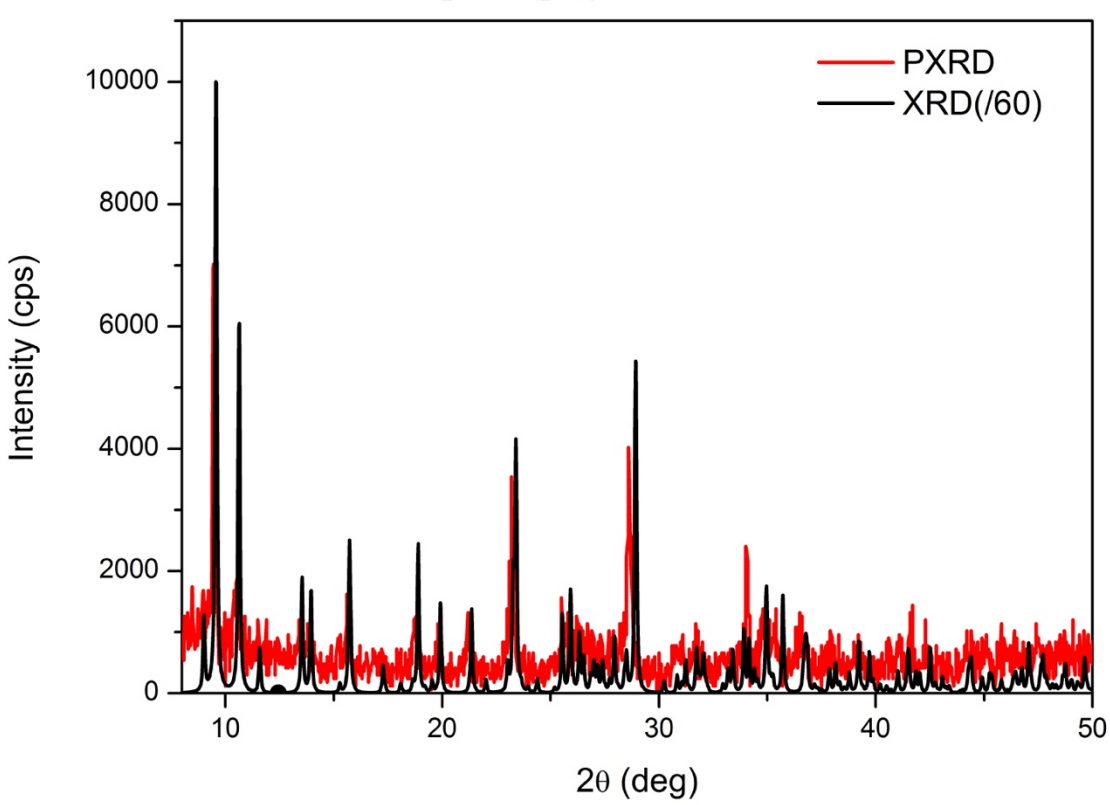

Figure 3.3 X-ray powder diffraction of $[Co^{II}_2(\mu\text{-}Cl)_2(BTP)_2Br_2]$, **7b** (red) in the 5-50° 2θ region, as compared with the theoretical pattern generated from single crystal X-ray data (black).

3.3 Results and discussion

3.3.1 Synthesis and structural analysis of BTP ligand

While the synthesis of BTP has been previously reported, we believe we have accessed a more efficient synthetic route (Scheme 1.1). This may facilitate greater efforts towards the development of the rich coordination and redox chemistries of BTP. BTP was synthesized in three steps from 2,6-dibromopyridine using modified synthetic procedures for the construction of the 1,2,4-triazine rings. [84] The first step for the generation of this bis-triazine ligand is the same with BTZP synthesis, from the replacement reaction between bromide groups and cyanide groups of pyridine in DMF.[155] Under the conditions with lower temperature and shorter reaction time, we are able to obtain the yield to 87 %. The other steps included the addition of hydrazine to 2,6-dicyanopyridine, which can further couple with 2,3-dihydroxy-1,4-dioxane. The published synthesis of BTP involves the addition of glyoxal trimer with 2,6-bis(carboximidhydrazide).[90] However, this method was found to possess a low yield. Consequently, with the addition of small

excess of 2,3-dihydroxy-1,4-dioxane in methanol, both of the triazine rings can be closed by the [4+2] cycloaddition reaction to achieve the BTP ligand. [92] The ligand was used without any further purification for the complexation studies.

Scheme 3.1. Synthetic route for BTP ligand.

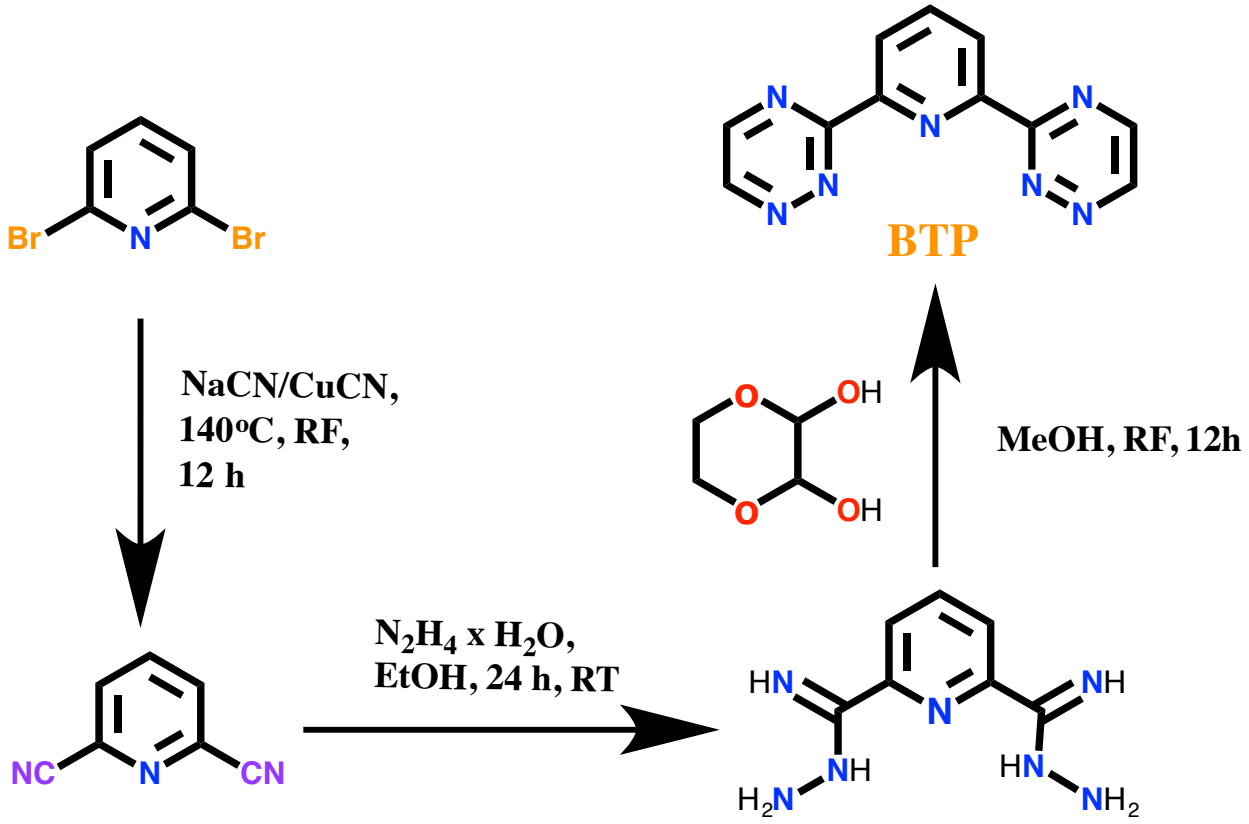

In order to have a better understanding of the BTP molecular structure as well as to gain insight into the effects of metal coordination on the structure, SCXRD studies were performed. BTP crystalizes in the monoclinic C_2/c space group; the asymmetric unit is shown in Figure 3.4. The structure consists of three aromatic rings, a central pyridine ring with two flanking 1,2,4-triazine rings. The three rings appear to occupy the same plane in space, however, the flanking 1,2,4-triazine rings twist slightly out of the plane with torsion angles of 5.80 and 6.70°, most likely a result of the hydrogen bond network within the lattice (*vide infra*). The arrangement of the rings results in the formation of a tridentate and potentially chelating pocket for metal coordination which is akin to that found in terpy. The molecules in the crystal are held together *via* C-H···N hydrogen bonds, which result in two BTP molecules within the same plane to form a dimeric-like

structure (see Figure 3.4). There is a slight elevation of 0.363 Å between the two molecules which take part in the extensive hydrogen bonding within the dimeric-like unit. Together these interactions and the difference in elevation are believed to be the origin of the torsion angles of the 1,2,4-triazine with respect to the central pyridine. Beyond hydrogen bonding, weak π···π interactions between dimers within the same column are observed with short contacts between C15-C16 (3.359(4) Å) and C16-N17 (3.249(3) Å), which are only marginally smaller than the sum of the Van der Waals radii of 3.4, and 3.25 Å for C-C and C-N interactions respectively.[156] The columns of dimers form along the b-axis, where each column of dimers is related to one another by a rotation of ~156^{o} out of the plane of the molecule. Again, C-H···N hydrogen bonds are responsible for linking the ribbon-like layers, such that the closet distance between n atoms in the molecules above and below each other is 3.762(3) Å.

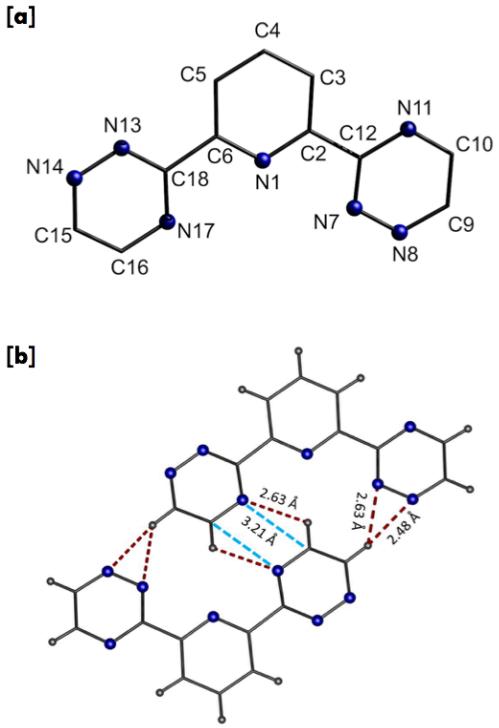

Figure 3.4. [a] Molecular structure of 2,6-bis-(5,6-dialkyl-1,2,4-triazin-3-yl)-pyridines (BTP). Colour code: blue (N) and black (C). All of hydrogen atoms are invisible for clarity. **[b]** Two BTP molecules within the same plane to form a dimeric-like structure which exhibits centro-symmetry.

Colour code: blue (N), black (C) and grey (H). Red dash represents C-H···N hydrogen bonds and blue dash represents for the short contacts between C···N.

3.3.2 Synthesis and structural analysis for complex 5-7

Given the structural similarities of BTP with terpy, the coordination chemistry of BTP was investigated with 3d transition metals. A series of homoleptic and heteroleptic complexes of BTP were isolated. With respect to homoleptic compounds, two isostructural complexes of Fe^{II} with BF_4^- and ClO_4^- counterions were obtained through the addition of the respective hydrate salt to BTP in a 1:1 mole ratio in acetonitrile. The reactions proceed with an immediate colour change from yellow to dark red at room temperature. Gravity filtration followed by diffusion of the mother liquor with diethyl ether afforded black needle single crystals suitable for X-ray diffraction studies. The X-ray crystallographic studies reveal that complexes $[Fe^{II}(BTP)_2](BF_4)_2 \cdot 4MeCN \cdot Et_2O$ (**5a**) and $[Fe^{II}(BTP)_2](ClO_4)_2 \cdot 2MeOH$ (**5b**) crystallize in the monoclinic space groups *Cm* and triclinic *P*-1, respectively (Figure 3.5). The differences observed in the space groups may be attributed to the subtle changes in the counterion interactions within the lattice (*vide infra*), as **5a** and **5b** have a relatively similar structure. Such that the complexes are characterized by a 6-ccordinate Fe^{II} center, where the primary coordination sphere is completed with six N-atoms from two BTP ligands, and exhibits bite angles in the range 80.53-81.55°, resulting in the formation of a distorted octahedral geometry. The BTP ligands are organized in a meridional fashion with average Fe-N distances of 1.916 and 1.917 Å for **5a** and **5b** respectively. The shortest Fe-N distances are obtained for the central N-atom of the pyridine ring with distances of 1.874(7) and 1.877(7) Å for **5a** and 1.878(4) and 1.868(4) Å for **5b** (Table 3.2). Following bond valence sum (BVS) calculations these Fe-N distances are most consistent with a Fe^{II} oxidation state for the metal center, correlating with the charge balance of the species. What is interesting to note is the changes in the $N_{triazine}$-$N_{triazine}$ bond distances of the flanking 1,2,4-triazine in comparison to the free ligand. There is a slight compression of the $N_{triazine}$-$N_{triazine}$ bond on average from 1.347(3) to 1.328(8) Å, suggesting that metal-ligand back donation is likely playing role, as it is expected to observed bond elongation upon metal coordination. This finding for complex **5a** and **5b** contrasts the slight bond elongation seen in the corresponding Co^{II} analogs (*vide infra*).

Scheme 3.2. Synthesis of complexes **5-7**. M = Fe^{II} or Co^{II} and X = Cl^- or Br^-.

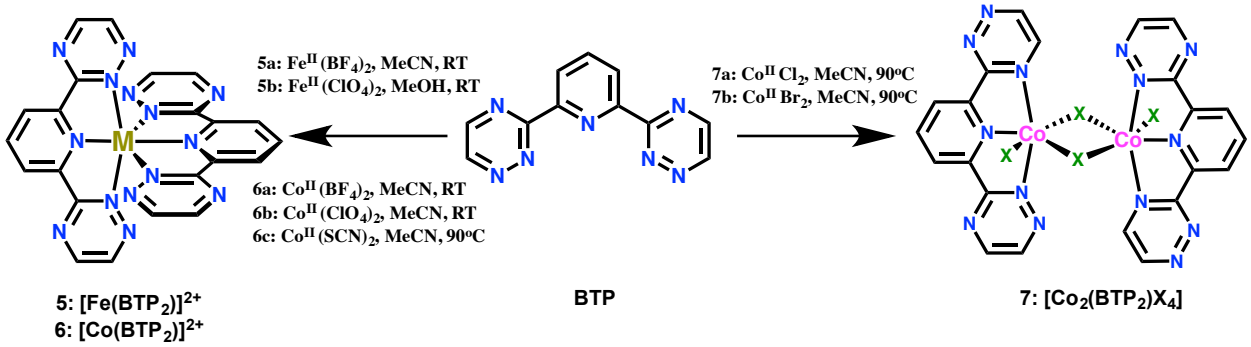

Within the lattice, the counterions largely dictate the packing arrangement, such that both the BF_4^- and ClO_4^- ions of **5a** and **5b** form weak anion-π interactions with the 1,2,4-triazine components of the bound BTP ligands (Figure. 3.8). Such interactions are not surprising as it has been previously observed in similar electron deficient aromatic ligands with tetrazine, triazine, and pyrimidine moieties.[84, 157] Within **5a**, the BF_4^- ions interact with the 1,2,4-triazine ring composed of N19, N20, C21, C22, N23, and C24, such that a F-centroid distance of 2.80 Å is achieved. This distance is well within the Van der Waals separation of 3.17 Å for C-F,[125] suggesting that a dominant electrostatic interaction exists between these moieties. In fact, these interactions with the BF_4^- ions propagate the formation of brick-like layers along the ab-plane, where the BF_4^- ions alternate with the octahedral compound, giving rise to an inter-layer distance of 7.43 Å. The ClO_4^- ions in **5b** form more tightly packed anion-π interactions, resulting in an extension of molecules in a zig-zag fashion along the b-axis. Presumably as a result of the smaller radius of the ClO_4^- ion (2.40 Å) vs. the BF_4^- (2.32 Å),[158] **5b** is able to pack more densely, increasing the density of the materials from 1.571 $g.cm^{-3}$ for **5a** to 1.674 $g.cm^{-3}$. As a result, the distance between the layers decreases to 5.06 Å in comparison to the inter-layer distance in **5a**.

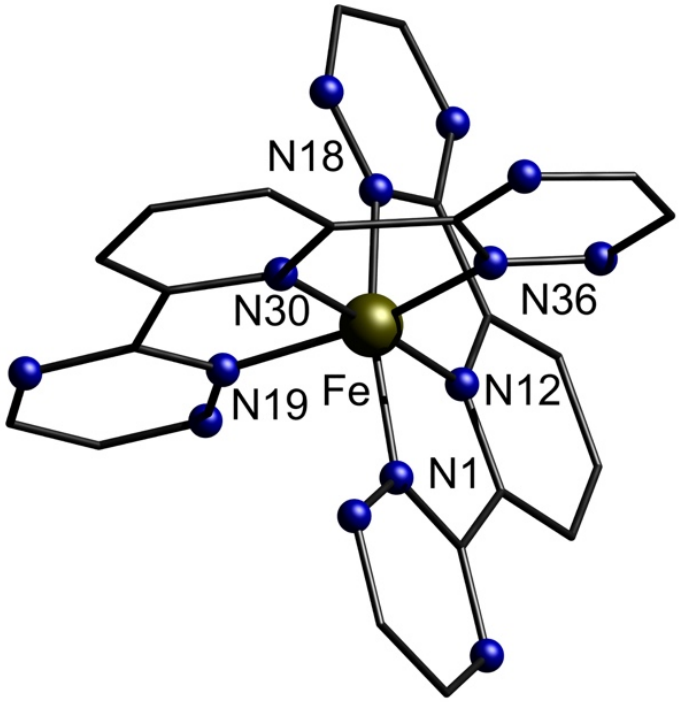

Figure 3.5. Partially labelled molecular structures of complexes $[Fe^{II}(BTP)_2]^{2+}$, **5a**. Colour code: olive green (Fe), blue (N), and black (C). All of hydrogen atoms and solvent molecules are omitted for clarity.

Table 3.2. Selected bond distances (Å) for complexes **5a** and **5b**.

5a		**5b**	
Fe1-N30	1.873(5)	Fe1-N1	1.868(4)
Fe1-N12	1.876(5)	Fe1-N19	1.878(4)
Fe1-N1	1.929(6)	Fe1-N13	1.930(4)
Fe1-N36	1.934(6)	Fe1-N25	1.937(4)
Fe1-N19	1.936(6)	Fe1-N7	1.942(4)
Fe1-N18	1.946(6)	Fe1-N31	1.946(4)

Intrigued by the rich structural insights of BTP with Fe^{II}, its chemistry was also explored with Co^{II} precursors. These efforts have elicited both mononuclear homoleptic complexes with BF_4^-, ClO_4^- and $[Co(NCS)_4]^{2-}$ anions, as well as heteroleptic dimeric complexes, with μ-halides (*vide infra*). Adopting the synthetic procedure for **5a**, single crystals of $[Co^{II}(BTP)_2]$ $(BF_4)_2$ ·3MeCN (**6a**) and $[Co^{II}(BTP)_2]$ $(ClO_4)_2$ ·2MeCN (**6b**) were grown from the diffusion of diethyl ether into the mother liquor of the reaction. SCXRD analysis reveals that both **6a** and **6b** molecule crystallize in the monoclinic $P2_1/n$ space group. The overall crystal structure of **6a** and **6b** closely

resembles the structure of **5a** and **5b** (see Figure 3.6), adopting a 6-coordinate distorted octahedral, coordinated by two BTP ligands in a meridional mode. Notably, the only minor difference between the $[Fe(BTP)_2]^{2+}$ and $[Co(BTP)_2]^{2+}$ is that one of the triazine ring can inverse during the coordination process. In the case of **6a**, one of the rings on 50% of the molecules is inversed indicating its lability and in the **6b** case, this ring is inversed on 100% of the molecules.

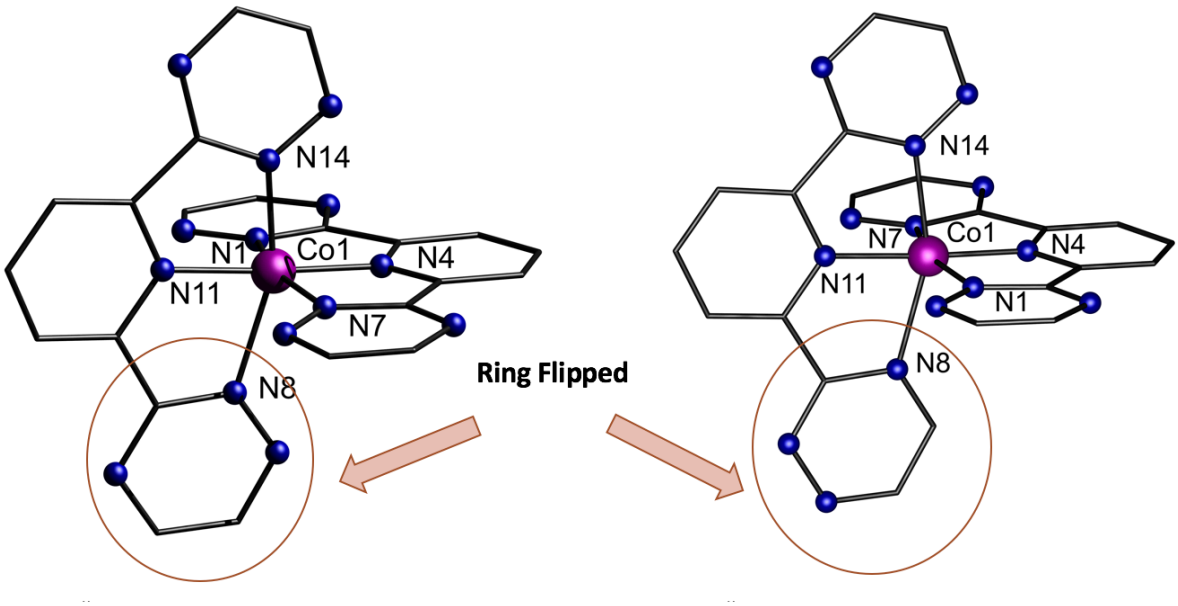

Figure 3.6. Partially labelled molecular structures of complexes $[Co^{II}(BTP)_2]^{2+}$, **6a** (left) and **6b** (right). Colour code: pink (Co), blue (N), and black (C). All hydrogen atoms and solvent molecules are omitted for clarity.

Analysis of the packing arrangements and locations of the counterions in the lattice, reveals that there are a number of close contacts between the 1,2,4-triazine rings and the respective BF_4^- or ClO_4^- ions in the lattice. Specifically, there exists a close contact between N9 of the 1,2,4-triazine and F2 of the BF_4^- ion in **6a**, resulting in a separation of 2.920(2) Å. In the **6b** case, the closest contact is 3.469 (1) Å, between N14 of the triazine ring and O5 of ClO_4^- ion. These interactions are characteristic of anion-π interactions and result in slightly longer average metal-nitrogen bond distances of 1.96 Å (**6a**) and 2.01 Å (**6b**) compared to the Fe^{II} analogues (Table 3.3). This anion-π interaction in both cases is believed to be the result of the elongated Co-N bonds leading to Jahn-Teller axes in both **6a** and **6b**. Within **6b**, the elongation is more pronounced with Co1-N8 and Co1-N14 axial bonds being 2.181(3) Å and 2.123(4) Å respectively. Comparatively,

6a displays a less prominent elongation along the same axis, N8-Co1-N14. Here, the Co1-N14 bond elongation is not immediately obvious, however inspection of the standard errors reveal that the variance in the bond length is 1.91-1.97 Å. Thus, at the upper limit this bond far exceeds the upper limit of the Co1-N1 bond (1.957 Å), thereby providing evidence for a Jahn-Teller elongation along the N8-Co1-N14 axis of compound **6a**. The 1,2,4-triazine cycle which encompasses N1, also participates in similar anion-π interactions, which is likely the cause for the appearance of a longer metal-nitrogen bond. From these observations, it can be concluded that ClO_4^- anions induce a greater Jahn-Teller elongation compared to BF_4^- anions, which is expected to have consequences on the spin states of these materials (*vide infra*). Nevertheless, these BF_4^- or ClO_4^- ions are responsible for propagating a *zig-zag*-like packing arrangements of the complexes in the solid state (Figure 3.8).

Table 3.3. Selected bond distances (Å) for complexes **6a** and **6b.**

6a		**6b**	
Co1-N1	1.953(4)	Co1-N1	1.976(3)
Co1-N4	1.930(5)	Co1-N4	1.865(4)
Co1-N7	1.944(5)	Co1-N7	1.962(3)
Co1-N8	2.143(4)	Co1-N8	2.181(3)
Co1-N11	1.932(4)	Co1-N11	1.926(4)
Co1-N14	1.940(3)	Co1-N14	2.123(4)

For comparison, a complex ion was synthesized with BTP and $Co(NCS)_2$ (2 equiv.) in a solution of MeCN yielded black block-like crystals with octahedron morphology. The as-synthesized compound was characterized and formulated by SCXRD studies as $[Co(BTP)_2]^{2+}$, complex **6c**. Complex **6c** crystallizes in monoclinic space group $P2_1/n$, and consists of one $[Co(BTP)_2]^{2+}$ cation and one $[Co(NCS)_4]^{2-}$ anion (Figure 3.7). The $[Co(BTP)_2]^{2+}$ cation features a central six-coordinate Co^{II} ion, that possesses a distorted octahedral geometry, with two BTP ligands which are approximately perpendicular to one another. Close inspection of the Co-N bond distances, reveals average distances of 2.00 Å (Co1) and 1.95 Å (Co2). Interestingly, the longest observed Co-N distances for Co1 are 2.184(4) Å and 2.118(2) Å for Co1-N12 and Co1-N9 (Table 3.4). These bonds lie on the same axis, providing evidence for a Jahn-Teller elongation and a low spin state (*vide infra*). The shortest Co---Co distance is 7.0495(8) Å, which represents the distance between the octahedral and tetrahedral Co ions. [159] Each unit cell contains **6c** molecules with a similar packing arrangement to complex **6a** and **6b**, with alternating anion-cation pairs. The

molecules form a closely packed networked where the $[Co(NCS)_4]^{2-}$ anions exhibit short S---N contacts with N6 of the flanking triazine rings (3.241(3) Å). Additional short contacts between the H-atoms of the central pyridine ring of BTP and the NCS^- ligands generates a slightly denser packing arrangement than those of **6a** and **6b** (1.679 $g.cm^{-3}$ *vs.* 1.572 $g.cm^{-3}$).

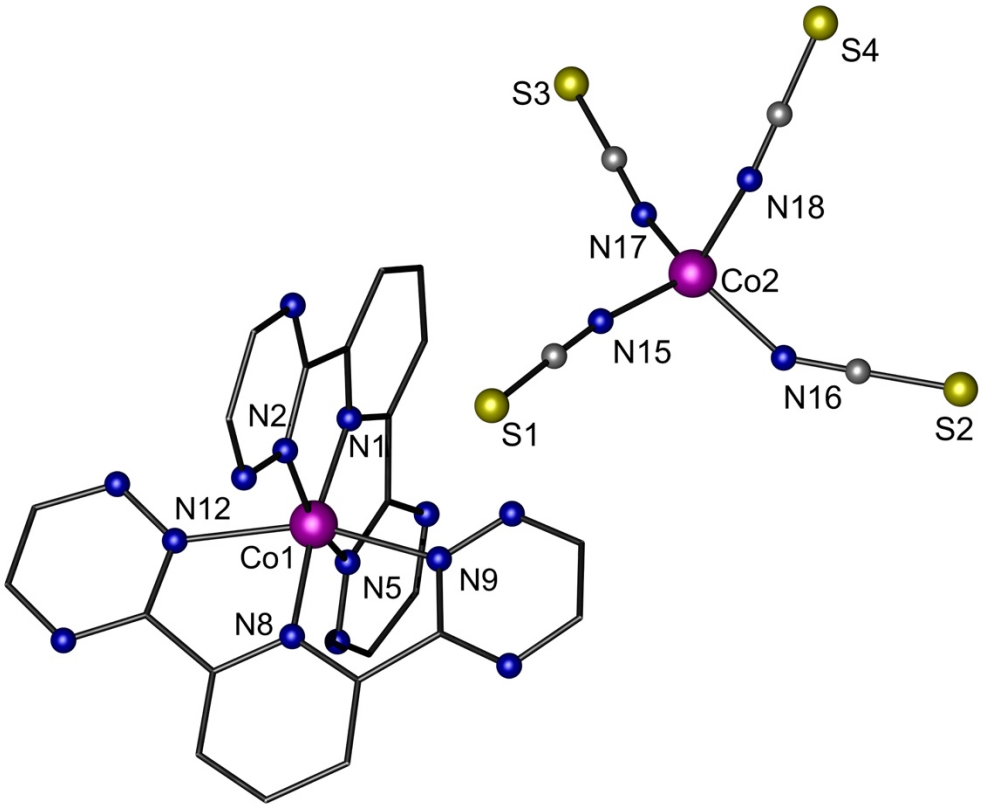

Figure 3.7. Partially labelled molecular structures of complexes $[Co^{II}(BTP)_2][Co^{II}(NCS)_4]$, **6c**. Color code: pink (Co), yellow(S), blue (N), and grey (C). All of hydrogen atoms are omitted for clarity.

Table 3.4. Selected bond distances (Å) for complex **6c**

Co1-N1	1.863(2)	Co1-N12	2.184(2)
Co1-N8	1.930(5)	Co2-N16	1.944(3)
Co1-N2	1.955(2)	Co2-N15	1.953(3)
Co1-N5	1.965(6)	Co2-N17	1.953(3)
Co1-N9	2.119(2)	Co2-N18	1.969(3)

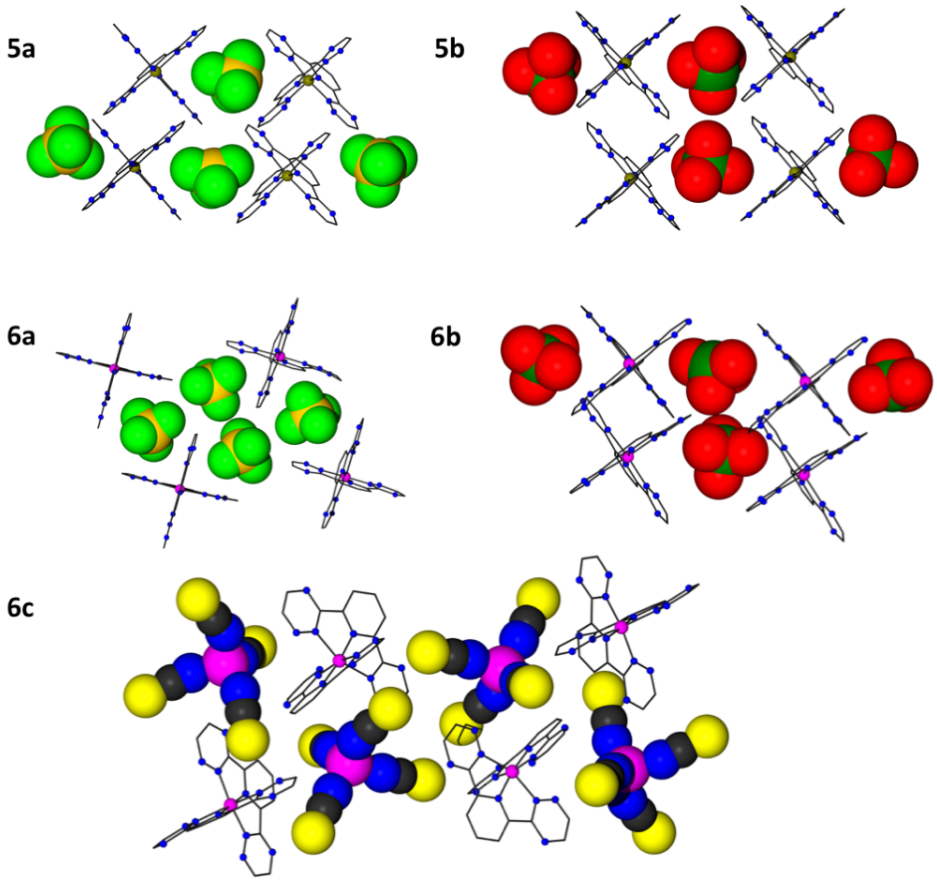

Figure 3.8. Ball and stick, and spacefill molecular structures constructed through *zig-zag* anion-π-system interactions in the structure of **5a**, **5b**, **6a**, **6b** and **6c**. Hydrogen atoms and disorders were omitted for clarity. Colour code: olive green (Fe), red (O), bright green (F), green (Cl), gold (B), pink (Co), yellow (S), blue (N) and black (C).

The reaction of cobalt(II) chloride and BTP was characterized and formulated by X-ray crystallography diffraction studies as complex **7a** (Figure 3.9). According to the crystallographic data, the molecule crystallizes in the monoclinic space group $P2_1/n$, and is composed of a centrosymmetric dinuclear cobalt complex in which two octahedral Co^{II} ions are connected by two chloride bridges (Cl1, Cl1a). The remaining two chloride ions are terminally coordinated with cobalt. This centrosymmetric complex is comprised of two six-coordinate Co^{II} ions. The angle of Co1-Cl1-Co1a is 96.30° and the distance between Co···Co is 3.6719(6) Å, where the shortest distance between two Co^{II} centres connected through two halide bridges in the literature is 2.763Å.[160] The central Co2Cl2 core, appears to be nearly rhombic, with the two Co-Cl1 distances

being 2.5107(6) and 2.4182(7) Å, respectively (Table 3.11). The shortest intermolecular Co···Co distance is 7.624(1) Å.

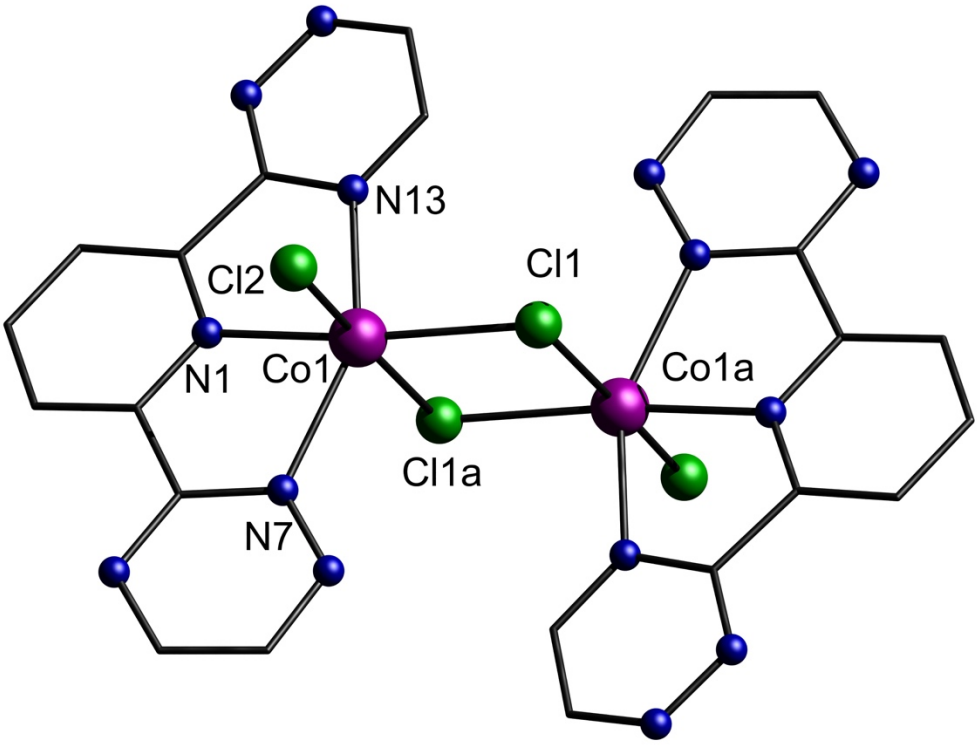

Figure 3.9. Partially labelled molecular structures of complexes $[Co^{II}_2(\mu\text{-}Cl)_2(BTP)_2Cl_2]$ **7a**, which exhibits centro-symmetry. Colour code: pink (Co), blue (N), green (Cl) and black (C). All of hydrogen atoms are invisible for clarity.

The structure of complex **7b** was relatively similar to complex **7a** and the main difference is the exchange of halides from chloride to bromide. Similarly, **7b** crystallizes in the triclinic *P*-1 space group and is composed of a dinuclear cobalt complex which is connected by two bromide bridges (Figure 3.10). The bridging angle of Co1-Br1-Co1a is 93.91° with a Co···Co distance of 3.8152(4) Å. Both the Co-X-Co bond angles and Co···Co distances are similar to those exhibited by complex **7a**. Molecules of complex **7b** form parallel ribbons *via* C-H···N hydrogen bonds. π···π stacking interactions can be seen to further link ribbons layers.

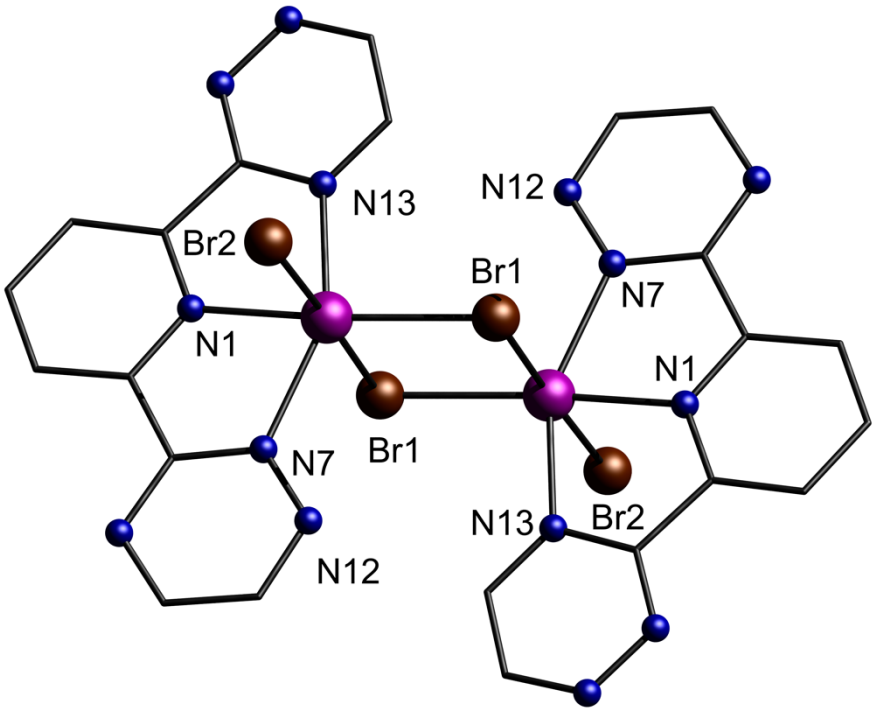

Figure 3.10. Partially labelled molecular structure of complexes $[Co^{II}(\mu\text{-}Br)_2(BTP)_2Br_2]$, **7b**. Colour code: pink (Co), brown (Br), blue (N), and black (C). All hydrogen atoms and solvent molecules are omitted for clarity.

Table 3.5. Selected bond distances (Å) for complex **7a** and **7b**.

7a		**7b**	
Co1-Co1a	3.6719(6)	Co1-Co1a	3.8152(4)
Co1-N13	2.2002(18)	Co1-N13	2.1624(18)
Co1-N1	2.1054(17)	Co1-N1	2.0806(17)
Co1-N7	2.2111(18)	Co1-N7	2.1448(18)
Co1-Cl1-Co1a	96.30 (2)	Co1-Br1-Co1a	93.910(11)

3.3.3 Thermogravimetric analysis

In order to determine the stability of compound **6a** and **6b** in the high temperature during the magnetic measurement studies, TGA experiments were carried out in comparison to that of the **6a** and **6b**. The TGA analysis data of **6a** indicates that there is a small amount of MeCN solvent lose before 100 °C and the compound decomposed at around 300 °C. In the coming **6b** case, we can see that there is a tiny of residue solvent lose before 100 °C compare to **6a**. Additionally, the decomposition temperature is identical to **6a** (Figure 3.11 and 3.12).

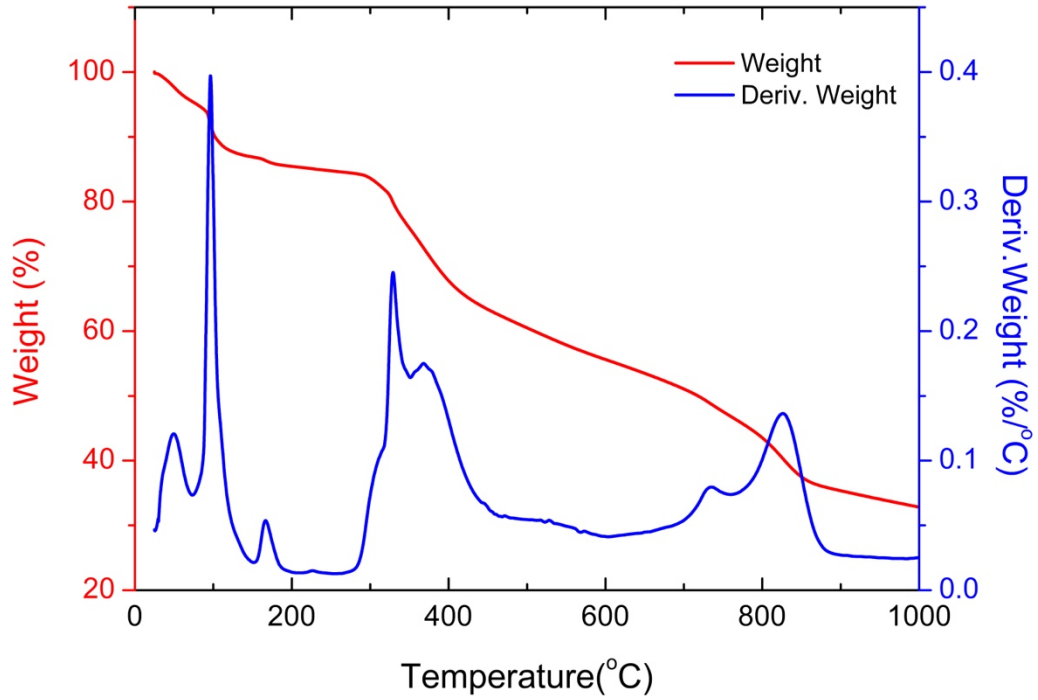

Figure 3.11. TGA analysis of **6a** performed in a dynamic nitrogen atmosphere.

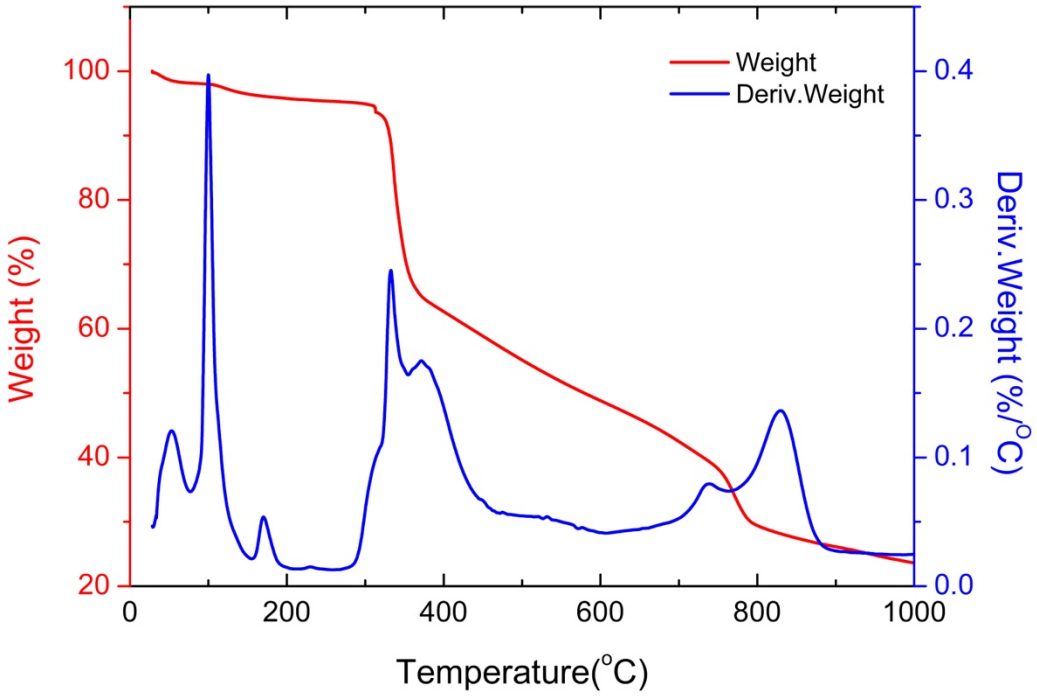

Figure 3.12. TGA analysis of **6b** performed in a dynamic nitrogen atmosphere.

3.3.4 Diffuse reflectance spectroscopy analysis

The solid-state electronic structure of the ligand and its complexes were further investigated using diffuse reflectance spectroscopy at room temperature (Figure 3.13). The free ligand presented a visible absorption at 287 nm, which correlates with the previously reported solution UV-vis absorption measurements completed in 1,4-dioxane by Sauer and coworkers.[92] This band may be attributed to n$\rightarrow \pi^*$ and $\pi \rightarrow \pi^*$ transitions, common to conjugated organics. However, at this absorption range, only **6b** presented four sharp peaks while all the rest of compounds showed a board peak. These ligand based transitions are also observed in the spectra of complexes **1-3**. Intriguingly, complex **2b** displays three peaks in the UV region of the spectrum, which may be attributed to the "ring-flip" described above for this sample (*vide supra*). Thus, it would not be surprising that the different metal-ligand bonding interactions would give rise to three unique energies. The diffuse reflectance spectrum of BTP also contains a shoulder at 927 nm, exclusively in the NIR region. The diffuse reflectance spectra of the octahedral BTP complexes show the expected metal-ligand charge transfer (MLCT) absorptions in the range of 600-700 nm. [76, 126, 127] Notably, the intensity of the MLCT maxima of tetrahedral complexes are significantly higher than other compounds. This can be attributed to the differences in the energy gap of HOMO-LUMO energy levels for tetrahedral and octahedral cobalt complexes. Furthermore, the MLCT λ_{max} values for all BTP complexes are almost identical.

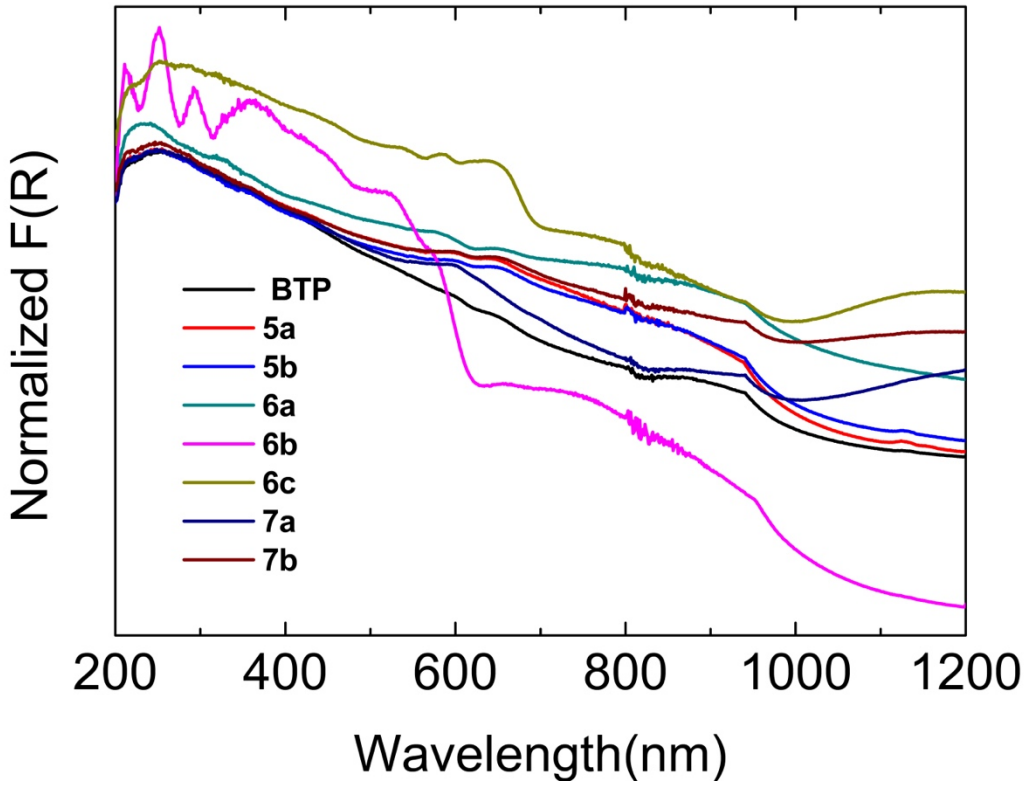

Figure 3.13. Normalized Kubelka-Munk spectra for BTP and complexes **5-7**.

3.3.5 Electrochemical studies of BTP and complexes 5-7

In order to investigate the electrochemical properties of the BTP complexes (**5-7**) and the free BTP ligand, cyclic voltammetry (CV) experiments were conducted in MeCN with 0.1 M Bu_4NBF_6 as supporting electrolyte and Fc/Fc^+ as an internal reference (*vide infra*). BTP (Figure 3.14) exhibits a single irreversible sharply-defined redox process with E_c = - 2.066 V vs. Fc/Fc^+ in MeCN, which is a common value in the redox chemistry of uncoordinated triazines.[161] There are no oxidation peaks observed within the solvent window for BTP. Conversely, for complexes **5-7** the complexity of the CV spectra was unexpected given the simplicity of the free ligand spectra. Most of the metal-centered redox processes were reversible or partially reversible, and fall in a range of $0.13 < E_{1/2} < 0.90$ V vs Fc/Fc^+. In addition to these redox events, all of the complexes showed up to four reductive processes related to the ligand, which were either partially reversible or irreversible (Table 3.6).

Table 3.6. CV data for the complexes in this work (MeCN/0.1 M Bu_4NBF_6, 298 K). Potentials are quoted at a scan rate 0.1 V/s *vs.* an internal Fc/Fc^+ standard

	M^{III}/M^{II} $E_{1/2}$, V	Ligand-based reductions $E_{1/2}$, V
BTP	-	-2.066[b]
5a	1.282	-1.055[b], -1.231[b], -1.533[b], -2.004[b]
5b	-	-1.016[a], -1.276[b], -1.709[a], -2.08[b]
6a	0.139	-0.781[a], -1.517[a], -2.017[a]
6b	0.169	-0.783[a], -1.508[a], -1.978[a]
6c	0.89[c], 0.239	-0.738[b], -1.085[b], -1.517[a], -2.008[a]
7a	-	-
7b	0.329[c]	-0.845[a], -1.481[b], -2.005[a]

[a] Partly chemically reversible, $E_{1/2}$ value quoted. [b] Irreversible process, E_c value quoted. [c] Irreversible process, E_a value quoted.

More specifically, the cyclic voltammetry results of **5a** show a single reversible redox couple with $E_{1/2}$= 1.282 V. Peak to peak potential separation (ΔE) was found to be 0.084 V demonstrating reversibility. In contrast, there are four irreversible processes with potentials of -1.055, -1.231, -1.533 and -2.004 V related to the ligand-based reductions. The Fe^{III}/Fe^{II} redox chemistry of **5a** is very similar to previously reported terpy-like complexes.[162-164] Due to the limitation of the solvent window size, the metal based reduction process of **5b** was not observed. Surprisingly, some of the ligand-based reductions appeared to be partially chemically reversible at -1.016 and -1.709 V, while there are also irreversible processes which appear at -1.276 and -2.08 V, respectively. This finding may suggest that the ClO_4^- anion allows for increased stability of **5b** over **5a**, which was found to be labile in solution in a previous study.[91]

Surprisingly, in the coming cobalt case, it shows the reversible redox properties in **6a** and **6b**. The first reduction of **6a** and **6b** in $[Co(BTP)_2]^{2+}$ are almost identical, with the Co^{III}/Co^{II} redox couple at 0.139 V and 0.169 V, respectively. Peak to peak potential separation (ΔE) was found to be 0.07 V (**6a**) and 0.083 V (**6b**) demonstrating the expected reversibility for the metal-based processes. Although the free ligand showed irreversibility, the ligand-based electrochemistry of $[Co(BTP)_2]^{2+}$ revealed partially reversible redox events for complex **6a** and **6b**. Interestingly, there are only three partially reversible ligand-based reductions compared to the four processes observed in **1a** and **1b**, thus it is anticipated that the fourth process may lie just marginally outside of the solvent window. Nevertheless, the ligand-based peaks for **6a** and **6b** are nearly identical, revealing

potentials of -0.781, -1.517 and -2.017 V for **6a** as well as -0.783, -1.508 and -1.978 V for **6b**, respectively. All the peaks appeared roughly equal and consistent with previous reports of $[CoN_6]^{2+}$ compounds.[130, 131] It is possible that the BTP radical state is stabilized through enhanced metal ligand back bonding with Co compare to Fe.

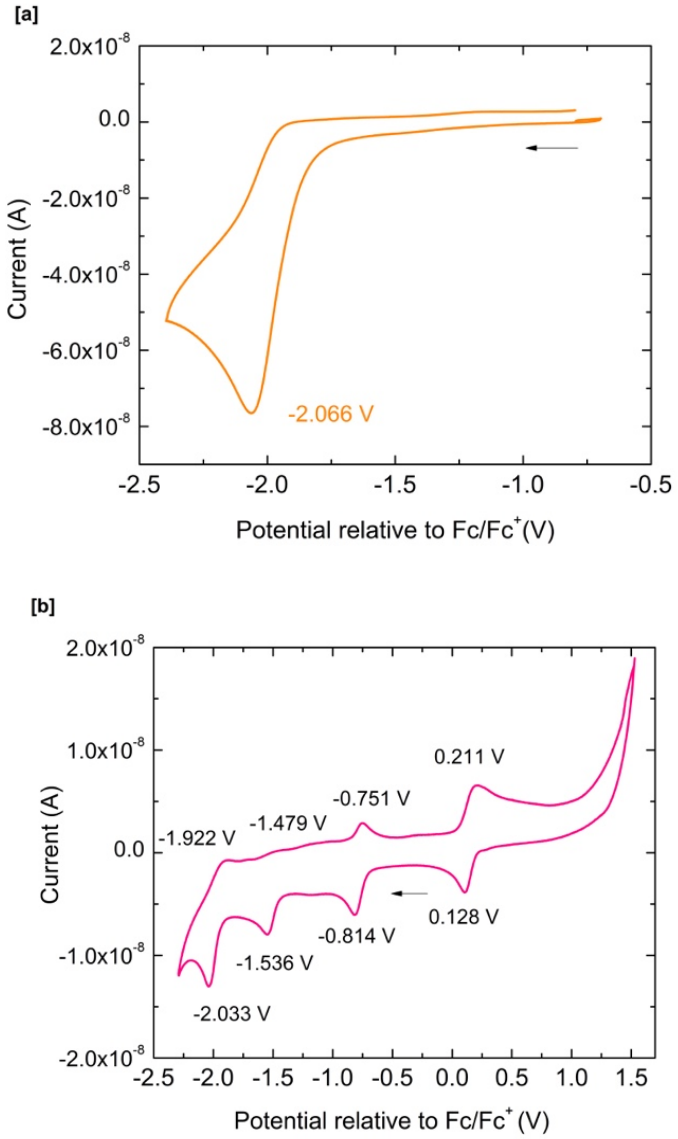

Figure 3.14. CV scan of BTP ([**a**]; top orange line) and **6b** ([**b**]; bottom pink line) in MeCN solution (0.1 M $[Bu_4N][PF_6]$, 100 mV/s). Black arrow indicates the direction of sweep.

Conversely, when it comes to **6c**, the Co^{III}/Co^{II} couple characteristic of the $[Co(BTP)_2]^{2+}$ component can still be seen at 0.239 V. However, another Co^{III}/Co^{II} couple is observed at 0.89 V, which is attributed to $[Co(NCS)_4]^{2-}$. There are also four ligand-based reduction process consistent

with complexes **5**-**6b**, which appeared at 0.738, -1.085, -1.517 and -2.008 V for complex **6c**. Unfortunately, due to the poor solubility of complex **6c** in MeCN, some of the oxidation peaks might not be observed during the experiment. Similarly, the solubility of the binuclear complex **3** in MeCN was also very poor, as such it prevented the observation of a signal when the CV measurement of complex **7a** was conducted. However; the increased solubility due to the presence of bromide ions resulted in the Co^{III}/Co^{II} redox couple of compound **7b** to be 0.329 V, which is only slightly more positive that complex **6**. In addition, three ligand-based reduction process appeared at -0.845, -1.481 and -2.005 V, which is consistent with complex **6a** and **6b**.

3.3.6 Magnetic properties

In order to probe the magnetic properties of compounds **5**-**7**, dc magnetic susceptibility measurements were completed under a static field of 1000 Oe in the temperature range 1.8-300 K and up to 370 K for **6a** & **6b** (*vide infra*). Under these conditions, an absence of signal was observed for compounds **5a** and **5b**, confirming their diamagnetic electronic configuration. This may be attributed to the strong ligand field/crystal field splitting of the BTP ligand, which is in accordance with other chelating nitrogen-based ligands with various metal centers.[91] However, this drastically contrasts the many reports of spin-crossover behaviour observed in analogous $[FeN_6]^{+2}$ complexes.[165] Thus, BTP may be seen as a terpy analog which may be used as a way to tune the spin state of the metal ion. Conversely, compounds **6a**, **6b**, **6c**, **7a**, and **7b** exhibited paramagnetic behaviour, revealing χT values at 300 K of 0.82, 0.57 3.41, 5.95, and 5.78, respectively.

While the synthesis of **6a** is known, its potential as a magnetic material has not been previously investigated because of its instability under ambient conditions.[91] In order to prevent degradation of the sample, **6a** was dried under reduced pressure overnight and recrystallized from an MeCN solution in an inert atmosphere glovebox *via* diethyl ether diffusion. It must be noted that the magnetic measurements of **6a** and **6b** were conducted in sealed sample holders in order to maintain their integrity. Notably, both samples, **6a** and **6b**, are spin crossover active, giving similar χT *vs.* T plots (Figure 3.15). This gradual spin crossover nature has been observed in many other "terpy-like" Co^{II} motifs.[71-73, 78, 136-138] Sample **6a** undergoes a gradual spin crossover, with χT decreasing from 0.894 cm^3 K mol^{-1} at 370 K, consistent with *ca.* 35% high spin (S = 3/2), to 0.579 cm^3 K mol^{-1}, consistent with *ca.* 13.6% high spin at 1.8 K, comparing to the low spin state (S = 1/2) value of 0.375 cm^3 K mol^{-1}. Even at the lowest possible temperature of 1.8 K, a portion of the

molecules remain in the high spin state, this is not surprising considering that the Jahn-Teller axis in **6a** is not as pronounced as it is in **6b** (*vide supra*). Systems with d^7 electronic configurations and well defined Jahn-Teller elongation axes, are expected to yield a low spin state.[166] Thus, unsurprisingly, **6b** displays a more abrupt and complete spin crossover transition such that the χT product decreases from 0.695 cm^3 K mol^{-1} at 370 K, consistent with *ca.* 21.3% high spin, to 0.402 cm^3 K mol^{-1}, in agreement with the majority of the sample being low spin. These slight differences in the χT *vs.* T profiles of **6a** and **6b** are a direct consequence of the counter anions in the lattice. The presence of ClO_4^- anions appears to have resulted in greater a Jahn-Teller elongation *via* stronger anion-π interactions and in turn results in stabilization of the low spin state. Such effects of coutnerions on the spin crossover properties of molecules has been previously investigated.[165, 167-169] Moreover, at 1.9 K the magnetization saturates for **6a** and **6b** at 1.16 μ_B and 0.77 μ_B, respectively (Figure 3.16 and 3.17) which is in excellent agreement with the expected value for this spin system (1 μ_B), assuming $g = 2$. Additionally, the isothermal reduced magnetization curves are all super-imposed suggesting the absence of angular momentum, this is not surprising given that the low spin state is dominant in these systems at low temperature (Figure 3.16 and 3.17).

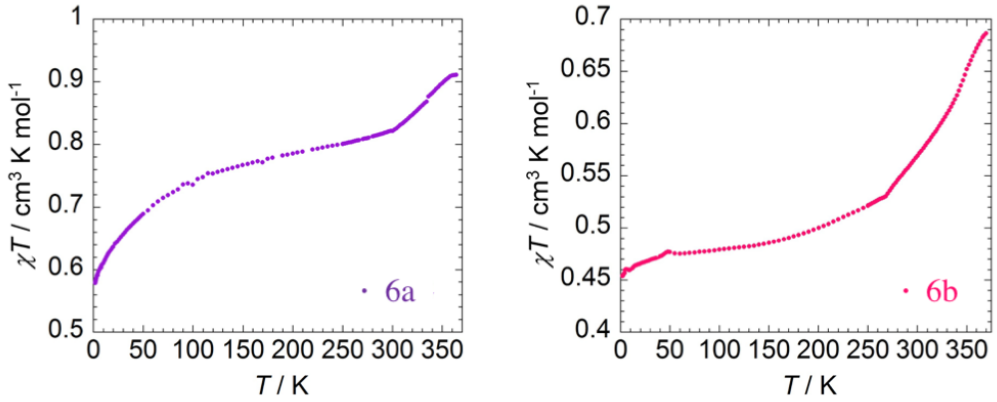

Figure 3.15. Temperature dependence of the χT product at 1000 Oe for **6a** (left), and **6b** (right), with χ being the molar magnetic susceptibility per molecule as defined by $2M/H$.

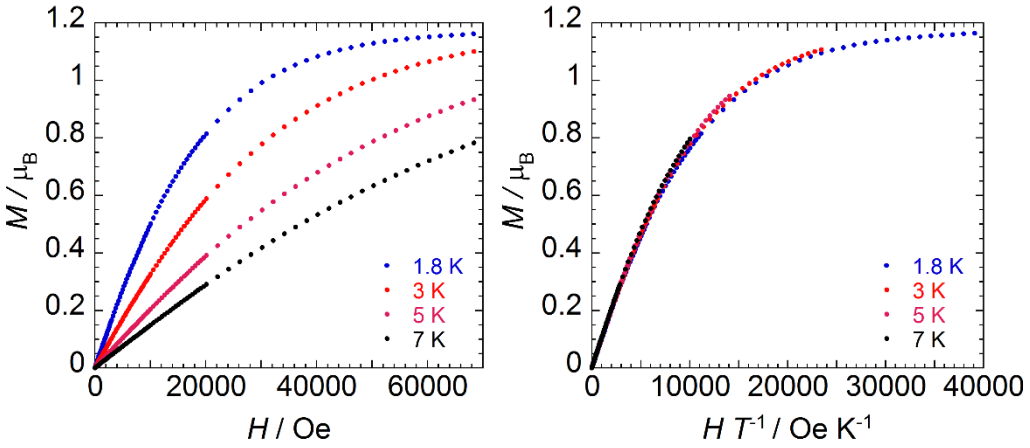

Figure 3.16. Field dependence of the magnetization (left) and reduced magnetization (right) at 1.8, 3, 5 and 7 K for **6a**.

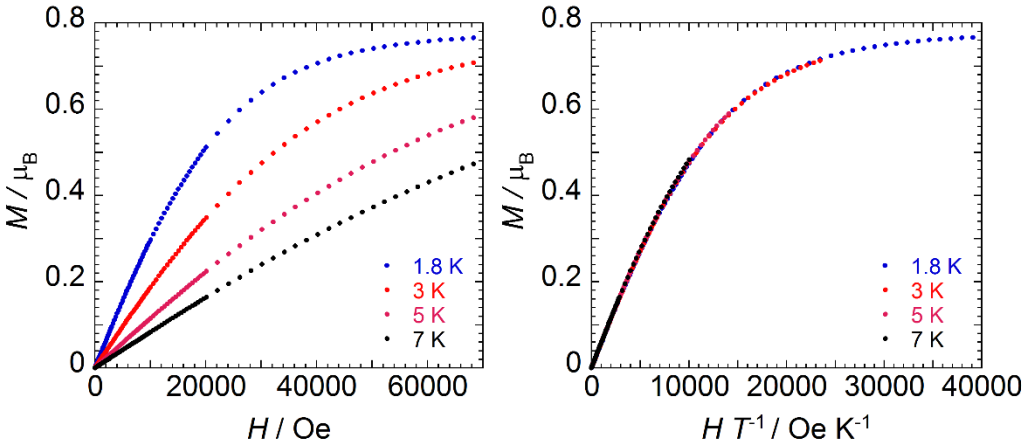

Figure 3.17. Field dependence of the magnetization (left) and the reduced magnetization (right) at 1.8, 3, 5 and 7 K for **6b**.

The room temperature χT value of 3.41 cm^3 K mol^{-1} for **6c** is in good agreement with the expected spin-only value of 3.375 cm^3 K mol^{-1} for two non-interacting Co^{II} ions (Figure 3.19). Due to the presence of the Jahn-Teller elongation in the $[Co(BTP)_2]^{2+}$ a low spin configuration is expected for Co1 in complex **6c**.[166] Subsequently, resulting in spin states of $S = 1/2$ for Co1 and $S = 3/2$ for Co2, which exhibits tetrahedral geometry. Nevertheless, the χT profile of **6c** remains relatively linear upon decreasing temperature, until 12 K, where there is a more precipitous drop, reaching a minimum value of 2.34 cm^3 K mol^{-1} at 1.8 K. The decrease in the χT product is most likely a result of weak antiferromagnetic intermolecular interactions between the complex ion pairs of Co1 and Co2 in **6c**. This interaction was quantified through utilizing the $-2J$ formalism with

PHI software,[170] yielding J = -0.18 cm^{-1} and g = 1.94 (Table 3.7). The best-fit parameters also include a small temperature independent paramagnetism (TIP) contribution of 0.0002 cm^{-1}. While the magnitude of the exchange coupling may seem rather small for transition metal-based systems, it is not surprising given the intermolecular Co1-Co2 distance of 7.894(6) Å. At this distance, characteristically weak coupling is expected. Furthermore, at 1.8 K the magnetization saturates at 3.89 μ_B (Figure 3.18), which is in excellent agreement with the expected value for this spin system (3.88 μ_B), considering the spin-only formula. Additionally, the non-superposition of the reduced magnetization isothermal curves may be a result of unquenched angular momentum (Figure 3.18). Such behaviour is expected to originate from the presence of the tetrahedral Co2, as this geometry has previously elicited slow magnetic relaxation in Co^{II} ions, with significant zero-field splitting parameters (D > - 100 cm^{-1}).[141, 159, 171, 172] Investigation into this did not result in frequency dependent slow magnetic relaxation.

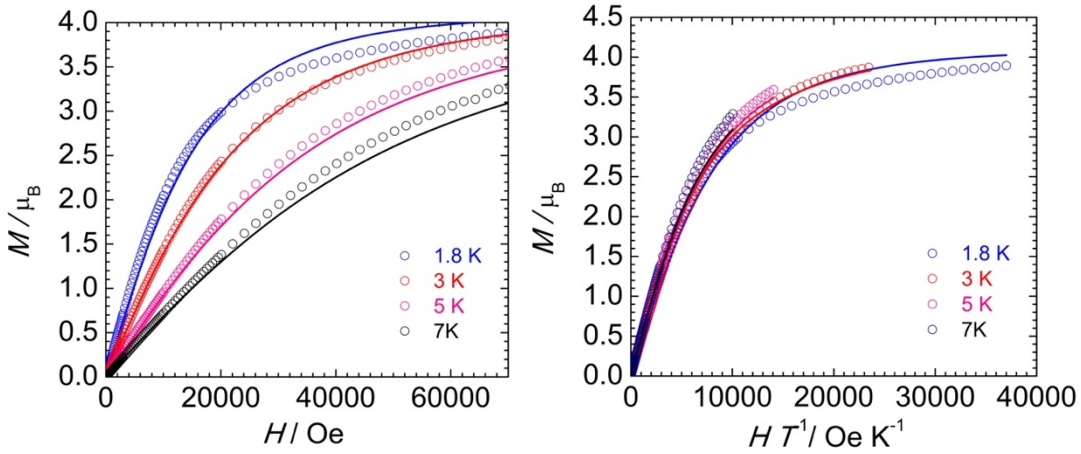

Figure 3.18. Field dependence of the magnetization (left) and the reduced magnetization (right) at 1.8, 3, 5 and 7 K for **6c**. Experimental data is represented by hollow circles and best fits to the data as obtained through *PHI* software are depicted as solid lines.[170]

χT curves of complexes **7a** and **7b** display similar temperature dependent behavior over the range 1.8-300 K, this is not surprising given the similarities in their molecular structures. At room temperature, χT values of 5.95 cm^3 K mol^{-1} for **7a** and 5.78 cm^3 K mol^{-1} for **7b** are obtained. These values are marginally larger than what is expected from the spin-only approximation of 3.76 cm^3 K mol^{-1} for two non-interacting high spin Co^{II} ions with S = 3/2. The larger experimental values are not uncommon in high spin Co^{II} systems, given the large degree of unquenched orbital angular

momentum;[173] in fact, the observed values for **7a** and **7b** lie within the range of previously reported values for similar systems.[172, 174-178] Upon decreasing temperature, the χT products for both **7a** and **7b** progressively decrease to reach local minima at 30 K of 5.31 and 5.29 cm^3 K mol^{-1} for **7a** and **7b**, respectively. Following which, both systems experience an increase in their χT products to 6.09 and 5.86 cm^3 K mol^{-1} at 5.5 K. This is attributed to a weak intramolecular ferromagnetic exchange (*vide infra*). At significantly low temperature (< 5 K), there is a final rapid decrease to reach 5.34 and 5.40 cm^3 K mol^{-1} at 1.8 K for both **7a** and **7b**. This downturn may be a direct consequence of the inherent orbital angular momenta of Co^{II} high spin ions, or the presence of weak intermolecular antiferromagnetic interactions.[139-141]

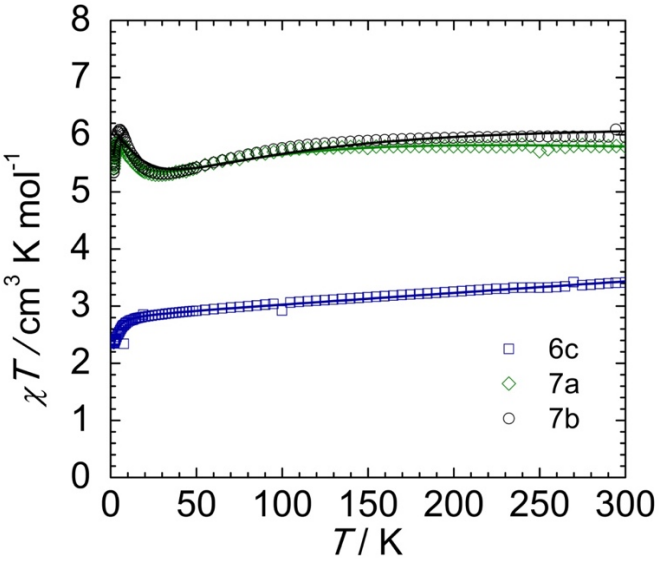

Figure 3.19. Temperature dependence of the χT product at 1000 Oe for **6c**, **7a** and **7b**, with χ being the molar magnetic susceptibility per molecule as defined by *M/H*. Experimental data is represented by hollow circles and best fits to the data as obtained through *PHI* software are depicted as solid lines.[170]

In a similar manner to complex **6c**, the extent of the magnetic exchange was quantified with *PHI* software, using the -2*J* formalism.[170] Only the intramolecular Co-Co interaction was considered for as the intramolecular Co-Co distances of 3.672(6) Å for **7a** and 3.815(4) Å for **7b** are assumed to result in dominant exchange interactions through the μ-halides. In fact, the best fit parameters obtained demonstrate that this interaction is overall ferromagnetic in nature, producing J = +2.57 cm^{-1} and g = 2.16 for compound **7a**, and J = +2.98 cm^{-1} and g = 2.21 for **7b**. This

dominant ferromagnetic interaction has only been observed a few times in other cobalt chloride-based dimers.[174, 178] Furthermore, at 1.8 K the magnetization saturates at 4.40 μ_B for **3a** and 4.41 μ_B for **7b** (Figure 3.20 and 3.21), which is in excellent agreement with the expected value for these spin system (4.60 μ_B and 4.52 μ_B), considering the spin-only formula. Additionally, the non-superposition of the reduced magnetization isotemperature curves may be a result of unquenched angular momentum (Figure 3.20 and 3.21).

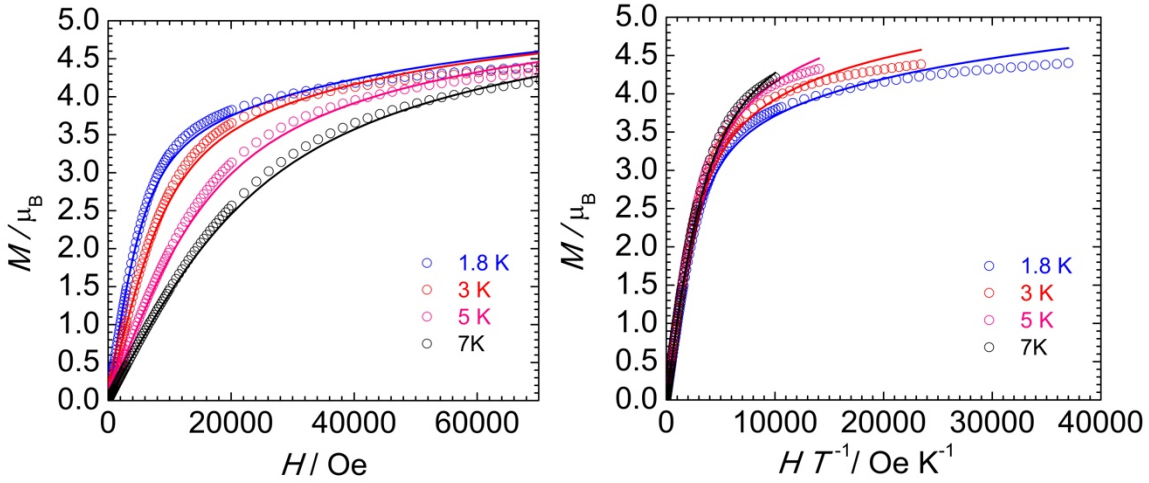

Figure 3.20. Field dependence of the magnetization (left) and the reduced magnetization (right) at 1.8, 3, 5 and 7 K for **7a**. Experimental data is represented by hollow circles and best fits to the data as obtained through *PHI* software are depicted as solid lines.[170]

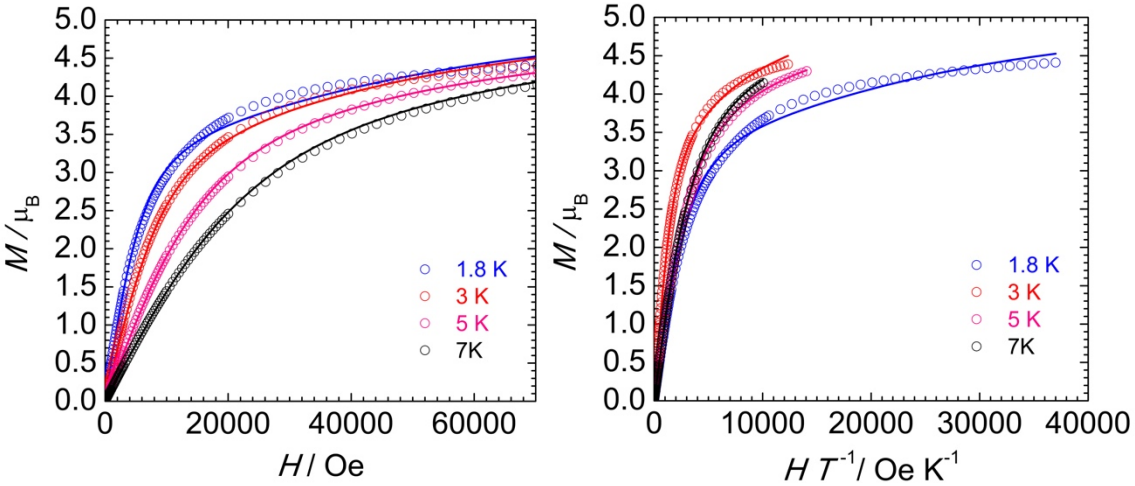

Figure 3.21. Field dependence of the magnetization (left) and the reduced magnetization (right) at 1.8, 3, 5 and 7 K for **7b**. Experimental data is represented by hollow circles and best fits to the data as obtained through *PHI* software are depicted as solid lines.[170]

Table 3.7. Selected magnetic parameters for complex **6c**, **7a** and **7b**.

	6c	**7a**	**7b**
***J* (cm^{-1})**	-0.18	+2.57	+2.98
g	1.94	2.16	2.21

3.3.7 Proposed super-exchange mechanism

To propose an explanation for the observed ferromagnetic interactions in complexes **7a** and **7b** a comparative literature study was completed with other cobalt dimers bridged through μ-chlorides.[131, 178-183] A comparison of the bridging angles and resulting coupling values are compiled in Figure 3.22.

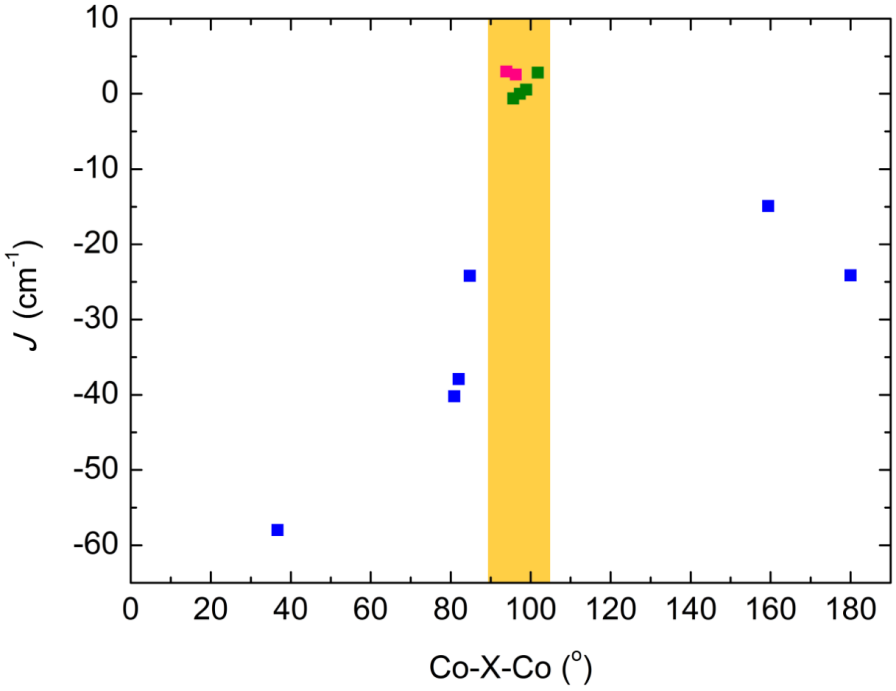

Figure 3.22. Compilation of the magnetic behavior of several Co^{II} dimer with chloride bridge. Highlighted region indicates Co-X-Co (X =F, Cl, Br and I) bond angles that lead to ferromagnetic exchange interactions. [174, 178, 180-182, 184-186]

Remarkably, a clear trend can be observed between the magnitude of the Co-X-Co (X = F, Cl, Br, and I) angle and the magnetic coupling parameter, *J*. Here, a switch from antiferromagnetic exchange to ferromagnetic exchange occurs approximately when the Co-X-Co angle approaches 90°. Within this context, molecules that showed a Co-X-Co angle less than 90° displayed

antiferromagnetic coupling, as well as when that angle was larger than 100°. This leaves a narrow window, *ca.* 10°, between 90-100°, where ferromagnetic exchange is observed. This trend may be explained by considering the relative orbital overlap between the *d*-orbitals of the metal centers and the *p*-orbitals of the bridging chlorides. The small range of 90-100°, suggests that favorable orbital overlap occurs within this range, allowing for the observation of ferromagnetic exchange. Such characteristics are reminiscent of the early work by Hatfield and Hodgson's on a series of Cu^{II} dimers bridged by hydroxyl groups.[187-192] They describe the magnetostructural correlation based on the degree of orbital overlap between the Cu^{II} d_{xy} orbital with the *p*-orbitals of the bridging moieties. Where ferromagnetic exchange is achieved when there is equal orbital overlap with both the p_x and p_y orbitals. This is a rather simple model which takes advantage of the single magnetically active orbital of Cu^{II}. However, with a Co^{II} ion (S = 3/2), it is more difficult to describe such interactions by simply considering the antisymmetric and symmetric combinations of the metal-ligand bonding as there are more magnetically active *d*-orbitals. When the inherent magnetic anisotropy of the Co^{II} ion is considered, the picture rapidly becomes more complex, and thus a simple model of considering orbital overlap with the superexchange orbitals may not be entirely accurate. With respect to compounds **7a** and **7b**, we speculate that within this bonding arrangement that the e_g set of orbitals are participating dominantly in the superexchange pathway, such that the d_z orbital would be aligned with the Cl1a-Co1-Cl2 axis in **7a**. Nevertheless, with positive *J*-values and Co-X-Co angles of 96.30(2)° and 93.910(11)°, compounds **7a** and **7b** satisfy the trend observed with the other Co-X-Co molecules in the literature.

3.4 Conclusion and future work

In summary, a series of new complexes **5-7** namely $[Fe^{II}(BTP)_2](BF_4)_2{\cdot}4MeCN{\cdot}Et_2O$ (**5a**), $[Fe^{II}(BTP)_2](ClO_4)_2{\cdot}2MeOH$ (**5b**), $[Co^{II}(BTP)_2](BF_4)_2{\cdot}3MeCN$ (**6a**), $[Co^{II}(BTP)_2](ClO_4)_2{\cdot}4MeCN$ (**6b**), $[Co^{II}(BTP)_2][Co^{II}(NCS)_4]$ (**6c**), $[Co^{II}_2(\mu^2\text{-}Cl)_2(BTP)_2Cl_2]$ (**7a**), $[Co^{II}_2(\mu^2\text{-}Br)_2(BTP)_2Br_2]{\cdot}MeCN$ (**7b**) have been successfully prepared, isolated *via* complexation of BTP with Fe^{II}/Co^{II} and various anions (e.g. BF_4^-, ClO_4^-, NCS^-, Cl^- and Br^-), and characterised structurally, together with detailed probing of their solution electrochemistry and solid-state magnetic behaviour. These $[M^{II}(BTP)_2]^{2+}$ (M = Fe or Co) complexes with BF_4^-, ClO_4^- and $[Co(NCS)_4]^{2-}$ anions were explored to probe the effect of anion-π interactions on the supramolecular packing arrangement and to

examine their influence on the subsequent physical properties. In particular, complexes **5** and **6** crystallize as Fe^{II} or Co^{II} centered complexes with distorted octahedral environments. Intriguingly, in the Co^{II} examples, Jahn-Teller elongations are observed, such that a more pronounced elongation is observed when replacing the BF_4^- anions with ClO_4^- anions. And, consequently, an even larger distortion is observed with NCS^- anions; giving rise to a coordination salt, with which the octahedral motif remains but adding a Co^{II} centered tetrahedral coordinated by four NCS^- anions. Conversely, complex **7** is composed of a dinuclear cobalt complex which is bridged by two halide anions, either chloride or bromide.

As might be expected due to their structural similarities, electrochemical studies for **5**-**7** are quite comparable. Most of the metal-centered redox processes were reversible or partially reversible, and fall in a range of $0.13 < E_{1/2} < 0.90$ V *vs.* Fc/Fc^+. In addition to these oxidations, all of the complexes showed up to four reductive processes in the MeCN window and these redox processes are partially reversible or irreversible. In terms of the magnetic properties, complex **5** is diamagnetic due to the low spin state of the metal center. Complex **7** exhibit paramagnetic behaviour typical for dinuclear $S = 3/2$ complexes in weak ferromagnetic interactions.

Based on the studies described here, we can see that counter anions play a significant role on the packing arrangement as well as the coordination environment in the solid-state structure of the resulting coordination complex. While this results in minimal differences in the electrochemical properties of the complexes, it significantly effects the magnetic properties. By varying the anions of the $[Co(BTP)_2]^{2+}$, varying degrees of Jahn-Teller elongations are observed, and this either results in spin crossover behaviour, or simply a low-spin state. This is in stark contrast to the diamagnetism inherent to the $[Fe(BTP)_2]^{2+}$ derivatives, which collectively demonstrates the ability to tune the spin-state of metal ions, both through careful ligand and anion selections.

4 Conclusions and outlook

The work presented herein aims to investigate the synthesis and characterizations of the complexation of two terpy analogues ligands with redox active properties (i.e. BTZP and BTP). Both BTZP and BTP can be reduced based on the electrochemical studies on free ligands. However, the redox activities after complexation remains largely unexplored; in fact, the coordination environment may affect the radical state of ligand, for the metal center would have more electron density which may stabilize the radical state of the ligand. Both BTZP and BTP have the potential to be reduced as a monoradical or diradical and moreover, after coordinating with metal ions, those ligands have increased potential to achieve the radical state, because of the various coordination environments. Indeed, monoradicals have S=1/2 and diradicals have S=1 and they are ideal candidates in terms of magnetic applications, such as superexchange coupling, SMM, single chain magnet etc. In turn, these two redox active ligands lead to investigations of new performing magnetic materials.

In chapter 2, a series of first and second row transition metal complexes, namely, $[Co^{II}(BTZP)_2](ClO_4)_2 \cdot 3MeCN$(**1**), $[[Ni^{II}(BTZP)(MeCN)_3](ClO_4)_2]$ (**2**), $[Ni^{II}Cl_2(BTZP)(MeCN)] \cdot 2MeCN \cdot H_2O$ (**3a**), $[Ni^{II}Cl_2(BTZP)(MeCN)] \cdot MeCN$ (**3b**), $\{[Cd^{II}(BTZP)(NO_3)_2]\}_n$ (**4**) was prepared while the presence of BTZP, with various Co(II), Ni(II) and Cd(II) salts. All complexes were structurally, electrochemically and magnetically characterized. Since complexes **1-3** are discrete molecules, there are a lot of similarities in the various characterization studies. To be specific, the crystal structure of **1** reveals a classic $[CoN_6]^{2+}$ inorganic core coordinating through a tridentate 'terpy-like' pocket, with a Jahn-Teller compression. Complexes **2** and **3** present a nearly perfect octahedral geometry with only one BTZP ligand with other three weak ligands with a monodentate coordination mode. Conversely, complex **4** crystalized as a 1-D coordination polymer, which has a repeating unit of $[Cd^{II}(BTZP)(NO_3)_2]$ bridged by two μ-nitrate bridges. Complexes **1-3** showed similar results in optical spectroscopy and magnetic studies. However, electrochemical studies presented that only complex **1** is relatively stable during the redox process. This lead us to investigate whether the replacement of the ligand can see the same result.

Due to the perfect reversible redox process of the radical state of complex **1** observed by electrochemical data, we decided to synthesize a series of complexes with the similar structure with **1** by varying different anions. Since the complexation of BTP and lanthanides are shown in the previous literature studies,[90, 96] this work is mainly aimed on exploring the coordination chemistry of BTP in the first row transition metals. In chapter 3, the solid-state structure of a family of 3-d transition metal complexes of BTP were reported. In this series, five complexes have a general formula $[M^{II}(BTP)_2]^{2+}$ (M = Fe or Co) with coordination through the tridentate 'terpy-like' pocket,[116] and two dimeric complexes of the $[Co^{II}(\mu\text{-}X)_2(BTP)_2X_2]$ (X = Cl or Br) which are bridged by halides were obtained. We have structurally characterised all of these BTP complexes and completed their electrochemical studies as well as investigated their spin states through magnetometry. The two $[Fe^{II}(BTP)_2]^{2+}$ compounds are diamagnetic due to their low spin electron configuration in the metal center. Notably, there are two $[Co^{II}(BTP)_2]^{2+}$ compounds that are spin crossover active. Additionally, the dimeric species allow for a unique opportunity to study the superexchange coupling between two high-spin cobalt metal centers through halide bridges in the $[M^{II}(\mu\text{-}X)_2(BTP)_2X_2]$ coordination motif.

To the best of our knowledge, as it might be expected the complexity of synthesizing and isolating the radical state of BTZP and BTP, there is no literature result of the crystal structures and magnetic results involving a radical state of either ligand. Investigations to further explore and understand the redox chemistry by isolating the radical state of both ligands and new magnetic materials by reducing complexes showed in chapter 2 and 3 or coordinating the metal center and the radical state of ligands are currently underway.

References

1. G. B. Yelyakov, V. A. Stonik and T. N. Makaryeva, *Khim. Geterotsikl. Soedin.*, 1977, **13**, 435.

2. B. M. Krasovitskii and B. M. Bolotin, *Khim. Geterotsikl. Soedin.*, 1974, **11**, 1443.

3. K. Dhanabalan, T. Sadhasivam, J. H. Park, H. Y. Jung, B. S. Kim and S. H. Roh, *Fuel Cells*, 2017, **17**, 278.

4. V. M. Ivanov, *J. Anal. Chem. USSR.*, 1976, **31**, 810.

5. L. B. Salam, M. O. Ilori and O. O. Amund, *3 Biotech*, 2017, **7**, 11.

6. S. K. Fung, T. T. Zou, B. Cao, P. Y. Lee, Y. M. E. Fung, D. Hu, C. N. Lok and C. M. Che, *Angew. Chem. Int. Ed*, 2017, **56**, 3892.

7. Y. L. L. Xiong, *Ann. N. Y. Acad. Sci.*, 2017, **1398**, 37.

8. T. A. Khattab, M. H. Elnagdi, K. M. Haggaga, A. A. Abdelrahmana and S. A. Aly, *AATCC J. Res.*, 2017, **4**, 1.

9. T. Y. Li, T. Meyer, R. Meerheim, M. Hoppner, C. Korner, K. Vandewal, O. Zeika and K. Leo, *J. Mater. Chem. A*, 2017, **5**, 10696.

10. B. J. Walekar, S. R. Mane and P. N. Bhosale, *Adv. Powder Technol.*, 2017, **36**, 243.

11. G. R. Jenness, W. M. Wan, J. G. G. Chen and D. G. Vlachos, *Acs Catal.*, 2016, **6**, 7002.

12. J. A. Elvidge, J. R. Jones and R. Salih, *J. Chem. Soc., Perkin Trans. 2*, 1979, **0**, 1590.

13. L. Saso, *Mini-Rev. Med. Chem.*, 2013, **13**, 317.

14. C. Medana, P. Calza, A. Deagostino, F. Dal Bello, E. Raso and C. Baiocchi, *J. Mass Spectrom.*, 2011, **46**, 782.

15. S. Kumar, R. K. Singh, B. Patial, S. Goyal and T. R. Bhardwaj, *J. Enzyme Inhib. Med. Chem.,* 2016, **31**, 173.

16. V. I. Poltev, *Kristallografiya*, 1977, **22**, 453.

17. H. Groger, M. Hatam, J. Kintscher and J. Martens, *Synth. Commun.*, 1996, **26**, 3383.

18. P. Imming, R. Mohr, E. Muller, W. Overheu and G. Seitz, *Angew. Chem. Int. Ed.*, 1982, **21**, 284.

19. R. E. Sammelson, M. M. Olmstead, M. J. Haddadin and M. J. Kurth, *J. Org. Chem.*, 2000, **65**, 9265.

20. M. J. Hearn and F. Levy, *Org. Prep. Proced. Int.*, 1987, **19**, 215.

21. S. Mayer and K. Lang, *Stuttg.*, 2017, **49**, 830.

22. R. Ben Chaabane, R. Guermazi, G. Clavier, P. Audebert and A. Hedhli, *Dyes Pigm.*, 2014, **108**, 64.

23. D. E. Chavez, S. K. Hanson, J. M. Veauthier and D. A. Parrish, *Angew. Chem. Int. Ed.*, 2013, **52**, 6876.

24. D. E. Chavez, B. C. Tappan, M. A. Hiskey, S. F. Son, H. Harry, D. Montoya and S. Hagelberg, *Propellants Explos. Pyrotech.*, 2005, **30**, 412.

25. D. E. Chavez, M. A. Hiskey and D. L. Naud, *Propellants Explos. Pyrotech.,* 2004, **29**, 209.

26. T. Reiner, E. J. Keliher, F. Emmetiere, J. S. Lewis and R. Weissleder, *J. Label. Compd. Radiopharm.*, 2013, **56**, S47.

27. R. Kumar, A. D. Singh, J. Singh, H. Singh, R. K. Roy and A. Chaudhary, *Mini-Rev. Med. Chem.*, 2014, **14**, 72.

28. J. Saravanan, S. Mohan and J. J. Roy, *Eur. J. Med. Chem.*, 2010, **45**, 4365.

29. R. M. Abdel-Rahman, M. S. T. Makki, T. E. Ali and M. A. Ibrahim, *Curr. Org. Chem.*, 2013, **10**, 136.

30. I. M. Labouta, N. H. Eshba and H. M. Salama, *Monatsh. Chem.*, 1988, **119**, 591.

31. A. Tobe and T. Kobayashi, *Jpn. J. Pharmacol.*, 1976, **26**, 559.

32. S. Shibamoto, T. Nishimura and H. Fukuyasu, *Yakugaku Zasshi*, 1986, **106**, 54.

33. M. Mojzych, *J. Chem. Soc. Pak.*, 2011, **33**, 698.

34. R. M. Abdel-Rahman, J. M. Morsy, F. Hanafy and H. A. Amene, *Pharmazie*, 1999, **54**, 347.

35. R. M. Abdel-Rahman, *Pharmazie*, 2001, **56**, 18.

36. J. Wieczorek, M. Mordarski, A. Rykowski and P. Nantkanamirski, *Arch. Immunol. Ther. Exp.*, 1980, **28**, 727.

37. M. F. Reich, P. F. Fabio, V. J. Lee, N. A. Kuck and R. T. Testa, *J. Med. Chem.*, 1989, **32**, 2474.

38. S. Konno, M. Sagi, C. Kimura, J. Kikuchi, H. Yamanaka, F. Fujita, Y. Yamada and M. Adachi, *Yakugaku Zasshi*, 1988, **108**, 142.

39. M. K. Tennant, D. S. Hill, J. C. Eldridge, L. T. Wetzel, C. B. Breckenridge and J. T. Stevens, *J. Toxicol. Environ. Health.*, 1994, **43**, 197.

40. D. Q. Tran, K. Y. Kow, J. A. McLachlan and S. F. Arnold, *Biochem. Biophys. Res. Commun.*, 1996, **227**, 140.

41. K. Ban, S. Duffy, Y. Khakham, V. M. Avery, A. Hughes, O. Montagnat, K. Katneni, E. Ryan and J. B. Baell, *Bioorganic Med. Chem. Lett.*, 2010, **20**, 6024.

42. C. Maxim, A. Matni, M. Geoffroy, M. Andruh, N. G. R. Hearns, R. Clerac and N. Avarvari, *New J. Chem*, 2010, **34**, 2319.

43. C. P. Constantinides, E. Obijalska and P. Kaszynski, *Org. Lett.*, 2016, **18**, 916.

44. G. Giacomelli, A. Porcheddu and L. De Luca, *Curr. Org. Chem.*, 2004, **8**, 1497.

45. I. Prejmereanu, I. Sebe and L. Floru, *Rev. Chim.*, 1994, **45**, 853.

46. K. Mori, H. Hirahara, Y. Oishi and H. Sasaki, *Mater. Trans.*, 2001, **42**, 1219.

47. E. Topp and W. Smith, *J. Environ. Qual.*, 1992, **21**, 316.

48. D. A. S. Phillips, R. Reisel and A. H. M. Renfrew, *Color. Technol.*, 2008, **124**, 173.

49. M. Yang, Y. J. Liu, H. B. Chen, D. G. Yang and H. M. Li, *ACS Appl. Mater. Interfaces*, 2016, **8**, 28615.

50. M. H. Keshavarz and O. R. Syadat, *Asian J. Chem.*, 2007, **19**, 965.

51. J. K. Srivastava, N. T. Awatade, H. R. Bhat, A. Kmit, K. Mendes, M. Ramos, M. D. Amaral and U. P. Singh, *RSC Adv.*, 2015, **5**, 88710.

52. R. T. Boere and T. L. Roemmele, *Coord. Chem. Rev.*, 2000, **210**, 369.

53. K. L. M. Harriman, A. A. Leitch, S. A. Stoian, F. Habib, J. L. Kneebone, S. I. Gorelsky, I. Korobkov, S. Desgreniers, M. L. Neidig, S. Hill, M. Murugesu and J. L. Brusso, *Dalton Trans.*, 2015, **44**, 10516.

54. M. A. Lemes, A. Pialat, S. N. Steinmann, I. Korobkov, C. Michel and M. Murugesu, *Polyhedron*, 2016, **108**, 163.

55. W. Kaim, *Coord. Chem. Rev.*, 2002, **230**, 127.

56. A. Halasz and J. Hawari, *Aquatic Redox Chemistry*, 2011, **1071**, 441.

57. A. K. Hui, Y. Losovyj, R. L. Lord and K. G. Caulton, *Inorg. Chem.*, 2014, **53**, 3039.

58. T. Hattich and U. Kunze, *Angew. Chem. Int. Ed*, 1982, **21**, 364.

59. S. Mishra and K. M. Purohit, *Indian J. Chem. Technol.*, 1988, **27**, 78.

60. G. F. Condike and A. E. Martell, *Polyhedron*, 1969, **31**, 2455.

61. M. H. Sipponen, O. J. Rojas, V. Pihlajaniemi, K. Lintinen and M. Osterberg, *ACS Sustain. Chem. Eng.*, 2017, **5**, 1054.

62. J. W. Park, J. H. Park and C. H. Jun, *J. Org. Chem*, 2008, **73**, 5598.

63. C. H. Jun, C. W. Moon and D. Y. Lee, *Chem. Eur. J.*, 2002, **8**, 2423.

64. S. Korwar, K. Brinkley, A. R. Siamaki, B. F. Gupton and K. C. Ellis, *Org. Lett.*, 2015, **17**, 1782.

65. J. H. Lee, E. A. Jo and C. H. Jun, *Synlett*, 2009, **66**, 2647.

66. K. H. Thompson, Y. Tsukada, Z. M. Xu, M. Battell, J. H. McNeill and C. Orvig, *Biol. Trace Elem. Res.*, 2002, **86**, 31.

67. A. Christoforidis, A. Haritandi, I. Tsatra, I. Tsitourides, S. Karyda and M. Athanassiou-Metaxa, *Eur. J. Haematol*, 2007, **78**, 52.

68. W. Z. Fang, Y. P. Wang, Y. F. Wang, S. C. Zhang and X. Y. Yi, *RSC Adv.*, 2015, **5**, 8996.

69. J. W. Ciszek, Z. K. Keane, L. Cheng, M. P. Stewart, L. H. Yu, D. Natelson and J. M. Tour, *J. Am. Chem. Soc.*, 2006, **128**, 3179.

70. L. M. Yan and J. M. Seminario, *J. Phys. Chem. A*, 2005, **109**, 6628.

71. X. Zhang, Z. X. Wang, H. M. Xie, M. X. Li, T. J. Woods and K. R. Dunbar, *Chem. Sci*, 2016, **7**, 1569.

72. R. G. Miller and S. Brooker, *Inorg. Chem.*, 2015, **54**, 5398.

73. J. Palion-Gazda, A. Switlicka-Olszewska, B. Machura, T. Grancha, E. Pardo, F. Lloret and M. Julve, *Inorg. Chem.*, 2014, **53**, 10009.

74. X. Zhang, H. M. Xie, M. Ballesteros-Rivas, Z. X. Wang and K. R. Dunbar, *J. Mater. Chem. C*, 2015, **3**, 9292.

75. I. Bhowmick, D. J. Boston, R. F. Higgins, C. M. Klug, M. P. Shores and T. Gupta, *Sens. Actuator B-Chem.*, 2016, **235**, 325.

76. N. S. S. Kumar, M. Z. Shafikov, A. C. Whitwood, B. Donnio, P. B. Karadakov, V. N. Kozhevnikov and D. W. Bruce, *Chem. Eur. J.*, 2016, **22**, 8215.

77. N. W. Alcock, P. R. Barker, J. M. Haider, M. J. Hannon, C. L. Painting, Z. Pikramenou, E. A. Plummer, K. Rissanen and P. Saarenketo, *J. Chem. Soc., Dalton Trans.*, 2000, **0**, 1447.

78. Y. Guo, X. L. Yang, R. J. Wei, L. S. Zheng and J. Tao, *Inorg. Chem*, 2015, **54**, 7670.

79. E. C. Constable, C. E. Housecroft, G. E. Schneider, J. A. Zampese, H. J. Bolink, A. Pertegas and C. Roldan-Carmona, *Dalton Trans.*, 2014, **43**, 4653.

80. B. Liu, L. Hou, W. P. Wu, A. N. Dou and Y. Y. Wang, *Dalton Trans.*, 2015, **44**, 4423.

81. N. Elgrishi, M. B. Chambers, V. Artero and M. Fontecave, *Phys. Chem. Chem. Phys.*, 2014, **16**, 13635.

82. A. R. Mazzotti, M. G. Campbell, P. P. Tang, J. M. Murphy and T. Ritter, *J. Am. Chem. Soc.*, 2013, **135**, 14012.

83. N. J. Yutronkie, I. A. Kuhne, I. Korobkov, J. L. Brusso and M. Murugesu, *ChemComm.*, 2016, **52**, 677.

84. C. R. Benson, A. K. Hui, K. Parimal, B. J. Cook, C. H. Chen, R. L. Lord, A. H. Flood and K. G. Caulton, *Dalton Trans.*, 2014, **43**, 6513.

85. A. K. Hui, R. L. Lord and K. G. Caulton, *Dalton Trans.*, 2014, **43**, 7958.

86. P. Ghosh, S. Samanta, S. K. Roy, S. Demeshko, F. Meyer and S. Goswami, *Inorg. Chem*, 2014, **53**, 4678.

87. L. Hu, W. Liu, C. H. Li, X. H. Zhou and J. L. Zuo, *Eur. J. Inorg. Chem.*, 2013, **2013**, 6037.

88. C. Stroh, P. Turek, P. Rabu and R. Ziessel, *Inorg. Chem*, 2001, **40**, 5334.

89. M. S. Alam, M. Stocker, K. Gieb, P. Muller, M. Haryono, K. Student and A. Grohmann, *Angew. Chem. Int. Ed.*, 2010, **49**, 1159.

90. C. Boucher, M. G. B. Drew, P. Giddings, L. M. Harwood, M. J. Hudson, P. B. Iveson and C. Madic, *Inorg. Chem. Comm.*, 2002, **5**, 596.

91. L. J. K. Cook, F. Tuna and M. A. Halcrow, *Dalton Trans.*, 2013, **42**, 2254.

92. J. Sauer, D. K. Heldmann and G. R. Pabst, *Euro. J. Org. Chem*, 1999, **1999**, 313.

93. T. Ishizuka, L. E. Sinks, K. Song, S. T. Hung, A. Nayak, K. Clays and M. J. Therien, *J. Am. Chem. Soc.*, 2011, **133**, 2884.

94. A. K. Hui, C. H. Chen, A. M. Terwilliger, R. L. Lord and K. G. Caulton, *Acta Crystallogr. C*, 2014, **70**, 250.

95. A. K. Hui, B. J. Cook, D. J. Mindiola and K. G. Caulton, *Inorg. Chem.*, 2014, **53**, 3307.

96. A. Bhattacharyya, E. Kim, P. F. Weck, P. M. Forster and K. R. Czerwinski, *Inorg. Chem.*, 2013, **52**, 761.

97. A. N. Kharat, A. Bakhoda and B. T. Jahromi, *Polyhedron*, 2011, **30**, 2768.

98. T. Yutaka, L. Mori, M. Kurihara, N. Tamai and H. Nishihara, *Inorg. Chem.*, 2003, **42**, 6306.

99. A. M. Goforth, M. A. Tershansy, M. D. Smith, L. Peterson, J. G. Kelley, W. J. I. DeBenedetti and H. C. zur Loye, *J. Am. Chem. Soc.*, 2011, **133**, 603.

100. M. Chen, S. M. Ng, S. M. Yiu, K. C. Lau, R. J. Zeng and T. C. Lau, *ChemComm.*, 2014, **50**, 14956.

101. D. A. Roberts, B. S. Pilgrim, J. D. Cooper, T. K. Ronson, S. Zarra and J. R. Nitschke, *J. Am. Chem. Soc.*, 2015, **137**, 10068.

102. N. M. Shavaleev, S. J. A. Pope, Z. R. Bell, S. Faulkner and M. D. Ward, *Dalton Trans.*, 2003, **0**, 808.

103. S. Samanta, S. Das and P. Biswas, *J. Org. Chem.*, 2013, **78**, 11184.

104. S. Samanta, S. Ray, A. B. Ghosh and P. Biswas, *RSC Adv.*, 2016, **6**, 39356.

105. S. Samanta and P. Biswas, *RSC Adv.*, 2015, **5**, 84328.

106. D. E. Chavez, M. A. Hiskey and R. D. Gilardi, *Angew. Chem. Int. Ed*, 2000, **39**, 1791.

107. T. Troll, *Electrochim. Acta.*, 1982, **27**, 1311.

108. A. C. Knall and C. Slugovc, *Chem. Soc. Rev.*, 2013, **42**, 5131.

109. R. Gross and W. Kaim, *Inorg. Chem*, 1987, **26**, 3596.

110. M. A. Lemes, G. Brunet, A. Pialat, L. Ungur, I. Korobkov and M. Murugesu, *ChemComm.*, 2017, **53**, 8660.

111. K. Neumann, S. Jain, J. Geng and M. Bradley, *ChemComm.*, 2016, **52**, 11223.

112. T. Lacelle, G. Brunet, A. Pialat, R. J. Holmberg, Y. Lan, B. Gabidullin, I. Korobkov, W. Wernsdorfer and M. Murugesu, *Dalton Trans.*, 2017, **46**, 2471.

113. A. S. Lytvynenko, R. A. Polunin, M. A. Kiskin, A. M. Mishura, V. E. Titov, S. V. Kolotilov, V. M. Novotortsev and I. L. Eremenko, *Theor. Exp. Chem.*, 2015, **51**, 54.

114. J. Jacquet, M. Desage-El Murr and L. Fensterbank, *Chemcatchem*, 2016, **8**, 3310.

115. D. L. Jameson, L. E. Guise, C. A. Bessel and K. Takeuchi, *Inorg. Synth.*, 1998, **32**, 46.

116. J. M. Frost, L. Kobera, A. Pialat, Y. X. Zhang, S. A. Southern, B. Gabidullin, D. L. Bryce and M. Murugesu, *ChemComm.*, 2016, **52**, 10680.

117. B. V. Rao, S. Dhokale, P. R. Rajamohanan and S. Hotha, *ChemComm.*, 2013, **49**, 10808.

118. D. Casanova, M. Llunell, P. Alemany and S. Alvarez, *Chem. Eur. J.*, 2005, **11**, 1479.

119. B. N. Figgis, E. S. Kucharski and A. H. White, *Aust. J. Chem.*, 1983, **36**, 1527.

120. H. Oshio, H. Spiering, V. Ksenofontov, F. Renz and P. Gutlich, *Inorg. Chem.*, 2001, **40**, 1143.

121. N. Zhang, J. Yang, R. X. Hu and M. B. Zhang, *Z. Anorg. Allg. Chem.*, 2013, **639**, 197.

122. E. C. Constable, K. Harris, C. E. Housecroft, M. Neuburger and J. A. Zampese, *CrystEngComm*, 2010, **12**, 2949.

123. E. A. Medlycott, K. A. Udachin and G. S. Hanan, *Dalton Trans.*, 2007, **0**, 430.

124. J. England, E. Bill, T. Weyhermuller, F. Neese, M. Atanasov and K. Wieghardt, *Inorg. Chem.*, 2015, **54**, 12002.

125. A. Bondi, *J. Phys. Chem.*, 1964, **68**, 441.

126. Y. G. Ma, H. Y. Zhang, J. C. Shen and C. M. Che, *Synth. Met.*, 1998, **94**, 245.

127. J. K. Klosterman, A. Linden, D. K. Frantz and J. S. Siegel, *Dalton Trans.*, 2010, **39**, 1519.

128. H. Oshio, *Inorganica Chim. Acta*, 2001, **324**, 188.

129. G. Kaur, M. I. J. Polson and R. M. Hartshorn, *Dalton Trans.*, 2015, **44**, 4200.

130. B. K. Santra and G. K. Lahiri, *J. Chem. Soc., Dalton Trans.*, 1998, **0**, 139.

131. P. Ghosh, S. Samanta, S. K. Roy, S. Joy, T. Kramer, J. E. McGrady and S. Goswami, *Inorg. Chem.*, 2013, **52**, 14040.

132. E. Belhadj, A. El-Ghayoury, E. Ripaud, L. Zorina, M. Allain, P. Batail, M. Mazari and M. Salle, *New J. Chem.*, 2013, **37**, 1427.

133. H. Kon and T. Nagata, *Dalton Trans.*, 2013, **42**, 5697.

134. S. F. Rach and F. E. Kuhn, *Chem. Rev.,* 2009, **109**, 2061.

135. U. Demir and C. Shannon, *Abstracts of Papers of the American Chemical Society*, 1996, **212**, 28.

136. W. X. C. Oliveira, C. L. M. Pereira, C. B. Pinheiro, K. Krambrock, T. Grancha, N. Moliner, F. Lloret and M. Julve, *Polyhedron*, 2016, **117**, 710.

137. Y. H. Lee, M. S. Won, J. M. Harrowfield, S. Kawata, S. Hayami and Y. Kim, *Dalton Trans.*, 2013, **42**, 11507.

138. Y. Komatsu, K. Kato, Y. Yamamoto, H. Kamihata, Y. H. Lee, A. Fuyuhiro, S. Kawata and S. Hayami, *Eur. J. Inorg. Chem.*, 2012, **2012**, 2769.

139. J. M. Frost, K. L. M. Harriman and M. Murugesu, *Chem. Sci.*, 2016, **7**, 2470.

140. G. Brunet, D. A. Safin, J. Jover, E. Ruiz and M. Murugesu, *J. Mater. Chem. C*, 2017, **5**, 835.

141. J. Caballero-Jimenez, F. Habib, D. Ramirez-Rosales, R. Grande-Aztatzi, G. Merino, I. Korobkov, M. K. Singh, G. Rajaraman, Y. Reyes-Ortega and M. Murugesu, *Dalton Trans.*, 2015, **44**, 8649.

142. G. Ulas and G. W. Brudvig, *J. Am. Chem. Soc.*, 2011, **133**, 13260.

143. Z. Y. Ng, K. P. Loh, L. Q. Li, P. Ho, P. Bai and J. H. K. Yip, *Acs Nano*, 2009, **3**, 2103.

144. R. Lakshmanan, N. C. Shivaprakash and S. S. Nair, *J. Lumin.*, 2015, **168**, 145.

145. R. Indumathy, M. Kanthimathi, T. Weyhermuller and B. U. Nair, *Polyhedron*, 2008, **27**, 3443.

146. B. Maity, S. Gadadhar, T. K. Goswami, A. A. Karande and A. R. Chakravarty, *Dalton Trans.*, 2011, **40**, 11904.

147. P. Sinha, N. Kumari, K. Singh and L. Mishra, *Inorganica Chim. Acta*, 2015, **432**, 71.

148. V. Camara, N. Barquero, D. Bautista, J. Gil-Rubio and J. Vicente, *Inorg. Chem.*, 2015, **54**, 6147.

149. K. Takada, R. Sakamoto, S. T. Yi, S. Katagiri, T. Kambe and H. Nishihara, *J. Am. Chem. Soc.*, 2015, **137**, 4681.

150. E. C. Constable, C. E. Housecroft, M. Neuburger, S. Schaffner and L. J. Scherer, *Dalton Trans.*, 2004, **0**, 2635.

151. M. A. Halcrow, *Crystals*, 2016, **6**, 58.

152. A. Jouaiti, V. Jullien, M. W. Hosseini, J. M. Planeix and A. De Cian, *ChemComm*, 2001, **0**, 1114.

153. A. Galet, A. B. Gaspar, M. C. Munoz and J. A. Real, *Inorg. Chem.*, 2006, **45**, 4413.

154. X. P. Zhou, W. X. Ni, S. Z. Zhan, J. Ni, D. Li and Y. G. Yin, *Inorg. Chem.*, 2007, **46**, 2345.

155. J. Sanning, P. R. Ewen, L. Stegemann, J. Schmidt, C. G. Daniliuc, T. Koch, N. L. Doltsinis, D. Wegner and C. A. Strassert, *Angew. Chem. Int. Ed.*, 2015, **54**, 786.

156. S. S. Batsanov, *Inorg. Mater.*, 2001, **37**, 871.

157. J. McMurtrie and I. Dance, *CrystEngComm*, 2005, **7**, 216.

158. H. D. B. Jenkins and K. P. Thakur, *J. Chem. Educ.*, 1979, **56**, 576.

159. F. Habib, O. R. Luca, V. Vieru, M. Shiddiq, I. Korobkov, S. I. Gorelsky, M. K. Takase, L. F. Chibotaru, S. Hill, R. H. Crabtree and M. Murugesu, *Angew. Chem. Int. Ed*, 2013, **52**, 11290.

160. J. J. Schneider, R. Goddard and C. Kruger, *Z. Naturforsch. B Chem. Sci.*, 1995, **50**, 448.

161. K. B. Wiberg and T. P. Lewis, *J. Am. Chem. Soc.*, 1970, **92**, 7154.

162. C. Dares, T. Manivannan, P. G. Potvin and A. B. P. Lever, *Inorganica Chim. Acta*, 2011, **374**, 606.

163. M. G. B. Drew, M. R. S. Foreman, A. Geist, M. J. Hudson, F. Marken, V. Norman and M. Weigl, *Polyhedron*, 2006, **25**, 888.

164. C. S. Campos-Fernandez, B. W. Smucker, R. Clerac and K. R. Dunbar, *Isr. J. Chem.*, 2001, **41**, 207.

165. P. Gutlich, A. B. Gaspar and Y. Garcia, *Beilstein J. Org. Chem.*, 2013, **9**, 342.

166. M. A. Halcrow, *Chem. Soc. Rev.*, 2013, **42**, 1784.

167. J. Kusz, R. Bronisz, M. Zubko and G. Bednarek, *Chem. Eur. J.*, 2011, **17**, 6807.

168. L. Wiehl, G. Kiel, C. P. Kohler, H. Spiering and P. Gutlich, *Inorg. Chem.*, 1986, **25**, 1565.

169. H. Koppen, E. W. Muller, C. P. Kohler, H. Spiering, E. Meissner and P. Gutlich, *Chem. Phys. Lett.*, 1982, **91**, 348.

170. N. F. Chilton, R. P. Anderson, L. D. Turner, A. Soncini and K. S. Murray, *J. Comput. Chem.*, 2013, **34**, 1164.

171. F. Habib, I. Korobkov and M. Murugesu, *Dalton Trans.*, 2015, **44**, 6368.

172. F. Habib, C. Cook, I. Korobkov and M. Murugesu, *Inorganica Chim. Acta*, 2012, **380**, 378.

173. S. Gomez-Coca, E. Cremades, N. Aliaga-Alcalde and E. Ruiz, *J. Am. Chem. Soc.*, 2013, **135**, 7010-7018.

174. R. Herchel, Z. Dvorak, Z. Travnicek, M. Mikuriya, F. R. Louka, F. A. Mautner and S. S. Massoud, *Inorganica Chim. Acta*, 2016, **451**, 102.

175. T. F. Liu, D. Fu, S. Gao, Y. Z. Zhang, H. L. Sun, G. Su and Y. J. Liu, *J. Am. Chem. Soc.*, 2003, **125**, 13976.

176. J. Vallejo, I. Castro, R. Ruiz-Garcia, J. Cano, M. Julve, F. Lloret, G. De Munno, W. Wernsdorfer and E. Pardo, *J. Am. Chem. Soc.*, 2012, **134**, 15704.

177. R. Herchel, L. Vahovska, I. Potocnak and Z. Travnicek, *Inorg. Chem.*, 2014, **53**, 5896.

178. I. Nazarenko, F. Pop, Q. C. Sun, A. Hauser, F. Lloret, M. Julve, A. El-Ghayoury and N. Avarvari, *Dalton Trans.*, 2015, **44**, 8855.

179. I. R. Evans, J. A. K. Howard, L. E. M. Howard, J. S. O. Evans, Z. K. Jacimovic, V. S. Jevtovic and V. M. Leovac, *Inorganica Chim. Acta*, 2004, **357**, 4528.

180. M. T. Lemaire, T. M. Barclay, L. K. Thompson and R. G. Hicks, *Inorganica Chim. Acta*, 2006, **359**, 2616.

181. C. X. Shao, W. H. Sun, Y. Chen, R. J. Wang and C. J. Xi, *Inorg. Chem. Comm.*, 2002, **5**, 667.

182. K. Matsubara, T. Sueyasu, M. Esaki, A. Kumamoto, S. Nagao, H. Yamamoto, Y. Koga, S. Kawata and T. Matsumoto, *Eur. J. Inorg. Chem.*, 2012, **2012**, 3079.

183. D. M. Jenkins, A. J. Di Bilio, M. J. Allen, T. A. Betley and J. C. Peters, *J. Am. Chem. Soc.*, 2002, **124**, 15336.

184. U. Chakraborty, M. Modl, B. Muhldorf, M. Bodensteiner, S. Demeshko, N. J. C. van Velzen, M. Scheer, S. Harder and R. Wolf, *Inorg. Chem.*, 2016, **55**, 3065.

185. Y. I. Cho, M. L. Ward and M. J. Rose, *Dalton Trans.*, 2016, **45**, 13466.

186. D. L. Reger, A. E. Pascui, M. D. Smith, J. Jezierska and A. Ozarowski, *Inorg. Chem.*, 2012, **51**, 11820.

187. J. A. Barnes, W. E. Hatfield and D. J. Hodgson, *J. Chem. Soc. D*, 1970, **0**, 1593.

188. J. A. Barnes, W. E. Hatfield and D. J. Hodgson, *Inorg. Chem.*, 1972, **11**, 144.

189. D. Y. Jeter, D. J. Hodgson and W. E. Hatfield, *Inorg. Chem.*, 1972, **11**, 185.

190. P. Singh, W. E. Hatfield, D. J. Hodgson and D. Y. Jeter, *Inorg. Chem.*, 1972, **11**, 1657.

191. D. Y. Jeter, D. L. Lewis, D. J. Hodgson, W. E. Hatfield and J. C. Hempel, *Inorg. Chem.*, 1972, **11**, 1958.

192. D. L. Lewis, D. J. Hodgson and W. E. Hatfield, *Inorg. Chem.*, 1972, **11**, 2216.